Université de Toulouse

THÈSE

En vue de l'obtention du

DOCTORAT DE L'UNIVERSITÉ DE TOULOUSE

Délivré par *l'Université Toulouse III – Paul Sabatier*
Discipline ou spécialité: *Physique de la matière*

Présentée et soutenue par Llinersy Uranga-Piña
Le 9 juillet 2012

Titre: *Ultrafast geometrical rearrangement of solid neon upon photoexcitation of a* **NO** *impurity: A quantum dynamics study*

JURY

M.	Christoph Meier	LCAR, Toulouse	Directeur de thèse
M.	Jesús Rubayo-Soneira	InSTEC, L'Havane	Co-Directeur de thèse
M.	Ramón Hernández-Lamoneda	UNAM, Mexico D.F.	Rapporteur
M.	Maurice Monnerville	PhLAM, Villeneuve d'Ascq	Rapporteur
M^{me}	Nadine Halberstadt	LCAR, Toulouse	Examinatrice
M.	Rabdel Ruiz-Salvador	IMRE, L'Havane	Examinateur
M.	Osvaldo de Melo-Pereira	UH, L'Havane	Examinateur
M.	Carlos Cruz-Inclán	CEADEN, L'Havane	Examinateur

École doctorale: *Sciences de la matière*
Unité de recherche: *Laboratoire Collisions Agrégats Réactivité*
Directeur de thèse: Christoph Meier

ULTRAFAST GEOMETRICAL REARRANGEMENT OF SOLID NEON UPON PHOTOEXCITATION OF A NO IMPURITY: A QUANTUM DYNAMICS STUDY

submitted to the

UNIVERSITÉ PAUL SABATIER

and the

UNIVERSIDAD DE LA HABANA

for the degree of Doctor of Philosophy

Author:

Llinersy Uranga Piña

Advisors:

Prof. Christoph Meier

Prof. Jesús Rubayo Soneira

Havana

2012

Abstract

This thesis reports on results of quantum molecular dynamics simulations of photo-induced structural dynamics in nitric oxide (NO) doped solid neon (Ne). The local perturbation, caused by the optical excitation of the dopant molecule, propagates radially from the NO to the lattice atoms, in a shock-wave-like fashion. The ultrafast relaxation dynamics is studied using a purely quantum mechanical approach, based on a multidimensional shell model, with the shell radii being the dynamical variables. As a consequence of the weak anisotropy of the NO-Ne interaction, the model accounts for the main dynamical features of the rare gas solid while it implies a significant dimensionality reduction with respect to the real condensed phase system. The numerical propagation of the multidimensional wave packet allows the analysis of both the static deformation of the solid due to the impurity and the dynamical response after femtosecond excitation. The photo-induced dynamics of solvent atoms around the impurity centre is found to be a complex collective process, which involves many degrees of freedom. The proposed theoretical methodology allows to consider realistic time-dependent femtosecond pulses and the effect of the pulse duration on the geometrical rearrangement dynamics is clearly shown. The time-resolved absorption spectra were simulated, using the pulse parameters of previous pump-probe spectroscopic experiments, carried out with with femtosecond time-resolution. The computed transient signals qualitatively reproduce the experimental results, thereby enabling a clear analysis of the ultrafast mechanism of the energy transfer into the solid. The influence of explicitly including dynamical correlations in the theoretical treatment of the relaxation dynamics, within the Multi-Configurational Time-Dependent Hartree (MCTDH) scheme, was addressed. This aspect is found to be important only for certain degrees of freedom. The consideration of multi-configurational wave functions does not appreciably modify the values of observables such as the average shell radii, with respect to those obtained employing the time-dependent Hartree ansatz. However, the inclusion of correlations reduces the degree of structuring of the calculated pump-probe signals and improve the agreement with experimental results.

Contents

Résumé de la thèse

La compréhension des propriétés structurelles et dynamiques des systèmes à nombreux degrés de liberté est l'un des objectifs principaux de la physique de la matière condensée. En particulier, le progrès des techniques expérimentales de spectroscopie femtoseconde (spectroscopie laser ultrarapide ou technique de pompe / sonde) a donné lieu à un grand nombre de résultats expérimentaux et théoriques qui ont permis d'améliorer la compréhension des processus dynamiques de systèmes moléculaires en temps réel. La spectroscopie pompe / sonde est basée sur l'utilisation d'une première impulsion laser qui déclenche un réarrangement géométrique du système moléculaire, tandis que la deuxième impulsion, retardée dans le temps par rapport à la première, est utilisée pour détecter les mouvements des noyaux atomiques à l'échelle de temps de la femtoseconde. Cette technique est un outil puissant qui permet d'étudier les mécanismes de redistribution de l'énergie au niveau microscopique, dans de nombreux phénomènes en physique, chimie ou biologie (par exemple, l'isomérisation de la protéine rhodopsine qui constitue un processus primaire pour la vision) .

En phase condensée, les mesures spectroscopiques à l'échelle de la femtoseconde renseignent sur la réponse dynamique ultrarapide des espèces moléculaires localisées dans le voisinage d'un centre photoactif, tandis que le caractère macroscopique du milieu (solide, liquide, une protéine, etc.) passe au second plan. Par exemple, si on considère qu'une fonction biologique est, conformément au paradigme classique,

une séquence d'évènements caractérisés par des changements structuraux, les études expérimentales et théoriques de l'évolution temporelle de ces transformations sont primordiales pour la compréhension des mécanismes atomistiques de l'activité biologique. Les techniques pompe / sonde sont particulièrement bien adaptées pour étudier les états électroniques excités en phase condensée, associés aux propriétés optiques et électroniques de ces systèmes. Elles offrent la possibilité d'obtenir de l'information spectroscopique sur le centre optiquement actif (par exemple, une impureté dans un solide) et son milieu environnant, à partir de la comparaison entre les résultats des mesures spectroscopiques de la molécule dans les phases condensées et gazeuses. Grâce aux faibles interactions entre la molécule et son environnement, les matrices de gaz rares ou d'hydrogène moléculaire sont spécialement adaptées pour les études de spectroscopie moléculaire. Elles ont de nombreux avantages pour la caractérisation des processus dynamiques à l'échelle de la femtoseconde: elles constituent un milieu non polaire, chimiquement inert et leurs propriétés élastiques et thermodynamiques sont bien caractérisés. De plus, elles sont faciles à obtenir par déposition directe du gaz sur un substrat froid sous vide. Il est important de remarquer que les températures très basses de ces échantillons réduisent considérablement le nombre d'états accessibles aux molécules hôtes, ce qui est très favorable du point de vue de la modélisation théorique. Au niveau microscopique, l'excitation électronique de l'impureté par la première impulsion (la pompe) crée une redistribution de la densité électronique de la molécule, suivie par la réorganisation structurelle du milieu environnant. Ce principe est présent dans toute réaction chimique en phase condensée. Dans ce contexte, l'excitation conduit à une modification significative de la densité de charge de l'impureté et de son interaction avec le milieu environnant.

Dans ce contexte, la réorganisation géométrique de la matrice, après l'absorption d'un photon par le centre optiquement actif, a suscité un grand nombre d'études,

tout théoriques qu'expérimentales [1–12], en particulier sur les dihalogènes (Cl_2, Br_2, I_2, F_2 et ClF) dans une matrice d'argon [1, 2, 13]. Dans ces systèmes, beaucoup de phénomènes intéressants, ont pu être élucidés, comme par exemple le mouvement cohérent des atomes de gaz rares qui entourent l'impureté, ou le déphasage des vibrations et de l'inversion ultrarapide du spin de la molécule [14]. D'autres études résolues en temps ont été réalisées avec la molcule de NO en matrices de gaz rares [3–5] ou d'hydrogène. Pour les atomes de gaz rares légers, comme le Ne, ou pour des matrices d'hydrogène moléculaire, la réponse dynamique montre des effets quantiques plus prononcés. La figure 1 montre un schéma du solide avec l'impureté au centre et les paquets d'onde nucléaires associés à l'impureté et à chacun des atomes du solide:

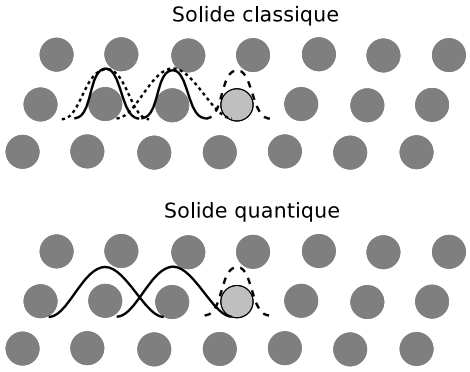

Figure 1: Schéma de solides classiques et quantiques. Cercles gris obscurs : les atomes du solide. Cercles gris clairs : l'impureté. Lignes continues : les fonctions d'onde nucléaires stationnaires de chaque atome du solide. Lignes discontinues : la fonction d'onde nucléaire de l'impureté. Lignes pointillées : les fonctions d'onde nucléaires au bout d'un temps t après l'excitation de l'impureté. Le solide est considéré classique si les fonctions d'onde stationnaires de chaque constituant ne se recouvrent pas, et quantique si elles se recouvrent. Dans un solide dont les propriétés d'équilibre peuvent être décrites classiquement, des effets quantiques prononcés peuvent toutefois être présents si, comme conséquence de la dynamique déclenchée par l'excitation locale, les fonctions d'onde dépendantes du temps se recouvrent au cours du temps.

Le système se comportera classiquement si les paquets d'ondes des constituants ne se recouvrent pas. Dans le cas contraire, des effets quantiques se manifesteront. Ce recouvrement peut être toujours présent, ou bien l'excitation locale de l'impureté

peut induire un élargissement des paquets d'ondes nucléaires des atomes environnants dans le temps et mener ainsi à un recouvrement dynamique.

Les études dans le domaine temporel dans des systèmes quantiques comportant beaucoup de degrés de liberté représentent un défi considérable du point de vue théorique. Parmi ces travaux, on peut citer des études sur la relaxation structurale dans les solides des gaz rares et d'hydrogène moléculaire [3, 15]. Ces travaux ont été complétés par des études expérimentales et par des simulations avec des méthodes de dynamique moléculaire classique (DMC).

A cause de l'amplitude significative des mouvements de point zéro, le solide de *Ne* constitue un système modèle pour l'étude de l'influence des effets quantiques sur les mécanismes fondamentaux de restructuration géométrique et sur la dissipation d'énergie associée à ce processus.

Dans le travail de thèse présenté, nous étudions la restructuration d'une matrice cryogénique de *Ne* provoquée par l'excitation électronique d'une impureté (molécule de *NO*). Par une méthode purement quantique, ce processus est analysé en détail et des spectres pompe-sonde sont simulés, pour pouvoir les comparer directement avec des résultats expérimentaux [3].

L'impureté sélectionnée possède trois propriétés fondamentales:

1. la molécule *NO* remplace un *Ne* du solide, donc elle n'affecte pas de manière importante les propriétés structurales du solide dans son état fondamental;

2. elle interagit fortement avec son environnement quand elle est photoexcitée vers son premier état de Rydberg. Dans cet état, le nuage électronique de *NO* et les orbitales de couche fermée de ses plus proches voisins se recouvrent spatialement dans le cristal, ce qui mène à un déplacement radial très prononcé de ces atomes;

3. ce mouvement est expérimentalement accessible par spectroscopie d'absorption dynamique à partir de l'état excité, ce qui nous permet de comparer directement les modélisations presentées ici avec des données experimentales.

Du point de vue théorique, comme l'excitation initiale et la détection impliquent des processus moléculaires collectifs, les modélisations théoriques de ces phénomènes sont fondamentales pour l'interprétation des résultats expérimentaux. Alors que pour les systèmes atomiques ou moléculaires simples le traitement théorique peut offrir des résultats très précis, dans les cas dans lesquels un grand nombre d'atomes sont impliqués, la modélisation théorique de la dynamique quantique loin de l'équilibre et l'interprétation des signaux expérimentaux constituent un défi considérable. Dans le contexte de la spectroscopie de pompe / sonde, la complexité vient non seulement du grand nombre de degrés de liberté impliqués, mais aussi de la variété des interactions intermoléculaires mises en jeu et de l'interaction du système avec des champs externes.

Dans ces dernières années, les techniques basées sur les intégrales de chemin de la mécanique quantique et les méthodes de résolution de l'équation de Schrödinger dépendante du temps pour des systèmes à haute dimensionnalité, comme la méthode de Hartree Multiconfigurationnel Dépendant du Temps (MCTDH, d'après ses initiales en anglais) [16,17], ont permis des avancements significatifs. La limitation fondamentale de ces méthodes est la croissance rapide de son coût de calcul avec l'augmentation du nombre de degrés de liberté. En particulier, avec les ressources informatiques actuelles, la description quantique de la dynamique de milliers d'atomes est encore hors de portée. C'est pourquoi, malgré le progrès des méthodes quantiques, les simulations par dynamique moléculaire classique constituent encore un outil très utilisé pour les études de processus dynamiques en phase condensée [1,4,6,7]. Conformément aux lois de la mécanique classique, la modification de l'état dynamique du système est locale dans les variables de l'espace de phases. Cette caractéristique implique un

avantage considérable en ce qui concerne les capacités d'allocation de mémoire et de temps de calcul requis pour intégrer numériquement les équations du mouvement, par rapport à la solution du problème quantique correspondant. Cependant, le comportement de systèmes macroscopiques où les effets quantiques sont présents ne peut pas être décrit correctement par un traitement purement classique [15].

La présente thèse est consacrée à l'étude des propriétés structurales et à la réorganisation géométrique du solide de *Ne*, comme conséquence de la photoexcitation électronique d'une impureté de *NO*. Pour pouvoir réaliser un traitement purement quantique d'un système avec autant de degrés de liberté, un modèle de dimensionnalité réduite s'impose. Grâce à la faible anisotropie de l'interaction *NO-Ne* dans l'état excité [18], le mouvement principal des atomes de *Ne* autour du *NO* est essentiellement une expansion radiale, qui a été appelée "formation d'une bulle électronique" [5, 11]. Basés sur cette propriété, nous avons construit un modèle de couches multidimensionnel, où les rayons des couches constituent les variables dynamiques. De cette façon il est possible de réaliser le traitement quantique explicite de la dynamique de beaucoup de particules, et d'examiner les propriétés statiques et dynamiques de ce système.

Les contributions principales de cette thèse sont les suivantes:

1. Le développement d'une méthodologie pour la simulation numérique des propriétés d'équilibre et des processus dynamiques dans des systèmes quantiques en phase condensée. Jusqu'à présent, l'étude quantitative de phénomènes dépendants du temps dans ce type de systèmes était limitée à des extensions semiclassiques de simulations classiques. Ces dernières ne peuvent pas toujours reproduire le comportement de systèmes avec des effets quantiques prononcés.

2. L'identification des mécanismes primaires et secondaires de redistribution vers les degrés de liberté de la matrice de néon de l'énergie déposée par le laser

pendant l'excitation électronique d'une molécule de NO,

3. L'évaluation des effets de durée finie et de forme de l'impulsion laser sur la dynamique de matrices de Ne dopées avec NO, ainsi que des effets d'interférence du paquet d'ondes vibrationnel formé à partir de l'excitation de la molécule. Ces phénomènes ne peuvent pas être décrits avec des simulations classiques.

4. L'évaluation de l'importance des corrélations dynamiques et de leur influence sur l'évolution temporelle du paquet d'ondes multidimensionnel qui décrit le solide de Ne.

De façon complémentaire aux travaux présentés ici, d'autres approches ont été proposées, avec l'objectif d'incorporer les effets de la délocalisation quantique des particules dans les simulations classiques. Par exemple, dans l'approche proposé par Bergsma, l'effet de l'énergie de point zéro des atomes du solide est incorporé au moyen d'une température effective, dérivée de l'approximation harmonique des oscillations du réseau [19, 20]. D'autres travaux proposent de considérer des paquets d'onde Gaussiens au lieu de particules ponctuelles [21]. Avec la restriction de largeurs fixes, cette approche est formellement équivalente à l'emploi de potentiels effectifs dans les simulations classiques, obtenus à partir de la convolution du potentiel d'interaction entre les particules avec la fonction Gaussienne. Ces deux méthodes, l'introduction d'une température ou les potentiels effectifs, sont approximatives par nature et ne peuvent pas tenir compte des effets de délocalisation prononcé et des effets de corrélation quantiques. Les techniques de simulation basées sur le formalisme d'intégrales de chemin sont, d'autre part, limitées au calcul de propriétés d'équilibre. Une autre limitation importante des méthodes semiclassiques est que le process d'excitation doit être consideré comme instantané, ce qui n'est pas toujours le cas dans des expériences réalistes.

Dans ce contexte scientifique, la **question principale** est:

Quelle est l'influence du caractère quantique du solide de néon et de la durée finie de l'impulsion laser sur la réponse dynamique de la matrice après photoexcitation de la molécule de NO ?

L'hypothèse fondamentale de ce travail est que l'inclusion des effets quantiques, par la solution numérique de l'équation de Schrödinger multidimensionnelle dépendante du temps, donne une description fiable de la dynamique de relaxation géométrique des matrices de néon dopées avec NO, et permet de reproduire théoriquement les spectres dynamiques d'absorption mesurés expérimentalement.

L'objectif général de la thèse présentée est l'étude de l'influence des effets de délocalisation et de corrélation quantiques entre les différents degrés de liberté, et de la forme explicite de l'impulsion laser sur la réponse dynamique de la matrice.

Les objectifs spécifiques de la thèse sont :

1. Etudier les caractéristiques du mouvement des atomes de Ne qui déterminent les modifications structurales principales induites par la transition électronique de l'impureté, et les mécanismes de redistribution de l'énergie déposée par le laser d'excitation.

2. Evaluer l'influence de la forme de l'impulsion excitatrice sur l'évolution temporelle du paquet d'ondes vibrationnel.

3. Modéliser les spectres d'absorption dynamiques et les comparer avec les données expérimentales, et étudier l'influence des paramètres des impulsions

4. Etudier l'effet des corrélations dynamiques entre différents degrés de liberté sur les observables calculées.

La thèse comporte sept chapitres : *Introduction*, *Caractéristiques du solide de Néon*, *La molécule de* NO, *Expériences de pompe / sonde et dynamique de relaxation du solide de* Ne *dopé avec une impureté de* NO, *Méthodologie*, *Résultats et Discussion*, *Conclusions et Recommandations*, avec les contenus suivants:

Dans le **Chapitre 1**, *Introduction*, sont décrits la motivation de ce travail et les objectifs principaux.

Le **Chapitre 2**, *Caractéristiques du solide du Néon*, est dédié à l'introduction des caractéristiques générales du solide de *Ne*, ainsi que ses propriétés physiques et structurelles, et les particularités de sa spectroscopie électronique.

Dans le **Chapitre 3**, *La molécule de* NO, certaines des propriétés de la molécule de *NO* dans les phases gazeuse et condensée en matrice de *Ne* sont présentées; principalement les propriétés qui déterminent la réponse dynamique de la matrice après la photoexcitation de *NO*.

Dans le **Chapitre 4**, *Expériences de pompe / sonde et dynamique de relaxation du solide de* Ne *dopé avec une impureté de* NO, nous décrivons sommairement les expériences de spectroscopie pompe / sonde dans le domaine temporel du système *NO* en matrice de *Ne*, et ses caractéristiques principales, comme la mesure de l'évolution temporelle de l'expansion de la cavité.

Dans le **Chapitre 5**, *Méthodologie*, le modèle de couches developpé est présenté avec la construction de la surface de potentiel correspondante. En plus, la méthode MCTDH utilisée dans la résolution numérique de l'équation de Schrödinger dépendant est detaillée.

Dans le **Chapitre 6**, *Résultats et discussion*, sont discutés et analysés en détail les résultats obtenus pour les propriétés stationnaires, comme par exemple les déformations statiques dues à la présence de l'impureté et les spectres d'absorption et d'émission résolus en energie. Ensuite, les propriétés dynamiques, comme la densité réduite le

long de chaque degré de liberté, les mécanismes principaux de dissipation de l'énergie dans le solide et les spectres d'absorption dynamique sont presentés. En particulier, les effets des impulsions de durée finie et des corrélations quantiques sur toutes ces observables forment un point central de ce chapitre.

Le **Chapitre 7**, *Conclusions et recommandations*, contient les conclusions principales de ce travail. La thèse termine avec une analyse des perspectives immédiates de ce travail, spécialement consacrée à la possibilité d'étendre l'étude à d'autres solides quantiques, comme par exemple le $p - H_2$.

Conclusions

En utilisant un modèle radial de couches, nous avons pu modéliser la réponse géométrique d'une matrice de *Ne* dopée avec une molécule de *NO*, après la photoexcitation de l'impureté, par deux méthodes purements quantiques. L'un est basée sur l'approche de Hartree dépendante du temps et l'autre est la méthode de Hartree multi-configurationnel dépendant du temps. Il s'agit d'une étude basée sur la solution directe de l'équation de Schrödinger multidimensionnelle pour un système avec 80 degrés de liberté, correspondant à 4192 atomes restreints à bouger le long de la direction radiale, en conservant une description réaliste des interactions intermoléculaires. Les conclusions principales de cette étude sont les suivantes :

1. La restructuration de la matrice est un phénomène multidimensionnel, caractérisé par l'expansion initiale de la première couche de voisins de l'impureté (appelé "bulle électronique") et par une corrélation significative entre les différents degrés de liberté du solide. Par conséquent, les modifications dans la configuration du système ne dépendent pas d'une manière monotone du rayon des couches, mais montrent clairement une déformation le long des axes préférentiels, (l'axe 110), définis par l'impureté centrale et les atomes de la première couche

de voisins. L'estimation de la vitesse de propagation de la perturbation indique qu'elle possède les caractéristiques d'une onde de choc.

2. Deux mécanismes principaux de dissipation de l'énergie peuvent être distingués: les collisions directes entre les atomes des couches qui forment l'axe cristallographique principal, et les collisions latérales de ces atomes avec ceux qui sont placés en dehors de l'axe (110). Ces dernières forment un "bain" vers lequel l'énergie, se propageant long de l'axe principal, est dissipée. Il est important de souligner que ce bain n'est pas formé par des atomes lointains, mais par les atomes qui se trouvent placés dans des positions défavorables par rapport à l'impureté. Nous avons trouvé que 0.55 eV sont déposés dans le bain par le mécanisme de dissipation mentionné ci-dessus, en parfait accord avec la valeur expérimentale [3].

3. La forme de l'impulsion excitatrice a une influence significative sur l'évolution temporelle du paquet d'ondes formé pendant l'excitation. En utilisant les paramètres de l'expérience [3–5, 15], nous avons trouvé que la durée finie de l'impulsion (280 fs) provoque des effets d'interférences quantiques de la fonction d'onde décrivant la dynamique de la première couche. Ceci est dû au fait que le temps d'expansion de la première couche est du même ordre de grandeur que la durée de l'impulsion.

4. Les spectres pompe / sonde modélisés par l'approche de Hartree dépendante du temps reproduisent qualitativement les résultats expérimentaux, en montrant clairement la formation ultrarapide de la bulle après la photoexcitation, sa contraction après environ 1 ps, et la dynamique de relaxation postérieure, due au couplage avec d'autres degrés de liberté. Cependant, la contraction de la bulle n'est pas un recul simple de la première couche, mais une réponse collective de

la matrice qui implique un grand nombre d'atomes environnants.

5. L'influence des corrélations dynamiques sur la relaxation du système a été élucidée par comparaison des résultats de la propagation numérique du paquet d'ondes multiconfigurationnel avec ceux obtenus par l'approche de Hartree. Qualitativement, l'approche de champ moyen (Hartree) donne une description correcte de la majorité des observables pendant l'évolution dynamique du système. Le transfert d'énergie dans le solide, ainsi que les déplacements des atomes voisins, sont convenablement décrits dans l'approche Hartree dependante du temps. Cependant, des structures plus détaillées de la forme de la distribution des particules dans l'espace de configurations, comme par exemple les fonctions de distribution radiale, montrent clairement les influences des corrélations quantiques. En particulier, le degré decohérence vibrationnelle du paquet d'ondes multiconfigurationnel est beaucoup plus petit que dans le cas de la méthode de TDH. L'approche de champ moyen conduit à des mouvements oscillatoires prononcés de la largeur de la densité radiale, qui sont pratiquement absents dans les résultats obtenus par la fonction d'onde corrélée. Cette caractéristique du mouvement est aussi visible dans certaines quantités directement mesurables, comme les signaux pompe / sonde. En général, l'inclusion des corrélations dans le traitement théorique conduit à un lissage des spectres, avec des profils moins structurés. En résumant, on peut conclure que les corrélations dynamiques diminuent significativement la cohérence vibrationnelle qui apparaît dans les résultats obtenus par la méthode Hartree dependante du temps.

Perspectives futures

En ce qui concerne l'extension de la méthodologie developpée, plusieurs directions

pour des travaux futurs peuvent être considérées:

1. *L'inclusion de l'anisotropie du potentiel impureté - gaz rare.* La densité électronique qui détermine les interactions $NO(X,\ A)$-Ne est légèrement anisotrope. L'effet de cet anisotropie [18,22] dans notre système pourrait être évalué en divisant les couches les plus affectées et en traitant chacun de ces sous-groupes de manière indépendante dans la dynamique. Cette approche permettrait d'étendre ce modèle au-delà de l'approche purement radiale, bien que sa possibilité d'application, en particulier la quantité de subdivisions qu'il est possible d'introduire, sera limitée par l'augmentation du nombre de degrés de liberté .

2. *L'emploi de méthodes approximatives alternatives.* Dans certains cas, il peut être convenable de recourir à des traitements approximatifs [23, 24], comme la méthode de la Dynamique Moyennée de Point Zéro (ZPAD, par ses initiales en anglais) [25]. Malgré son caractère approximatif, cette méthode pourrait être utilisée pour simuler la quantité d'atomes impliqués dans ce processus. Des travaux dans cette direction sont actuellement en cours.

D'autre part, le modèle radial développé dans cette thèse peut être appliqué directement à l'étude d'autres solides avec un comportement quantique prononcé, comme les matrices de para-hydrogène, dont la relaxation structurale photoinduite a été l'objet d'études expérimentales et théoriques [3–5, 15].

Sur la base des résultats obtenus dans ce travail de thèse, la méthode de Hartree dependante du temps peut devenir la méthode la plus prometteuse, car pour un effort numérique important, mais faisable, elle peut fournir des résultats qualitativement corrects. La modélisation de la dynamique en temps réel des solides à fort caractère quantique, comme le $p - H_2$, pourrait ainsi devenir réalité dans un futur proche.

Chapter 1

Introduction

Understanding the structural and dynamical properties of many-body systems is one of the primary goals of condensed matter physics. Especially, the progress of the experimental techniques known as femtosecond spectroscopy (also named as ultrafast laser or pump-probe spectroscopy) has stimulated, during the last decades, a large number of experimental and theoretical investigations devoted to gain a deeper insight in fundamental dynamical processes in molecular systems. In pump-probe setups, a first laser pulse triggers the dynamical rearrangement of the system, whereas a second, time-delayed pulse is used to monitor the motion of atomic nuclei in the femtosecond time scale [26]. This technique constitutes a powerful tool to investigate, at a microscopic level, the mechanisms of energy redistribution in molecular media, relevant for many phenomena in physics, chemistry and biology (for example, the isomerization of the protein rhodopsin as the primary step of visual image detection by fotoreceptor cells in the retina [27]). These studies provide a different perspective, from which the traditional frontiers among these fields become diffuse. In condensed phase, femtosecond measurements are sensitive to the ultrafast dynamical response of the molecular species localized around a center selectively activated by a light pulse,

while the macroscopic character of the medium (solid, liquid, protein, etc.) recedes in the background. For example, if a biological function is regarded, according to the classical paradigm, as a sequence of events characterized by structural changes, hence the experimental and theoretical studies which address the time evolution of such transformations constitute privileged approaches to comprehend the basic mechanisms of biological activity [26, 28].

Pump-probe techniques are especially valuable for the investigation of excited electronic states in condensed phase, associated to the optical and electronic properties of such systems [29–31]. In the case of an impurity embedded in a solid, this tool offers the opportunity to get spectroscopic information from both the chromophore and the surrounding medium, via the comparison between the spectroscopic measurements in gas and condensed phases. Due to the weak interaction with guest molecules and to the transparency of the solid within the ultraviolet spectral range, rare gas matrices are especially amenable for molecular spectroscopy studies [32–38]. Furthermore, rare gas solids present several advantages for the characterization of dynamical processes since the provide a non-polar environment, chemically inert, with well-defined physical properties. In fact, rare gas and para-hydrogen crystals are structurally stable matrices, with well-known elastic and thermodynamic properties. [39–42]. Additionally, they can be obtained, in a high vacuum environment, via direct deposition of the corresponding gas on a cold substrate. It is worth to notice that the cryogenic conditions under which these samples are kept, minimize the density of states accessible to guest molecules, thereby reducing the complexity of the system under study, especially from the theoretical point of view.

In particular, configurational rearrangements of the matrix, upon photon absorption by the chromophore, have been intensively studied. The interest on this process has been stimulated by its ubiquity and its inherent complexity, since it involve the

many-body response of the medium to the photo-excitation. At a microscopic level, the electronic excitation of the impurity by an electromagnetic pulse, cause a redistribution of the electron density of the molecule. The latter is followed by the structural reorganization of the surrounding medium. This basic mechanism is expected to be present in any chemical reaction in the condensed phase. Photo-excitation of Rydberg states and photo-ionization are especially interesting, since in those processes an electron is promoted to an electronic state characterized by a main quantum number which is different from that of the initial state. In this way, the electronic transition leads to a marked modification of the charge density of the impurity and of its interaction with the medium in which is embedded.

Doped rare gas solids and clusters has been widely used as model systems to study photo-induced geometrical rearrangements in many-body systems [1–15,23,37,43–59]. Specifically, dihalogens (Cl_2, Br_2, I_2, F_2 y ClF) in solid argon has been extensively studied, from both theoretical and experimental points of view [1, 2, 13, 14, 37, 44–46]. The time-domain studies carried out on such systems have revealed many interesting phenomena such as the coherent motion, upon photo-excitation, of the rare gas atoms around the impurity [34,45,48–50], the dephasing of molecule vibrations [47,48], or the ultrafast spin-flip [14, 44, 51]. Additionally, several pump-probe experiments on NO doped rare gas [3–5,53–55] and para-hydrogen [5,6,56–59] solids have been carried out, stimulated by the spectroscopic properties of the first Rydberg state of the impurity (similar to those of the $n = 1$ exciton in pure rare gas solids). The majority of these studies were performed in argon matrices. However, when moving to solids formed by lighter rare gas atoms (Ne) or even to molecular hydrogen (para-H_2), the induced dynamics is expected to exhibit more pronounced quantum effects.

As a consequence of both the significant amplitude of the zero-point motions and the low-temperature regime, solid Ne constitutes a model system to investigate the

influence of quantum effects on the fundamental mechanisms of large-scale configurational rearrangements and on the energy dissipation associated to this restructuring. In our study, we investigate the structural reorganization upon electronic excitation of a impurity, the nitric oxide molecule (NO), and we compare the results of our quantum simulations with those of pump-probe experiments carried out in this system. The impurity chosen as molecular probe exhibits three important properties [3]:

1. the molecule occupies a substitutional site in the solid Ne, so, when the impurity is in its ground electronic state, its presence does not appreciably affect the equilibrium properties of the solid;

2. it interacts strongly with the surrounding crystal after being photo-excited: in its first Rydberg state, A, the electron density of the molecule partially overlaps with the closed shell orbitals of its nearest neighbours in the solid, triggering a pronounced radial displacement of these atoms;

3. it provides an experimental observable which is very sensitive to the configuration of the local environment, that is, the medium response is directly observed, instead of being indirectly inferred from some intramolecular properties. The fluorescence of the A state allows to perform direct, background free, measurements of the intensity of the interaction between the impurity and the surrounding medium.

From the theoretical point of view, since both the initial excitation as well as the detection involve collective molecular processes, the theoretical modelling of this phenomenon is important for the interpretation of experimental results. While for atomic or simple molecular systems the theoretical treatment can provide very accurate results, in the case where a large number of atoms is involved, the theoretical modelling of the quantum dynamics far from equilibrium and the interpretation of experimental

signals remain as remarkable challenges for contemporary molecular physics [25,60]. In the context of pump-probe spectroscopy, the complexity lies not only in the large number of degrees of freedom, but also in the variety of intermolecular interactions and in the interaction of the system with external fields.

To our knowledge, dynamical time-resolved studies of ultrafast phenomena in quantum many-body systems are very scarce in the literature. Among the investigations carried out so far, the studies about coherence effects on the surface of large He clusters [61], the bubble state formation around Rydberg excited He_2^* dimers in liquid helium [62] and the structural relaxation of rare gas and normal-hydrogen solids [3, 15] must be highlighted. These works have been complemented by a much larger number of spectroscopic studies in the frequency domain [32,63–67] and computer simulations [68–72].

In recent years, the techniques based on the path integral formulation of quantum mechanics [73–75] and the methods of resolution of the time-dependent Schrödinger equation for many-body systems, such as the multiconfigurational time-dependent Hartree (MCTDH) approach [16, 17, 76, 77], have experienced a significant progress. The main limitation of these methods is the fast increase of their computational cost as the number of degrees of freedom of the system, or the number of configurations, gets larger. In particular, with the computational resources available nowadays, the quantum description of the dynamics of thousands of atoms is still out of reach. Therefore, in spite of the continuous development of these quantum approaches, classical molecular dynamics (MD) simulations still constitute the standard tool for the study of dynamical processes in condensed phase, owing to the high computational cost of the more sophisticated simulation methods [1, 4, 6, 7, 14, 23, 46, 50]. The modification of the dynamical state of the system in phase space, according to the laws of classical mechanics, is local. This local character implies a tremendous saving of both the

memory allocation and calculation time requirements for the numerical integration of the equations of motion, compared to the solution of the corresponding quantum problem. However, the behaviour of macroscopic systems where quantum effects are present can not be correctly described by a purely classical treatment [15,59,60].

Because of the complexity of the rigorous quantum treatment of systems with many degrees of freedom, many approximations have been proposed in the past, with the aim to incorporate quantum delocalization effects into MD simulations. That is the case of the Bergsma's approximation, which incorporates the effect of zero-point energy on crystal site oscillations through an effective temperature. The latter is derived using a harmonic approximation of lattice vibrations [19,20]. Several authors have considered Gaussian wave packets instead of point particles [21,25,78]. If all the wave packets are constrained to have the same width, the procedure is equivalent to employing an effective potential, obtained via convolution of the interaction potential with the corresponding Gaussian, in otherwise classical simulations. Both approaches, the introduction of an effective temperature or potential, are approximated by nature and can not account for strong quantum delocalization or correlation effects. On the other hand, the simulation techniques based on the path integral formalism are limited to the calculation of equilibrium properties. Those factors condition the absence of rigorous evaluations of the role played by quantum effects in dynamical processes in condensed phase, and pose the question about what is the magnitude of such effects in the photo-induced structural relaxation of nitric oxide doped neon matrices. An additional limitation of semiclassical methods is that, to simulate the excitation process, it is necessary to assume that the light pulse is extremely short, so the electronic transition can be regarded as instantaneous. This feature limits the possibility to simulate the time-dependent experimental signals.

As stated above, the present thesis focuses in the study of the structural prop-

erties and of the geometrical reorganization of solid *Ne*, as a consequence of the electronic photo-excitation of a *NO* impurity. To carry out a fully quantum mechanical treatment of a system with so many degrees of freedom, we introduce a reduced dimensionality model. Due to the weak anisotropy of the *NO*-*Ne* interaction in the excited state [18, 22], the primordial motion of the *Ne* atoms around the *NO* is, essentially, a radial expansion, which has been termed "bubble formation" [5, 11, 53]. Based on this property, we construct a multidimensional shell model, with the shell radii being the dynamical variables. In this way, we can treat explicitly the quantum many-body dynamics and to examine the static as well as the dynamical properties of the target system.

The main goal of this work is the study of the dynamical response of a neon matrix to the photo-excitation of a nitric oxide impurity to its first Rydberg state. The specific aims of the thesis are:

1. To clarify the characteristics of the motion of *Ne* atoms, which determine the main structural modifications induced by the electronic transition, and the mechanisms of the excess energy redistribution into the lattice.

2. To evaluate the influence of the form of the pump laser pulse on the time evolution of the vibrational wave packet.

3. Employing the pulse parameters which reproduce the form of the excitation and probe pulses used in previous experiments, to simulate the transient spectra and to investigate the relationship between these pump-probe signals and the instantaneous configuration of the system.

4. To evaluate the effect of dynamical correlations on the wave packet propagation and on the computed observables.

In this work, as a contribution to theoretical modelling and simulation of time-dependent phenomena in quantum condensed phase systems, the following novel results are presented:

1. The development of a methodology which allows the numerical simulation of the equilibrium properties and of the dynamical processes in condensed phase, thereby overcoming the limitations of quantitative studies of time-dependent phenomena in those systems, based on semiclassical extensions of the classical MD method.

2. The identification of the primary and secondary mechanisms of redistribution, among the different degrees of freedom of the neon matrix, of the excess energy deposited by the laser during the electronic excitation of a *NO* molecule to its first Rydberg state.

3. The evaluation of the influence of both the finite width and the form of the laser pulse on the dynamics of *NO* doped *Ne* matrices, as well as the interference effects of the vibrational wave packet formed after the excitation of the molecule. These phenomena can not be described by classical simulations.

4. The evaluation of the role of dynamical correlations and their effect on the time evolution of the multidimensional wave packet used to describe the *Ne* solid.

The thesis is divided in seven chapters: *Introduction*, *Physical properties of solid neon*, *Nitric oxide molecule*, *Pump-probe experiments on the structural relaxation dynamics of* NO *doped solid* Ne, *Methodology*, *Results and discussion*, *Conclusions and Recommendations*, the chapters being organized as follows:

In **Chapter 1**, *Introduction*, the motivation and the main objectives of this work are described.

In **Chapter 2**, *Physical properties of solid neon*, is devoted to introduce the general characteristics of the neon crystals, such as the physical and structural properties, as well as the most significant features of the electronic espectroscopy of the pure solid.

In **Chapter 3**, *Nitric oxide molecule*, some properties of *NO* molecules in the gas phase and embedded in a *Ne* solid are presented, with emphasis in those which determine the dynamical response of the matrix to the photo-excitation of the diatomic molecule to its first Rydberg state.

In **Chapter 4**, *Pump-probe experiments on the structural relaxation dynamics of* NO *doped solid* Ne, time-resolved pump-probe experiments of a *NO* molecule embedded in a *Ne* matrix, and the measurement of the bubble or cavity expansion, are described in brief.

In **Chapter 5**, *Methodology*, the shell model, the construction of the potential energy surface of the system, the MCTDH scheme used in the numerical resolution of the time-dependent Schrödinger equation and observables calculation are introduced.

In **Chapter 6**, *Results and discussion*, the results obtained for the stationary properties of the system, such as the static deformations due to the presence of the impurity and the absorption and emission spectra, are analysed in detail. Calculated dynamical properties, as the reduced densities along each degree of freedom, the principal mechanisms of energy dissipation into the solid, the pump-probe spectra, the effects of the finite pump pulse width and of dynamical correlations, among others, are also discussed in this chapter.

Finally, in **Chapter 7**, *Conclusions and Recommendations*, the main conclusions of this work are presented. The thesis finishes with an outlook, especially concerning the possibility to extent the present study to other quantum solids such as $p - H_2$.

Chapter 2

Physical properties of solid neon

Solid neon presents interesting properties which emanate from the light mass of its atomic constituents, compared to the rest of noble gases, and from the weakness of the interatomic Ne-Ne interactions. In the present chapter, the main characteristics of the neon crystal and its importance as a model system are presented, focusing in the quantum character of this solid.

2.1 Structural and physical properties of solid Ne

Rare gas solids have been intensively studied during last decades form both experimental and theoretical points of view. They constitute ideal solvents for the investigation of molecular phenomena, since they are chemically inert and their structure and thermodynamic properties are well characterized in a wide range of pressures and temperatures.

Rare gas atoms, and Ne in particular, present closed shell electronic structures. As a consequence, the cohesive forces in the solid, of the van der Waals type, are very weak and the spherical electron distribution of the rare gas atoms in the gas

phase is approximately conserved in the matrix. This characteristic of the interaction between the atoms, cause the rare gases to crystallize adopting a face-centred cubic (f.c.c.) structure. In the case of neon, the conservation of the spherical symmetry of the electron cloud in the condensed phase, can be understood also in terms of the low polarizability of the *Ne* atoms ($\sim$2.7 a.u.^{3}). The shallowness of the interatomic potential also causes the freezing of rare gas systems to occur only at cryogenic temperatures (the triple point temperature of neon is 24.5 K). As a consequence of the low temperature regime, the equilibrium properties of solid neon are determined by the vibrational ground state of the system. Furthermore, the low temperatures also lead to the reduction of the density of states accessible to the molecules immersed in these medium, thereby facilitating its study.

van der Waals interactions are long range forces between the induced dipoles of the atoms. In the case of rare gases, the interatomic interaction is usually represented by a potential energy curve of the Lennard-Jones (LJ) type, which contains both repulsive (which dominates for small interatomic distances) and attractive (long-range) contributions:

$$V_{LJ}(r) = 4\epsilon \left[\left(\frac{\sigma}{r}\right)^{12} - \left(\frac{\sigma}{r}\right)^{6} \right] \quad , \tag{2.1}$$

where ϵ is the well depth, σ is a characteristic length scale which roughly corresponds to the size of the interacting atoms (σ is equal to the separation between the atoms for which the potential (2.1) vanishes) and r is the interparticle distance. For the rare gas atoms, ϵ is of the order of 0.01 eV. In practice, the parameters ϵ and σ are commonly obtained from the fitting of the thermodynamic properties, taken from the experiment, of the corresponding substances or of *ab initio* calculated interaction energies. In the latter case, these energies correspond to the eigenvalues of the elec-

tronic Hamiltonian, evaluated within the Born-Oppenheimer approximation, which depend parametrically on the separation between the atomic nuclei. Specifically, for the neon solid, ϵ=3.084 meV and σ=5.257 a.u. [79].

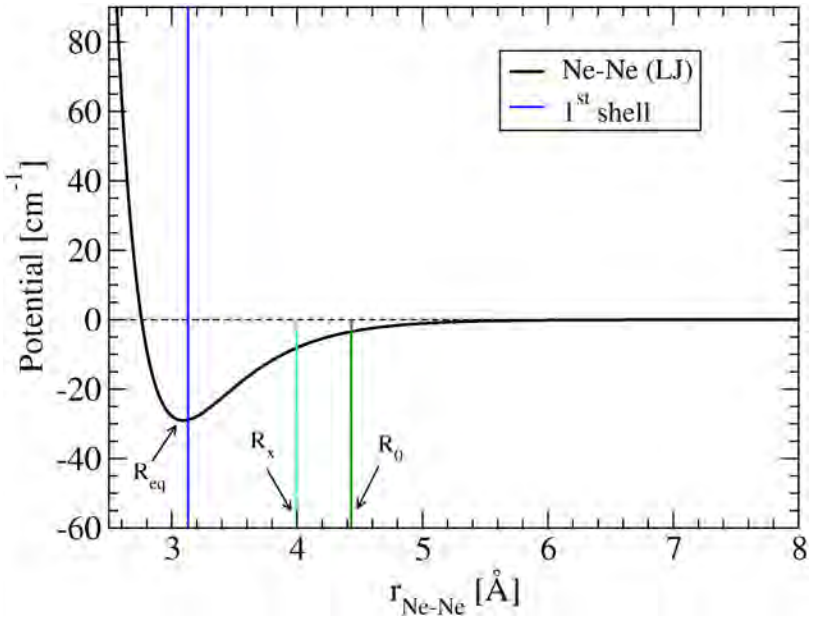

Figure 2.1: *Ne-Ne* interaction potential. r_{Ne-Ne} represents the separation between the Ne atoms. The dark blue vertical line indicates the equilibrium distance between nearest neighbours in the crystal (5.91 a.u.).

In Figure 2.1 the $Ne - Ne$ interaction potential employed in this work [79] is represented. Although more sophisticated forms of the interaction potential have been developed, the correspondence between the experimental data and the simulations performed using these alternative forms is not significantly better than the results obtained with the Lennard-Jones potential, except for the rare gas solids at very high pressures. Since the phenomenon investigated in this thesis take place in matrices produced by direct deposition of the gas in high vacuum environments, i.e., at zero external pressure, it is not necessary to consider three-body contributions to the interaction among Ne atoms.

Some of the structural properties of solid Ne are shown in Table 2.1:

Table 2.1: Structural properties of solid Ne

R_0	d	ρ_{Ne}	m_{Ne}	E_D
8.37 a.u.	5.91 a.u.	1.507 g/cm^3	20.179 u.m.a.	6.45 meV

where R_0 is the lattice constant, d is the nearest neighbour distance, ρ_{Ne} is the mass density of the crystal, m_{Ne} is the mass of Ne atoms and E_D is Debye's energy. In Figure 2.2 it can be observed that E_D constitutes, in fact, the maximum frequency of lattice vibrations. In this graph, it is shown the dependence of the normal mode energies of the system, on the reduced wave vectors $R_0\mathbf{k}/2\pi$. The normal modes frequencies are obtained from theoretical calculations and inelastic neutron scattering measurements [80].

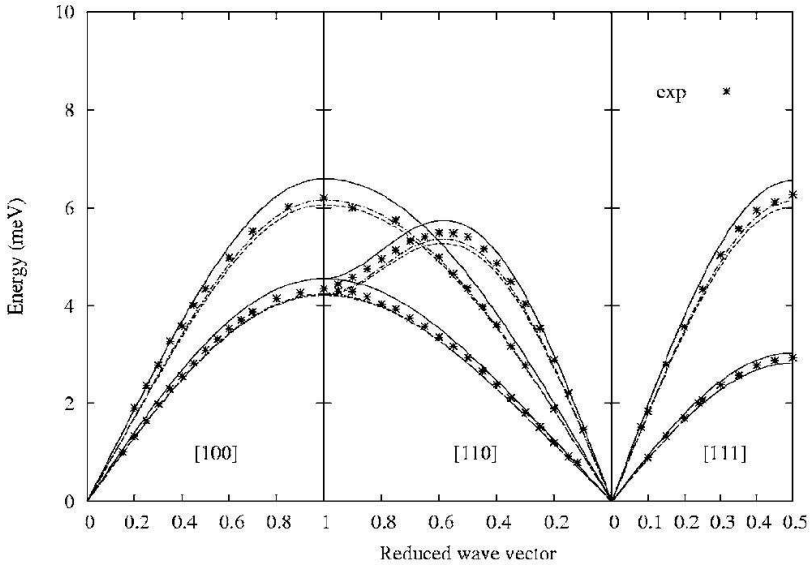

Figure 2.2: Dispersion relations $\omega(\vec{k})$ for the solid Ne.

At zero pressure $p = 0$, the dependence of the structural characteristics of solid neon as function of temperature is relatively weak. For example, the relative increment of the lattice constant, with respect to its value at T=4 K, is of 0.03% at T=8 K, 0.18% at T=12 K and 0.95% at T=20 K [79].

2.2 Quantum effects and anharmonicity

Although most of rare gas matrices can be regarded as classical systems, this hypothesis is not valid for the lighter rare gases, *He* and *Ne*. The *Ne* solid has been centred the attention of many condensed phase studies because, being composed by atoms of intermediate mass, it allows a deeper understanding of the role played by quantum effects via the comparison with other systems which exhibit a more pronounced classical or quantum behaviour.

The quantum character of the system can be defined using the parameters of the Lennard-Jones potential. Taking into account the functional form of this interaction potential (2.1), it is easy to verify that $V(\sigma) = 0$ and $V(R_{eq}) = -\epsilon$, where R_{eq} corresponds to the minimum of the potential. Assuming that the potential energy surface of the system can be obtained as a superposition of the contributions due to the interaction between each pair of particles, the Hamiltonian of the solid can be rewritten in dimensionless form:

$$H^* = -\frac{1}{2}\lambda^2 \sum_i \nabla_i^{*2} + \sum_{i>j} V^*(R_{ij}^*) \quad . \tag{2.2}$$

The superscript * indicates that the distances and energies are expressed, respectively, in units of σ and ϵ: $H^* = H/\epsilon$, $R_{ij}^* = R_{ij}/\sigma$. The de Boer parameter,

$$\lambda = \frac{\hbar}{\sigma(m \cdot \epsilon)^{1/2}} \quad , \tag{2.3}$$

where m is the atom mass, provides a quantitative estimation of the importance of quantum effects in condensed phase, at $T = 0$. Roughly speaking, this parameter evaluates the spread of the wave function of a single atom, with respect to the characteristic length scale of the confinement potential. For $\lambda \ll 1$, the system behaves

classically, and quantum effects become more noticeable as the value of λ gets larger. For the different rare gas and para-H_2 solids, the values taken by the de Boer quantum parameter are: 0.398 (He), 0.274 (para-H_2), 0.095 (Ne), 0.030 (Ar), 0.017 (Kr), 0.010 (Xe). In the case of Ne, this parameter is nearly three times larger than the corresponding value for Ar.

The quantum character of solid Ne is also evidenced by the fact that its bulk modulus, $B_0^{(cl)} = 75\epsilon/\sigma^3$, calculated classically, does not coincide with the experimental value reported for this magnitude. The deviation between the theoretical and experimental values of B_0 is of 60 % for Ne, 20 % for Ar and it is essentially zero for the heavier rare gases, Kr and Xe. This dependence on the mass of the atoms suggest that the discrepancy between the theoretical and experimental values owes to zero-point energy effects, which are disregarded in the above calculation. This is an example of the systematic deviation of the thermodynamic properties of neon from the law of corresponding states. The latter is based on the prediction, by classical statistical mechanics, that all substances, whose constituents interact according to the law $\epsilon V(r/\sigma)$, should have the same equation of state, if properly rescaled. The deviation of neon properties, with respect to the heavier rare gas atoms, has been experimentally established and it is attributed to quantum effects.

Quantum corrections to neon properties lead, for example, to the reduction by 1.4 K of its triple point temperature, indicating that such effects are important in the whole range of temperatures corresponding to the solid phase. Furthermore, quantum effects modify the critical pressure, volume and temperature of the liquid-gas transition, but the critical exponents calculated classically remain unchanged. On the other hand, the average kinetic energy per atom in solid neon at T=0 K is, in temperature units, of 41.5 K [81]. This is a clear indicator of the magnitude of zero-point energy effects in the crystal. As a consequence of this energy value, the

Table 2.2: Wave vectors $\vec{k}$, transversal (T) or longitudinal (L) characters and energies $\hbar\omega$ of some lattice phonons with lowest and highest frequencies in solid neon. The energies $\hbar\omega_0$, calculated within the harmonic approximation, are also included.

$\vec{k}$ $(2\pi/R_0)$	Carácter	$\hbar\omega$ (meV)	$\hbar\omega_0$ (meV)
(1/5,0,0)	T	1.41	1.22
(1/5,1/5,0)	T_1	1.34	1.24
(1/5,1/5,1/5)	T	1.85	1.66
(1/5,0,0)	L	1.95	1.70
(1/5,1/5,0)	T_2	2.00	1.72
(1,0,0)	T	4.67	3.94
(1,0,0)	L	6.98	5.51

mean square displacement of a Ne atom, about its equilibrium position in the lattice, reaches 9.1% of the nearest neighbours distance. For the H_2, D_2 and Ar solids, at T = 0 K, such ratio take the values 18%, 14% and 5%, respectively.

Due to the significant amplitude of zero-point motions, anharmonic effects also play an important role in solid Ne [79], [81]. In Table 2.2, the energies of some of the vibrational modes with the lowest and the highest vibrational frequencies are listed. The magnitude of anharmonic contributions can be assessed by comparing the energies calculated taking into account ($\hbar\omega$) and neglecting ($\hbar\omega_0$) their influence on lattice oscillations [79]. It can be seen, that the phonon frequencies computed within the harmonic approximation underestimate those obtained considering the full potential. The differences vary between 7% and 21% of the highest value.

It is worth to notice, that with respect to anharmonicity, the Ne crystal also constitutes an intermediate system between para-hydrogen and the rest of rare gas solids. The structural properties of solids as, for example, the lattice constant R_0, are continuous functions of λ. For classical solids ($\lambda \ll 1$), the nearest-neighbour distance approaches the equilibrium separation of the $Ne-Ne$ interatomic potential, while for larger values of λ, for systems of light atoms or molecules, the lattice constant increases to minimize the energy of the solid. If $d = R_0/\sqrt{2}$ exceeds the value

corresponding to the inflection point of the potential ($d > R_x$, where $V''_{LJ}(R_x) = 0$), as it happens for the $p - H_2$ solid [41], the frequencies of some harmonic modes can become imaginary and the results of the normal mode decomposition become inadequate to describe the vibrational properties of the solid. The presence of normal modes with imaginary frequencies implies that the equilibrium configuration of the solid is unstable in the harmonic approximation. In Figure 2.1, it can be seen that for the neon solid, nearest neighbour atoms are separated by a distance d which is only slightly larger than the equilibrium distance R_{eq} of the $Ne - Ne$ potential.

Previous studies on the relaxation dynamics of pure and NO doped neon solids, incorporated the effect of zero-point energy on crystal site oscillations into classical MD simulations through an effective temperature T_B. The latter was obtained by equating the diagonal elements of the quantum density matrix of a harmonic oscillator, evaluated at the physical temperature T, to the classical distribution corresponding to this potential, in thermodynamic equilibrium at the temperature T_B. As an illustrative example, the effective temperature used to mimic the zero-point energy effects in the neon solid at the experimental conditions (T= 4 K), is above the fusion point of the crystal [4,7,20]. The possibility to incorporate anharmonic contributions in the derivation of the effective temperature was explored in Ref. [20]. The new quantum correction is based on an analytical expression for the density matrix of an isotropic anharmonic oscillator, considering the fourth power of the displacement, with respect to the equilibrium position, as a perturbation:

$$U(r) = \frac{m}{2}\omega^2 r^2 + gr^4 \tag{2.4}$$

The resulting expressions for the new effective temperature T_{cl}, the oscillation fre-

quency ω and the anharmonicity constant g

$$T_{cl} = \frac{T_B}{1+\frac{3gkT_B}{(m\omega^2)^2}\tanh^2\left(\frac{\hbar\omega}{kT}\right)} \quad , T_B = \frac{\hbar\omega}{2k}\left[tanh\left(\frac{\hbar\omega}{2kT}\right)\right]^{-1} \tag{2.5}$$

$$\omega = \left[\frac{8\epsilon}{m}\sum_s \frac{N_s}{R_s^2}\left(\frac{\sigma}{R_s}\right)^6\left\{22\left(\frac{\sigma}{R_s}\right)^6 - 5\right\}\right]^{1/2} \tag{2.6}$$

$$g = \frac{28\epsilon}{5}\sum_s \frac{N_s}{R_s^4}\left(\frac{\sigma}{R_s}\right)^6\left\{143\left(\frac{\sigma}{R_s}\right)^6 - 10\right\} \tag{2.7}$$

show that the effective temperature T_B, evaluated within the harmonic approximation, is always larger than the value at which the classical and quantum distributions become similar. In the previous set of equations, N_s is the number of particles in each coordination shell, which is labelled by the index s and it is formed by all atoms located at the distance R_s from a lattice site which is chosen as the origin. Since $g \sim \epsilon$ and $\omega \sim \sqrt{\epsilon/m}$, it can be seen that the anharmonic correction to the effective temperature is proportional to $1/\epsilon$ (equation (2.5)), while the influence of the characteristic length of the interaction potential, σ, is contained in the sums in formulas (2.6) and (2.7). Therefore, the overestimation of the effective temperature is directly related to the main features of the interatomic potential energy curve, being more relevant in the case of the more weakly bound systems.

The results of the classical MD simulations of NO doped neon matrices have been revised, taking into account this improved representation of zero-point energy effects [7]. In Table 2.3, the calculated centroids and widths of the stationary absorption and emission bands, corresponding to the transitions between the electronic ground state and the first Rydberg state of NO in a Ne matrix, are reported.

It can be observed that the new quantum correction improve the correspondence between the simulations and the experimental spectroscopic results. Nevertheless, in spite of the use of impurity-rare gas interaction potentials fitted to reproduce the

Table 2.3: Mean values ($< E >$) and widths (ΔE) of the absorption and emission bands, calculated via MD simulations carried out at the effective temperatures derived using the harmonic approximation (T_B) and its extension to the case of anharmonic potentials (T_{cl}). Numbers in parenthesis indicate deviations (given in percentage) with respect to the corresponding experimental values.

Absorption		
	$< E >$ (eV)	ΔE (eV)
Exp.	6.439	0.153
T_B	6.447	0.191 (24.8%)
T_{cl}	6.440	0.136 (11.1%)
Emission		
	$< E >$ (eV)	ΔE (eV)
Exp.	5.646	0.068
T_B	5.677	0.050 (26.5%)
T_{cl}	5.666	0.061 (10.3%)

measured condensed phase spectra [4], appreciable deviations, between the empirical bands widths and the theoretically calculate values, still persist. Such differences show that it is not possible to reproduce the dynamical properties of solid neon using semiclassical approaches, pointing to the importance of applying a rigorous quantum treatment of the photoinduced structural relaxation in this system.

2.3 Electronic bubble formation in electronically excited solid neon

Rare gas atoms form weakly bound van der Waals solids, where the individual constituents retain their atomic character. The first electronic transition of the rare gas solids lies in the ultraviolet spectral range, since the energy required is above 8 eV. This transition corresponds to the excitation $np^6 \rightarrow np^5(n+1)s$ of one atom to its lowest energy Rydberg state, forming what is known as the $n = 1$ Frenkel exciton [82,83]. The Rydberg states of atoms and molecules, corresponding to small values

of the main quantum number, are characterized by radii of the electronic orbitals of the same order than the nearest neighbour distance in the rare gas crystals. Hence, the excitation of this electronic state causes a strong electrostatic repulsion on the neighbouring atoms, due to the overlap of the Rydberg orbital with the closed shell species that surround the excited centre, and it induces a substantial reorganization of the lattice around the $n = 1$ exciton.

The stationary electronic spectroscopy (both absorption and fluorescence) of the neon solid has been extensively studied [82, 84–92]. In this case, the formation of $n = 1$ Frenkel atomic excitons corresponds to the excitation $3p^6 \rightarrow 3p^5 4s$ of the first Rydberg state of the neon atom. As a consequence of the strong repulsion between the Rydberg electron and the closed shell surrounding atoms, the absorption band presents a pronounced blue shift, with respect to the corresponding spectral line in the gas phase [82–92]. This interaction induces the relaxation of the cavity around the excitation centre towards a new equilibrium configuration, from where fluorescence takes place. The large Stokes shift, i.e., the separation between the centroids of the absorption and emission bands, indicates that a large scale reorganization of the lattice occurs in the vicinity of the excited species [82, 84–86]. The basic mechanism consists in the outwards displacement of the surrounding atoms from the optically activated centre, leading to the formation of a cavity around it (electronic bubble).

This relaxation process has been theoretically investigated, employing analytical methods [93,94] as well as simulations based on minimization procedures [2,89,95,96]. In both cases, the key hypothesis is that the deformation possesses radial character. Those calculations confirm that the lattice expands considerably around the excited neon atom: the first coordination shell is displaced by approximately 1.9-2.3 a.u., which corresponds to an increase of 30-37% with respect to its original radius.

On the other hand, the role played by quantum effects in the real-time energy

redistribution mechanisms, associated to the restructuring of the solid around the excited Ne, remains unclear. This is due to the inherent limitations of the classical MD simulations, which constitute the most extended tool for the description of the structural dynamics of condensed matter. Albeit such methods have been successfully applied to the description of the photoinduced dynamics of molecules embedded in some rare gas solids [1, 2, 55, 97] and clusters [98–100], they are restricted to media where zero-point fluctuations are negligible with respect to typical intermolecular distances. Moreover, time-resolved experiments of the ultrafast lattice relaxation around the $n = 1$ exciton are presently out of reach, since it is not possible to access to exciton's energies ($\sim$16.85 eV) with the nowadays femtosecond laser technology. Additionally, for this process, the definition of suitable observation windows for the probe lasers becomes problematic. As will be discussed in the next chapter, the spectroscopic characteristics of the first Rydberg state of the NO molecule are similar to those of the $n = 1$ Frenkel exciton in solid neon, while it presents the advantage of being accessible by the modern pump-probe technology.

Chapter 3

Nitric oxide molecule

The study of the physical and chemical properties of the nitric oxide molecule, NO, in biological environments is a problem of great interest, because this molecule is present and plays an important role in many processes in the atmosphere and in the physiology of animals and plants. Initially pointed out as a cancerous agent, a dangerous element for the ozone shell and a precursor of acid rain, investigations carried out in recent years suggest that NO have an active role in the functioning of the human brain, the nervous terminals, the arteries, the immune system, the leaver, the pancreas and the uterus. In spite of being a simple molecule, the NO has multiple applications related to, for example, human health (as a blood vessel dilator and in the treatment of lung hypertension), in the agriculture (as a component of fertilizers) and in the chemical industry (as an intermediate compound in the synthesis of ammonia). NO is one of the elements of the nitrogen cycle in earth's atmosphere [101] and it is intimately related to the metabolism of plants (as antioxidant, regulator of the genetic expression, etc.). In 1998, the Nobel Prize of Medicine and Physiology was awarded to Robert F. Furchgott, Louis J. Ignarro and Ferid Murad, because of their discoveries concerning the role of nitrogen oxide as a signaling molecule in the cardiovascular

system.

Rare gas matrices provide an ideal host for the study of the molecular properties of NO and its interaction with the surroundings. Furthermore, these matrices constitute, due to their physical properties and the nature of their interactions, the simplest model of a biological system. The study of the NO molecule is relevant, not only because of its importance in biological processes, but also because the phenomenology associated to the excitation of its first Rydberg state, in neon matrices, is very similar to that of the $n = 1$ Frenkel exciton in the pure solid. Additionally, this Rydberg state posses the characteristic of being spectroscopically accessible. In the following sections, the main properties of NO in the gas phase and the essential features of the process of formation of the electronic bubble, in Ne matrices doped with this impurity, will be described.

3.1 Electronic states of *NO*

Nitric oxide is a highly reactive open shell molecule. It has 15 electrons, 8 coming from the oxygen atom and 7 from nitrogen, distributed among the molecular orbitals. The electronic structure of the molecule corresponds to [43]:

$$(1s_O\sigma)^2(1s_N\sigma)^2(2s_O\sigma)^2(2s_N\sigma)^2(2p_O\sigma)^2(2p\pi)^4(2p_N\pi)^1 \quad . \tag{3.1}$$

Its high reactivity is determined by the single electron that occupies the antibonding orbital $2p_N\pi$. In the excited valence states, the antibonding $2p\pi$ orbital is populated, causing a stronger repulsion between the atomic nuclei. The excitation of these valence states does not provoke the variation of the main quantum number n, so the dimensions of the electronic cloud of the molecule does not suffer considerable

changes. Contrary to valence states, in the process of excitation of the first Rydberg state, the orbital $2p\pi$ becomes unoccupied and the electron goes to the orbital $3s\sigma$, favouring the attractive interaction forces. In this case, the internuclear distance is smaller than for the ground electronic state, X, because the antibonding orbital is empty. On the other hand, the size of the electronic cloud of the molecule increases, due to the change of the main quantum number, proportionally to n^2 [44].

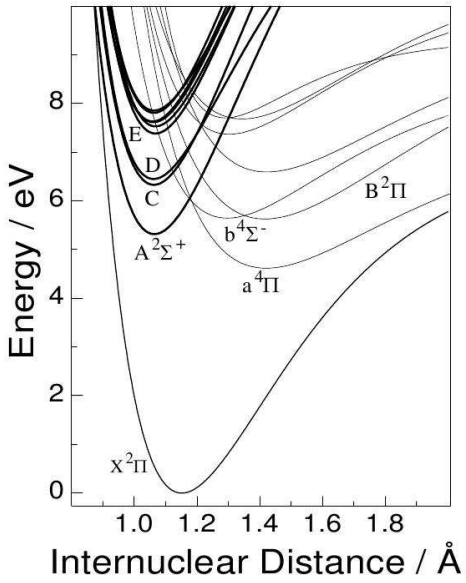

Figure 3.1: Potential energy curves of the Rydberg and valence states of the *NO* molecule in the gas phase. Thick lines correspond to the Rydberg states. It can be observed, that these states are practically parallel and that they have similar equilibrium radii. The bond distances of Rydberg states are smaller than the equilibrium radius of the ground state, X.

All the Rydberg states of *NO* have potential energy curves which are practically parallel among them. This feature implies that these states exhibit similar oscillation frequencies and they have almost the same equilibrium distance between nuclei. In Figure 3.1, the potential energy curves of Rydberg and valence states of *NO* are illustrated. On the other hand, the electronic structure of these orbitals is shown in Figure 3.2.

The energies of Rydberg states can be expressed as function of the ionization

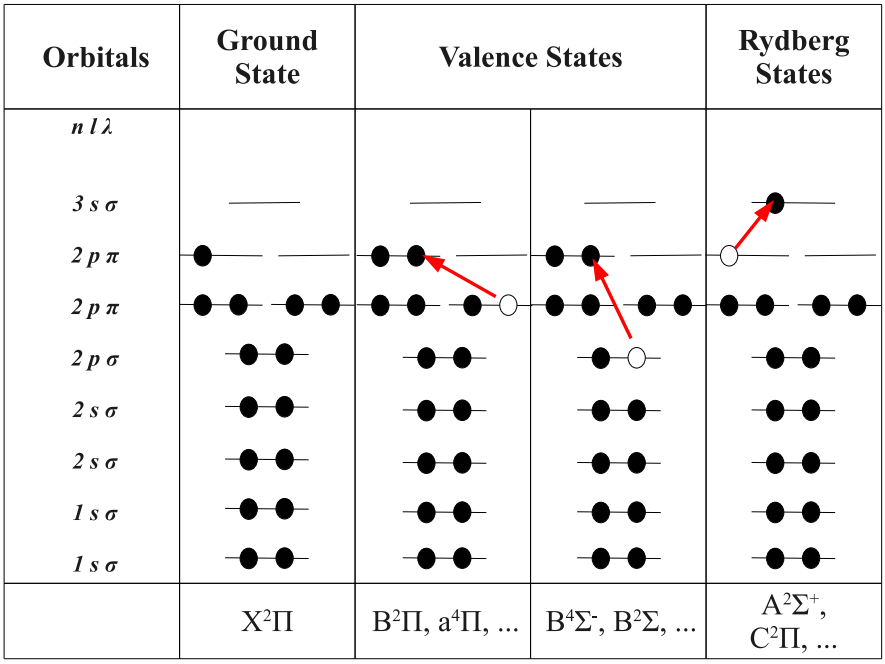

Figure 3.2: Diagrammatic representation of the electronic structure of the molecular orbitals of *NO*. The notation $nl\bar{\lambda}$ denotes the antibonding orbitals.

potential, E_{ion} (9.26 eV), and the Rydberg constant, R (13.6 eV): $E_n = E_{ion} - \frac{R}{(n-\delta_n)^2}$. The magnitude δ_n, known as "quantum defect", is a parameter that describes to what extent the Rydberg electron penetrates into the electron cloud corresponding to the inner shells of the molecule. As this value gets larger, there will be a more significant penetration of the Rydberg orbital, so the positive ionic core will exert a stronger attraction on this electron. The average radius of the electronic orbital corresponding to each state can be calculated using the expression [45]

$$\langle r_{elec} \rangle = \frac{1}{2}[3(n-\delta_n)^2 - l(l-1)]a_0 \tag{3.2}$$

where a_0 is the Bohr radius.

In Table 3.1, some of the molecular constants of *NO* in the gas phase are shown. It is important to notice, that for the first Rydberg state, $A^2\Sigma^+$, both the quantum

Table 3.1: Molecular constants of *NO* in the gas phase. E_{00} is the energy difference with respect to the ground state, R_e is the equilibrium distance between the nuclei, δ is the quantum defect and $\langle r_{elec} \rangle$ is the average radius of the orbital.

State	$nl\lambda$	E_{00} [eV]	R_e [a.u.]	δ	$\langle r_{electr.} \rangle$ [a.u.]
$X^2\Pi$	$2p\pi$	-	2.175	0.786	1.32
$A^2\Sigma^+$	$3s\sigma$	5.465	2.009	1.104	5.48
$C^2\Pi$	$3p\pi$	6.478	2.007	0.782	-
$D^2\Sigma^+$	$3p\sigma$	6.593	2.005	0.735	-
$E^2\Sigma^+$	$4s\sigma$	7.531	2.016	1.186	12.09
$B^2\Pi^+$	$2p$	5.692	2.677	-	-
$b^4\Sigma^-$	$2p$	5.72	-	-	-
$a^4\Pi$	$2p$	4.68	2.674	-	-

defect and the average radius of the orbital are relatively large. The average radius of the Rydberg electron, 5.48 a.u., is comparable to the distance between nearest neighbours in the neon crystal (5.91 a.u.). This characteristic becomes relevant in the case that *NO* occupies a substitutional site in a *Ne* crystal, and the molecule is excited to its first Rydberg state, $A^2\Sigma^+$, since it can be expected that the interaction between the molecule with the closeby *Ne* atoms will be purely repulsive, leading to the formation of a electronic bubble. In the following section this phenomenon will be described.

3.2 *NO* doped *Ne* matrices: model system to study the formation of electronic bubbles

The spectroscopic properties (spectral shifts, widths of the absorption and emission bands and Stokes shift) of the first Rydberg state of nitric oxide are very close to those of the $n = 1$ exciton in pure *Ne* solid. These properties can also be interpreted in terms of the model of electronic bubble formation [6,45,59]. Furthermore, since the

excitation energy of the molecule is considerably smaller than that of lattice excitons, the transition to the Rydberg state leads to a purely structural relaxation of the matrix, avoiding the additional complexity due to the probability of the exciton to transit between atomic centres.

Among the wide variety of possible molecular targets, the first Rydberg state ($A^2\Sigma^+$) of NO in Ne crystals is very amenable for femtosecond spectroscopy experiments [1, 2, 43–46, 102]. This state possesses two fundamental characteristics which make it very attractive: the dimensions of the electronic orbital are similar to the nearest neighbour distance in the crystal, and the decay time of the state is of approximately 200 ns, five orders of magnitude larger than the time that takes the system to reorganize itself and to reach the new equilibrium positions in the excited state. To make the first of this characteristics more striking, in Figures 3.3 and 3.4 the electron densities of NO in this state are shown, for the free molecule and for the molecule embedded in an argon matrix, respectively [103].

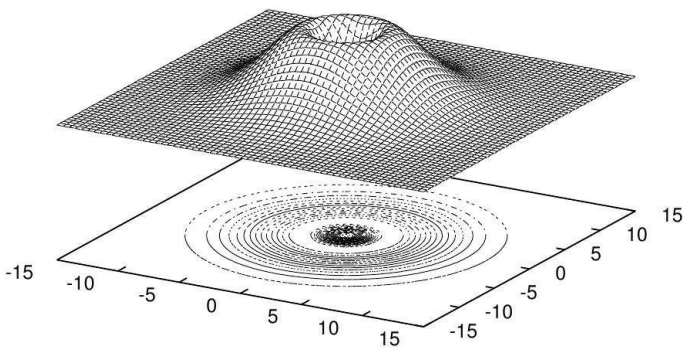

Figure 3.3: Electron density corresponding to the Rydberg orbital A of NO in the gas phase. It can be seen that the excited state is almost spherically symmetric. The distances along both Cartesian axes are expressed in Å.

In these graphs, it is observed that the Rydberg orbital of NO is strongly perturbed for the presence of the matrix and a strong repulsive interaction characterizes the zones occupied by Ar atoms. In the case of solid Ne, these phenomenon is even

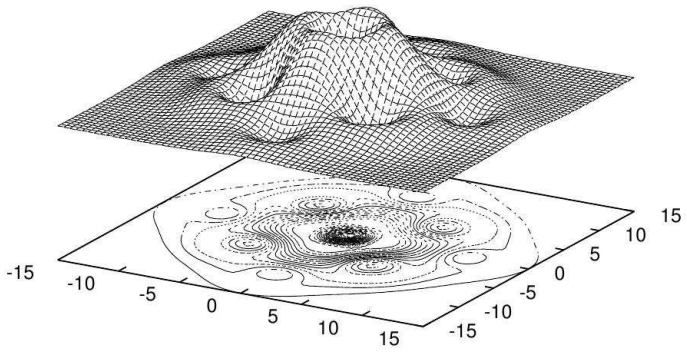

Figure 3.4: Electron density corresponding to the Rydberg orbital A of NO embedded in an argon matrix. It can be seen that the presence of the closeby rare gas atoms in the matrix significantly perturbs this orbital. The distances along both Cartesian axes are expressed in Å.

more pronounced, since in this matrix the atoms are located closer to each other (the density of solid Ne is the largest among the rare gas crystals).

On the other hand, the relaxation dynamics of NO doped neon matrices upon optical excitation of the first Rydberg state of the molecule, leads to the formation of a spherical microcavity, similar to those reported by both theoretical studies as well as stationary spectroscopy experiments on excited neon atoms in neon matrices [82,83] and on neutral atoms (alkaline-earth and alkaline atoms) in liquids [104–109]. The hypothesis of a radial motion of the atoms near the impurity is reasonable, since the $3s\sigma$ orbital of the A state conserves, to a large extent, its spherical symmetry. In Figure 3.5 it can be observed, that the potential energy surface corresponding to the excited state of the $NO(A) - Ne$ triatomic complex is practically isotropic.

The mechanism of formation of an electronic bubble is shown schematically in Figure 3.6. The excitation of NO consists in promoting the unpaired electron to the Rydberg orbital, A. Pauli repulsion forces between this electron and the electronic clouds of the atoms in the first coordination shell in the Ne matrix, pushes those atoms away from the impurity centre, leading to the formation of a spherical cavity. The reorganization of the atomic nuclei is accompanied by a cascade of non radiative

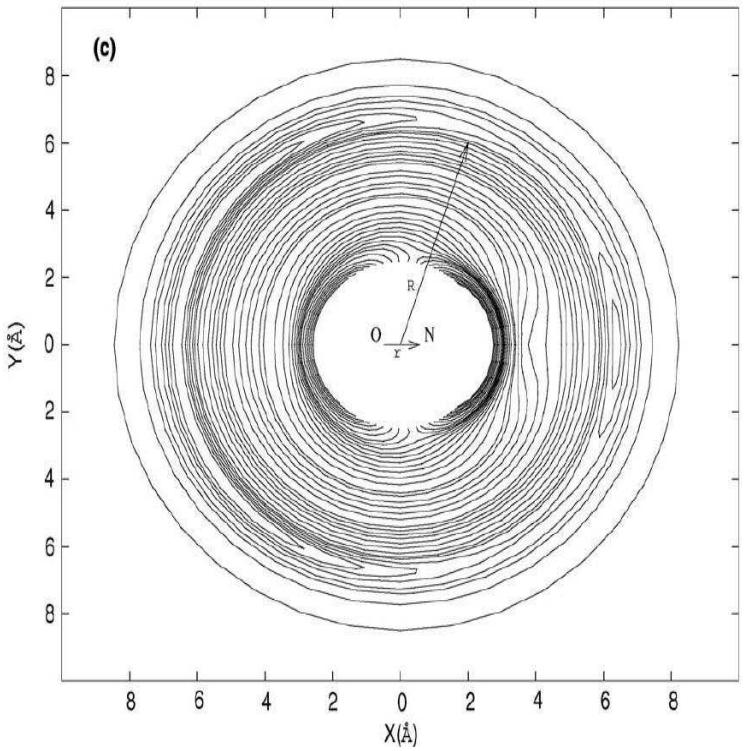

Figure 3.5: Potential energy surface of the $NO - Ne$ complex, corresponding to the first Rydberg state of nitric oxide. It is observed that this interaction potential approximately possesses spherical symmetry [18].

relaxation events, which occur in a time scale (of the order of picoseconds) much smaller than the decay time of the Rydberg state to the ground or valence states. Once the expanded shell reach its new equilibrium position, the system stays in the A electronic state for a few hundreds of nanoseconds. After this time interval have passed, the system returns to its electronic ground state. It is worth to notice, that the transition to the electronic ground state takes place from the equilibrium position of the matrix corresponding to the A state of the molecule. Finally, after the fluorescence have occurred, the cavity contracts back to its initial configuration.

The electronic bubble model has been applied to the interpretation of the process of structural relaxation, triggered by the excitation of the A state of a NO impurity, in rare gas matrices (such as argon, neon, hydrogen and deuterium) [3–5, 7, 15, 52, 53, 56–

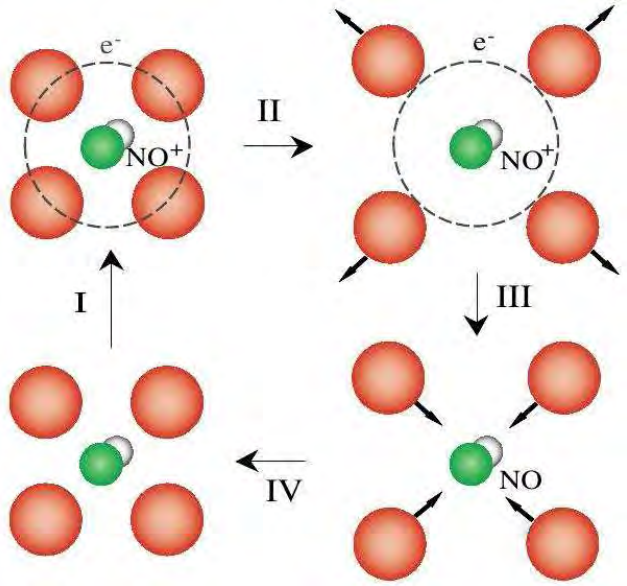

Figure 3.6: Schematic representation of the mechanism of bubble formation. Step I: Excitation of *NO* to its first Rydberg state. Step II: Dynamics and formation of the electronic bubble and reaching of the new equilibrium. Step III: Fluorescence to the ground state of *NO*. Step IV: Vibrational relaxation in the electronic ground state towards the equilibrium configuration.

59]. These studies have focused on the description of the stationary spectroscopy and the modelling, using classical MD simulations, of these systems. However, a rigorous quantum treatment of the nuclear dynamics, in matrices where quantum delocalization effects are important, is still lacking. For such matrices, the correspondence between theoretical and experimental results and, as a consequence, the validation of the mechanism of bubble formation, are limited by the approximate nature of the methodologies of simulation employed so far. Moreover, the impossibility to take into account explicitly, in MD simulations, the time dependence of the laser pulses, prevents to establish the relationship between the experimental transients (e.g., transient absorption spectra) and the microscopic motion of the atoms.

In this thesis, the dynamics of this relaxation process is investigated, via the numerical resolution of the time-dependent Schrödinger equation, using a shell model

which enables a significant reduction of the number of dimensions of the Hilbert space of the real system.

Chapter 4

Pump-probe experiments on the structural relaxation dynamics of *NO* doped solid *Ne*

This chapter offers an overview of the application of femtosecond spectroscopy to the investigation of solid *Ne* doped with a nitric oxide molecule. The first section makes a brief survey of the fundamentals of pump-probe techniques. In the second section, the time-domain and stationary spectroscopic experiments on the excited states of a *NO* molecule in solid *Ne*, simulated in this work, are described.

4.1 Fundamentals of femtosecond spectroscopy: pump-probe technique

The insertion of small concentrations of molecular species in a solid or a liquid constitutes a very useful procedure to study the interactions between these species and the surrounding media. The solute molecule can be selected in such a way, that

its optical absorption band does not interfere with that of the solvent. This feature allows to access the electronic levels of the molecule, thus obtaining truly local information. Although in this case it is only possible to measure the optical absorption of the molecule, the energies of its electronic states reflect the influence of the solvent media.

The electrostatic or dispersion interactions between the impurity and its environment provoke energy shifts with respect to the electronic energy levels in the gas phase. These interactions can change the geometry of the guest molecule, leading to an additional shift of its electronic states. The influence of the media is revealed not only in the displacement of the absorption spectral line of the impurity with respect to the gas phase, but also in the broadening of this line due to the coupling between the electronic states of the impurity and the lattice phonons. Therefore, the measurement of the transition energies between the electronic states of an embedded molecule in a condensed phase material constitutes a valuable experimental tool. It provides information about the interaction between the impurity and the surrounding media through, for instance, the broadening of the spectral lines, and also about the dynamical processes taking place around the impurity, that can be inferred from the study of the spectral shift between the centroids of the absorption and emission bands.

The traditional spectroscopy is based on the use of an electromagnetic wave train that can be regarded as infinitely long. These monocromatic waves trigger elementary excitations of the system with very well defined energies. Due to this feature, this technique is known as frequency-resolved spectroscopy. On the other hand, in femtosecond spectroscopy set-ups, the electromagnetic field interacts with the sample during time intervals much shorter than the time-scale of the process under study. As a consequence, the electromagnetic pulse contains a finite, but relatively large

frequency range. The pulse action is very localised in time, allowing to follow and to register atomic motions (which has typical velocities of around 1 km/s) of the order of 2 a.u., if a pulse with time-resolution of around 100 fs (i.e., the average time one atom needs to cover 2 a.u.) is used. The novel techniques of ultrafast laser pulse generation have enable the direct exploration of processes occurring within such spatial and temporal scales.

The pump-probe experimental technique was born around the year 1950, when the first studies at the microsecond time scale were reported. In such experiments, the photolysis induced by intense light bursts was studied [110,111]. The light created radicals in the sample and, using another light pulse, the spectra of these radicals were recorded. With the aid of these pioneering experiments, it was possible to observe intermediate relatively stable molecular species. Shortly after the construction of the first ruby laser, the generation of electromagnetic pulses of very short duration and great intensity became accessible. In 1961, the time-width of the lasers achieved the order of nanoseconds [112] and of picoseconds in 1966 [113]. In 1987, the first femtosecond laser was obtained with a width of 6 fs [114]. After the introduction of the solid-state Ti-sapphire lasers in 1991, the generation of femtosecond pulses became a standard laboratory tool to study molecular spectroscopy [102]. In 1999, the Nobel prize in chemistry was awarded to the American scientist, born in Egypt, Prof. Ahmed H. Zewail, for his contribution to the field of femtosecond spectroscopy and its application to the chemical reactions in condensed phase. In Figure 4.1 the characteristic time-scales of some fundamental processes in physics, chemistry and biology, are shown.

In order to study the molecular processes occurring in femtosecond time-scales, it is necessary to control the relative time delay between the pump and probe events. To this aim, the pump and probe pulses are produced synchronously. Afterwards,

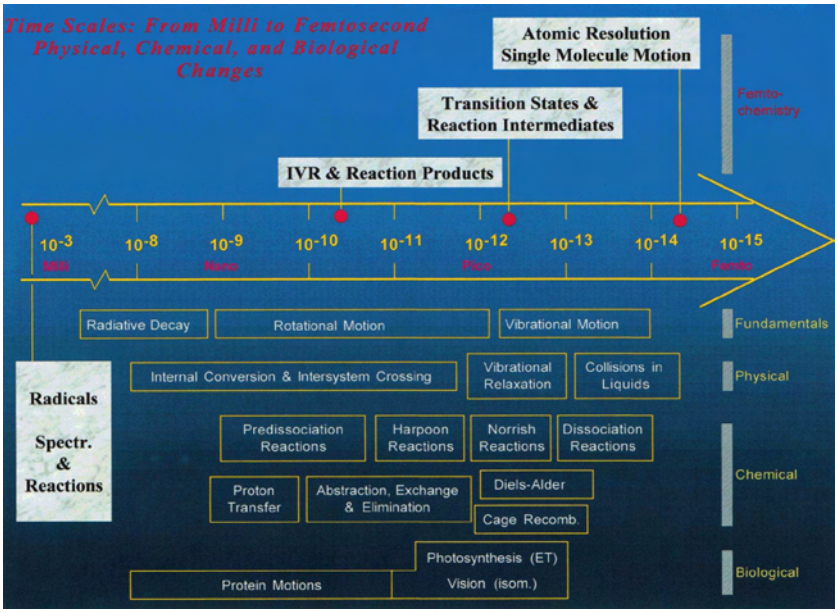

Figure 4.1: Characteristic time-scales of molecular processes in physics, chemistry and biology (given in seconds). Taken from Ref. [115].

the second pulse is delayed with respect to the first one by forcing the probe laser to travel across a path of variable optical length. The finite velocity of propagation of the light traduces this optical path into a difference between the arrival times of both pulses to the sample. For instance, if the probe pulse travels an additional distance of 1 μm, this is equivalent to a delay of 3.3 fs with respect to the pump pulse. The scheme of Figure 4.2 illustrates a typical femtosecond experimental set-up: the first (pump) pulse arrives to the sample and photo-excites the impurity or the optically active centre, and triggers the dynamical reorganization of the surrounding media. The second (probe) pulse arrives to the sample, delayed in time with respect to the former, and induces a transition to a higher excited state. In this way it is possible to measure the transferred population by observing the fluorescence of the latter state.

The fluorescence induced by the second pulse was the first probe method used, but alternative techniques such as mass spectroscopy and non-linear optics were incorporated later. At present, a large number of different probe methods coexist and

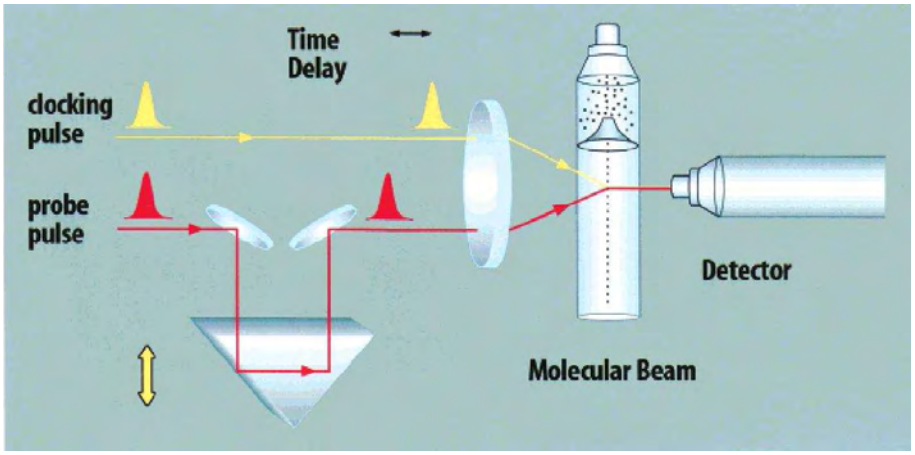

Figure 4.2: Pump-probe experiment scheme. Taken from Ref. [115].

novel techniques are continuously developed, the Coulombic explosion (used for the detection of transition states) being one of the most recent ones.

Depending on the spacing between the system energy levels, two different scenarios are possible: if the difference between two consecutive energy levels of the molecular target are much larger than the energy spread of the probe laser photons, then only one of these eigenstates will be excited, assuming a resonant laser frequency. On the contrary, if the interval of photon energies is larger than the spacing between the levels, the laser pulse will induce the creation of a vibrational wavepacket, as a result of the coherent superposition of the stationary states of the molecular target. The superposition of stationary state wave functions, with phase differences appropriately chosen, can produce a localised wavepacket in the phase space. Usually, the wavepacket has a well defined position and group velocity, and its propagation can be interpreted in terms of the motion of a classical particle, within atomic scale resolution. While the width of the wave-packet, typically of about $\sim$0.1 a.u., is at least one order of magnitude smaller than the accessible space ($\sim$1 a.u. or greater) the description in terms of classical concepts of position and momentum is completely justified.

Since the femtosecond spectroscopy has consolidated itself as a fundamental tool to study the processes at molecular and atomic scales, the systems composed by rare gas atoms, either pure or in presence of impurities, has been widely used to describe and to understand the basic principles behind the photo-induced configurational rearrangements in many-body systems [82, 84–86].

The next section is devoted to the presentation of the phenomenology of pump-probe experiments performed in *Ne* matrices doped with *NO* molecules. These experiments have allowed to study the dynamical evolution of the cavity created around the impurity.

4.2 Pump-probe spectroscopy of *NO* embedded in a *Ne* solid: cavity relaxation

In these experiments, samples are grown first with a relative concentration of *NO* in *Ne* of 1:10 000. This proportion guarantees the low concentration of impurities in the solid. The measurements are performed at a temperature of 3.5 K, thus reducing the density of states accessible to the guest molecules trapped therein. Figure 4.3 presents a scheme of the pump-probe technique applied to this particular system.

In this design, a first pump laser pulse with central wavelength of 192 nm and a temporal width of 280 fs, excites the $A(\nu = 0)$ level of the *NO* molecule at $t' = 0$ (ν refers to the quantum number identifying the vibrational level of the diatomic molecule). A second infrared laser pulse (probe pulse), delayed in time with respect to the pump pulse by an interval T, and with central wavelength varying from 1.1 to 1.4 μm, is used to monitor the dynamical response of the system. The latter induces transitions between the A-electronic state to the Rydberg C and D-electronic states of *NO*. As C and D are practically parallel and very close states, it is difficult to

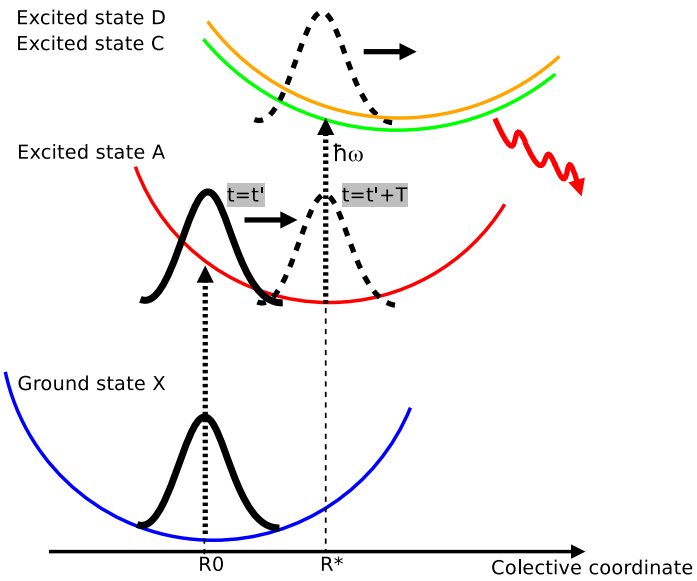

Figure 4.3: Pump-probe experiment scheme of the system composed by an NO embedded in a Ne matrix.

discriminate which of the spectroscopic measurements corresponds to each state. As a consequence, the measured signal contains the contributions of both states. In the experiment, the depletion of A-state population is chosen as the actual pump-probe signal. This is possible because the fraction of population transferred from C and D states to the A state is negligible. The A-state fluoresces to the ground state in around 200 ns, and the signal measured is proportional to the part of the wave-packet transferred from A to C and D states. This signal is recorded as a function of the delay interval T between pump and probe pulses and is termed as "transient absorption spectra".

Each probe pulse wavelength is resonant with a specific energy difference between A and C (or A and D) states for certain configurations of the system denoted by $\mathbf{R}^*$, that is, each probe pulse wavelength determines one (or more) specific configuration of the system. If it is possible to identify $\mathbf{R}^*$ with some collective coordinate with a direct physical meaning, then the dynamical evolution of this coordinate could be

directly measured and, thus, the energy dissipation mechanism into the solid could be inferred. As a result of the experiments performed with *NO* molecules embedded in rare gas matrices, this collective coordinate has been identified with the radius of the nearest neighbour atoms of the first shell around the impurity. Hence, the time-evolution of the cavity formed by this shell around the *NO* can be directly measured.

Table 4.1: Absorption (emission) bands maxima corresponding to transitions from (to) the ground X to (from) the first Rydberg state, $A^2\Sigma^+$ ($\nu = 0$), of *NO* embedded in different matrices of rare gases and para-hydrogen [9]. Values of the Stokes shifts are also presented.

	Absorption	Emission		
	Band maximum [eV]	Width [eV]	Energy [eV]	Stokes shift [eV]
Gas	5.48			
Ne	6.46	0.18	5.65	0.81
Ar	6.36	0.12	5.76	0.60
Xe	5.88	0.08	5.56	0.32
H_2	6.06	0.24	5.47	0.59

Figures 4.4 and 4.5 depict the experimental steady state absorption and emission lineshapes of NO, for the different Rydberg states. Table 4.1 summarizes the values of the respective band centres and widths for the absorption $A \leftarrow X$ and emission $X \leftarrow A$ processes of different rare gas matrices and p-H_2. The corresponding bands can be observed in Figure 4.4 [116].

At first sight, it can be noticed that the absorption bands are shifted to the blue (more energetic) compared with its gas-phase value. These is coherent with the analysis made before related with the dimensions of the *NO* Rydberg electron orbital and the strong electrostatic repulsion it exerts on the atoms of the first nearest neighbours shell. The second relevant aspect, is that the spectral position of the emission band, which is also blue-shifted with respect to the gas-phase value (vertical dotted line) in both argon and neon, points to a non complete relaxation of the

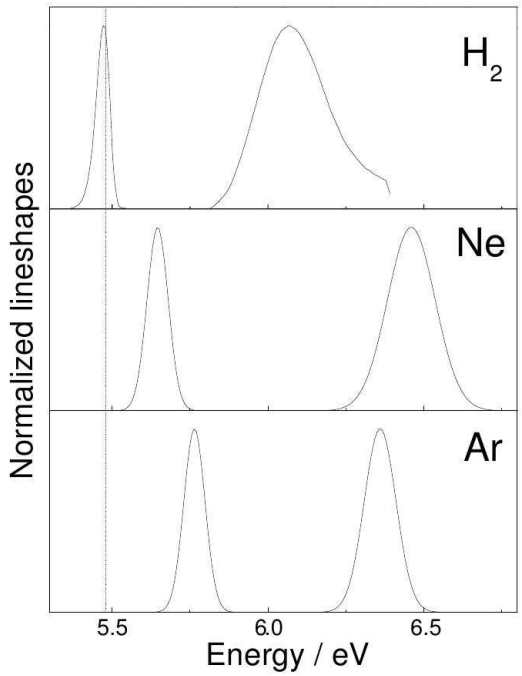

Figure 4.4: Absorption and emission bands $A \leftarrow X$ and $X \leftarrow A$ for matrices of neon, argon and para-hydrogen doped with *NO*. The vertical line indicates the transition energy between both states corresponding to the gas phase of *NO* [116].

lattice: the dopant molecule is still constrained by the cage when it fluoresces, as the surrounding crystal resists to any further compression. For hydrogen, the situation is the opposite: the emission band is slightly shifted to the red of the gas-phase line, indicating a completely lose cage around the impurity. In the latter case the cavity around the impurity is so large at the new equilibrium configuration, that the interaction between the impurity and the surrounding media is almost negligible. This implies that the para-H_2 crystal is less rigid compared with Ar and Ne solids. The Ne matrix presents the more pronounced Stokes shift, indicating that the largest rearrangement induced by the photo-excitation of the impurity takes place for this particular system.

Figure 4.5 shows the absorption bands of *NO* in Ne matrices from A to C and D states measured with respect to the A-state gas-phase spectral value [3, 9]. It can

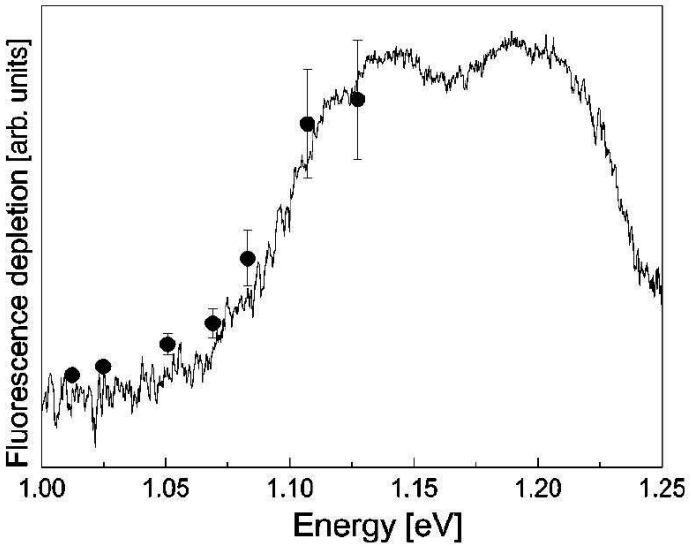

Figure 4.5: Absorption bands $C \leftarrow A$ y $D \leftarrow A$ for neon matrices doped with NO [3].

be noticed that, as stated above, the contributions of C and D states are very close to each other and have almost the same weight. These are the two states utilized to monitor the system dynamics in real time.

Figure 4.6 depicts the transient absorption and emission spectra for certain probe pulse wavelengths, measured in the pump-probe experiments performed for the NO in Ne system [5].

These signals represents the depletion of $A(3s\sigma)$ state, for a pump pulse wavelength of 192 nm. The vertical line indicates the departure time of the dynamics. For larger probe pulse wavelength (between 1325 and 1230 nm), the contribution of only one of the two states (C or D) exists. This feature can be inferred from the picture, where only one peak is present, with a time-width of $\approx$330 fs. The time associated with the peak corresponding to λ=1325 nm indicates the departure time, due to the correspondence between the energy hc/λ and the difference between the A and C PESs for the equilibrium configuration of the ground state. In this way, the instant $t = 0$ is assigned to the position of this peak maximum, because it re-

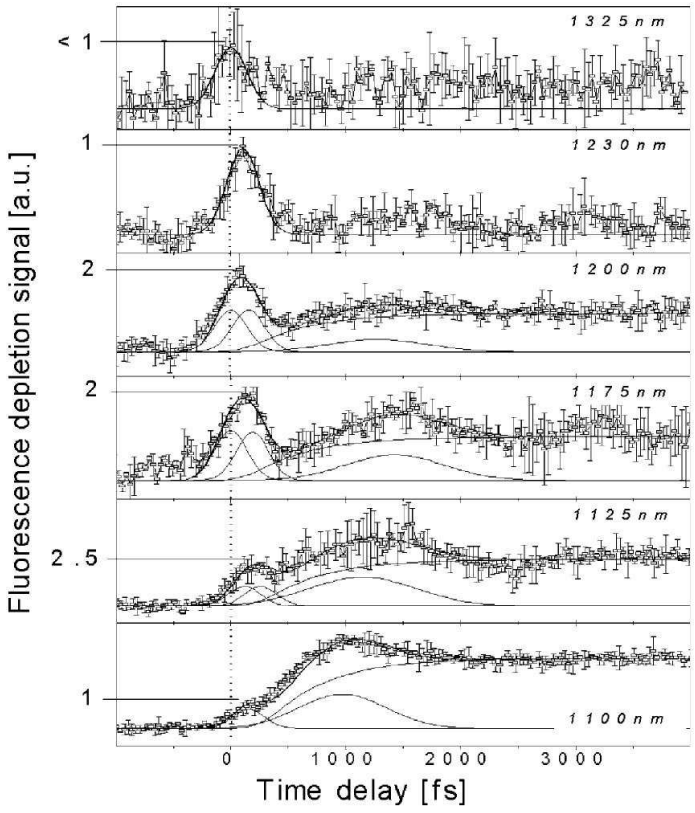

Figure 4.6: Transient absorption spectra for the pump-probe experiments of *NO* in *Ne* matrices [5].

flects the time corresponding to the creation of the wavepacket in the A-state by the pump pulse and, thus, the beginning of the dynamics. For probe pulse wavelengths of $\leqslant$1200 nm, the peak width increases to $\approx$440 fs and the intensity doubles. This fact reveals that for these wavelengths the signal has two contributions corresponding to transitions towards C and D states. The main conclusions that can be extracted from this experiment are:

1. during the first $\sim$200 fs after the photo-excitation, the dimensions of the bubble increases by 0.8 a.u..

2. The first contraction of the bubble occurs at around 1 ps.

3. The system relaxes almost completely in the first 2-3 ps, during which 0.54 eV of energy are released into the solid.

This relaxation time suggests an ultrafast release of the energy into the solid, with a shock wave-like propagation of the perturbation [3].

With the aim of explaining the microscopic mechanisms governing this dynamical process, leading to these experimental results, the theoretical modelling of the dynamical response around the impurity is crucial. The theoretical treatment of this particular system is difficult by nature because of the large number of degrees of freedom involved and the additional complexity of presenting a pronounced quantum behaviour. It is also important to notice, that due to the latter feature, classical methods like MD simulations will not provide a correct description of the underlying dynamical properties. This stresses the importance of developing a fully quantum model for this system, that will make the theoretical interpretation of the experimental findings feasible [4].

Chapter 5

Methodology

In this chapter, the methodology utilized to simulate the time evolution of the solid neon response upon the photoexcitation of an *NO* impurity is exposed. Especial emphasis is made on the features of the dynamical quantum treatment of this system, making use of the Multi-Configurational Time Dependent Hartree Method (MCTDH). To this purpose, a shell model is constructed, taking into account the weak anisotropy of the PES of $NO(A)$ state, thus enabling to considerably reduce the dimensionality of the system.

5.1 The shell model

The *NO* molecule has a small equilibrium radius with a value that does not change appreciably for all its Rydberg states (section 3.1). Furthermore, when embedded in an f.c.c. *Ne* solid, it occupies a substitutional site in the matrix [3, 52]. Additionally, the A state of *NO* presents a weak anisotropy, thus exhibiting an almost spherical symmetry. Based on these arguments, it will be assumed that the *NO* is a rigid molecule whose centre of mass remains fixed at the origin of coordinates. The *Ne*

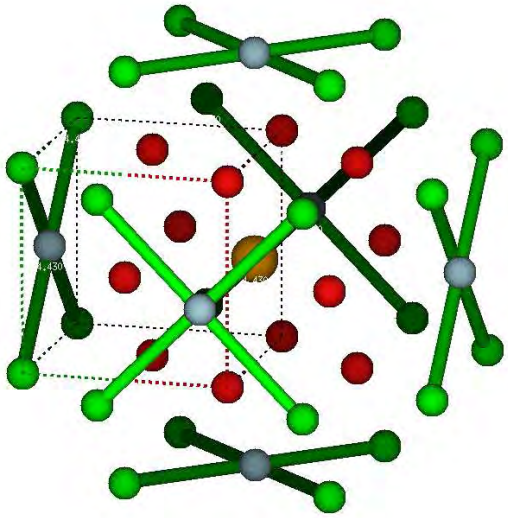

Figure 5.1: Shell model: the *NO* is fixed at the origin of coordinates. The shells are formed by atoms located at the same distance from the origin in the pure f.c.c. lattice. Only radial motions are allowed. The 1^{st} shell contains 12 atoms (red balls) placed at the smallest distance from origin. The 2^{nd} is formed by the next 6 atoms (blue balls) and the 3^{rd}, by the following 24 green atoms. The 4^{th} shell is not represented but it is the next shell belonging to the same crystallographic axis (110) as 1^{st}, therefore containing also 12 atoms.

atoms surrounding the impurity will be grouped in *shells* attending to its radius from the origin of coordinates, i.e., the atoms having the same radius in the f.c.c. pure solid will lie on the same shell. Each shell will be denoted by the index s and its radius by R_s. However, for reasons that will become clear later on, some of the shells will contain a part of the atoms having the same radius. In this way, the motion of the atoms initially located at the same distance from the origin could be described for more than one shell. In Figure 5.1 a scheme of the shell model and the three first *Ne* shells around the impurity is represented.

The atoms placed at the smallest distance from the *NO* molecule form the 1^{st} shell and determine the crystallographic axis (110). The motion of these atoms is expected to be particularly relevant, due to its privileged position with respect to the

impurity. This is the reason why it is necessary to split it up into two subshells: one containing the atoms pertaining to this crystallographic axis and the other grouping the atoms that do not belong to it. For example, as increasing the index s, the first shell presenting this feature is the 9^{th} shell. The atoms of this shell are separated into two subgroups denoted by $9a$ (atoms placed outside the (110) crystallographic axis) and $9b$ (atoms lying along the (110) crystallographic axis). This behaviour repeats itself for other shells located along this axis. In order to facilitate the notation these shells will be grouped in a set defined by $S_p = \{1, 4, 9b, 15, 24b, 34b, 46b, 58\}$. The real cluster simulated in this work contains a total amount of 80 shells in which the 58^{th} shell is the last one belonging to this axis. The subspace S_p will be used in further analysis.

Since three body contributions are negligible in rare gas matrices (they become appreciable only at very high pressures), only pairwise interactions between its constituents will be considered. The total Hamiltonian of the system corresponding to all *Ne* atoms around the impurity, in Cartesian coordinates, taking into account the grouping made before, is:

$$H_\alpha = \sum_{s=1}^{N} \sum_{i_s=1}^{n_s} \left(-\frac{\hbar^2}{2m} \vec{\nabla}^2_{r_{i_s}} + V^d_\alpha(|\mathbf{r}_{i_s}|) + \sum_{j_s=1}^{i_s-1} V(|\mathbf{r}_{i_s} - \mathbf{r}_{j_s}|) + \sum_{s'=1}^{s-1} \sum_{j_{s'}=1}^{n_{s'}} V(|\mathbf{r}_{i_s} - \mathbf{r}_{j_{s'}}|) \right). \quad (5.1)$$

The *NO-Ne* interaction has been designated by V^d_α, where the index $\alpha = X, A, C, D$ denotes the different electronic states considered in this work. A Lennard-Jones potential was used to describe the impurity-rare gas interaction for the ground state ($\alpha = X$) [117], while repulsive exponentials were utilized for the different excited states. The specific values of the potential parameters employed are summarized in Table 5.1.

In equation (5.1), n_s represents the number of atoms belonging to shell s, and N

Table 5.1: Lennard-Jones $V_{LJ} = 4\epsilon\left((\sigma/r)^{12} - (\sigma/r)^{6}\right)$ [79, 117] and exponential $V_{Exp} = A\ exp(-\beta(r - r_0))$ parameters used in this work. The latter were obtained by fitting the experimental absorption and emission spectra (see text).

	A (eV)	β (a.u.$^{-1}$)	r_0(a.u.)	ϵ (meV)	σ (a.u.)
V_X^d	–	–	–	6.258	5.877
V_A^d	3.483	1.580	3.764	–	–
V_C^d	3.918	1.777	3.764	–	–
V_D^d	4.490	1.824	3.764	–	–
V	–	–	–	3.074	5.257

is the total number of shells, that should be large enough to minimize frontier effects and to guarantee the convergence of the observables calculated in the simulation to its corresponding values for an infinite solid. The first term inside the parenthesis in equation (5.1) represents the kinetic energy of atom i_s of shell s; the second term, V_α^d, describes the interaction between the latter and the NO; the third one indicates the interaction between the same atom and the remaining atoms pertaining to the same shell s; and the fourth and last term corresponds to the interaction between such atom and all atoms in another shell $s' \neq s$. Figure 5.2 shows a scheme of the shell model illustrating the relative distances in the pure f.c.c. matrix.

Although until now only a special procedure for performing the sum over all surrounding Ne atoms has been introduced, the reduction of dimensionality is obtained once all atoms in the same shell s are constrained to move radially. In this thesis, the radial motion of $N = 80$ shells, corresponding to a total amount of 4192 atoms, will be considered. As an outcome of the simulations carried out in this work, it is found that this number of atoms guarantees the absence of frontier effects for a time interval of 2 ps, due to the fact that after this time the perturbation has not yet arrived to the boundary of the cluster.

The Cartesian positions of all atoms belonging to shell s can then be parametrized

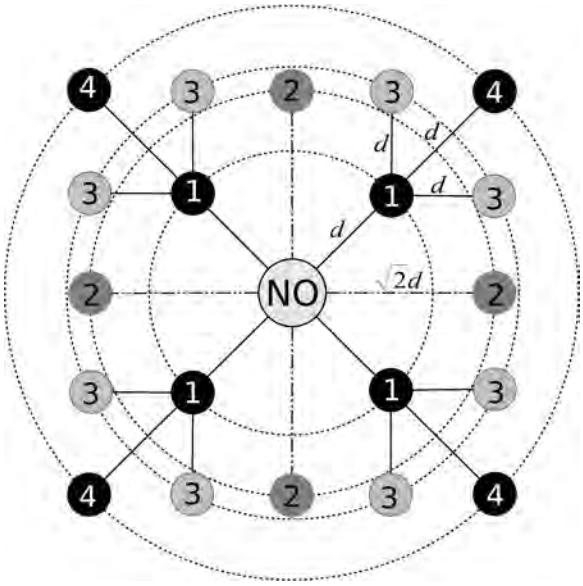

Figure 5.2: Schematic representation of the shell structure for an f.c.c. solid with the *NO* placed in a substitutional site (d is the nearest neighbour distance in the lattice). Notice that not all the atoms included in the representation belong to the same plane in a real f.c.c. crystal.

by its radial distance R_s as follows:

$$\mathbf{r}_{i_s} \equiv \mathbf{r}_{i_s}(R_s) \quad , \quad \text{donde} \quad R_s = |\mathbf{r}_{i_s}| \quad . \tag{5.2}$$

Using this parametrization, the Hamiltonian (5.1) can be transformed to the reduced form:

$$H_\alpha = \sum_{s=1}^{N} -\frac{\hbar^2}{2M_s}\frac{\partial^2}{\partial R_s^2} + W_\alpha(\mathbf{R}) \tag{5.3}$$

where $\mathbf{R} = (R_1, \cdots R_N)$ is the N-dimensional vector whose components are the radii of all shells and $M_s = n_s m$ is the total mass of the atoms in shell s. The potential W_α is a function of the radii R_s and can be written as the superposition of "one" and

"two-body" contributions:

$$W_\alpha(\mathbf{R}) = \sum_{s=1}^{N} W_\alpha^d(R_s) + \sum_{s=1}^{N}\sum_{s'=1}^{s-1} W(R_s, R_{s'}) \tag{5.4}$$

where

$$W_\alpha^d(R_s) = n_s V_\alpha^d(R_s) + V_s(R_s) \tag{5.5}$$

$$W(R_s, R_{s'}) = \sum_{i_s=1}^{n_s}\sum_{j_{s'}=1}^{n_{s'}} V(|\mathbf{r}_{i_s}(R_s) - \mathbf{r}_{j_{s'}}(R_{s'})|) \quad . \tag{5.6}$$

The term corresponding to "one-body" contributions, $W_\alpha^d(R_s)$, contains the *NO-Ne* interaction, $V_\alpha^d(R_s)$, that depends only on the dynamical variables R_s due to its isotropic character, and the contribution named as *intrashell interaction*, given by all *Ne* atoms of the same shell,

$$V_s(R_s) = \sum_{i_s=1}^{n_s}\sum_{j_s=1}^{i_s-1} V(|\mathbf{r}_{i_s}(R_s) - \mathbf{r}_{j_s}(R_s)|) \quad . \tag{5.7}$$

Based on the functional form of the *Ne-Ne* LJ potential, the interaction $V_s(R_s)$ can be rewritten to acquire the form of a single LJ potential.

$$V_s(R_s) = 4\epsilon_s[(\sigma_s/R_s)^{12} - (\sigma_s/R_s)^6] \quad , \tag{5.8}$$

with effective parameters ϵ_s y σ_s (see Appendix A.1). The "two-body" term, $W(R_s, R_{s'})$, is the sum of the interaction between all atoms in shell s with all the atoms belonging to a different shell s'. This interaction has been denoted by *intershell interaction*.

For reasons that will become clear latter, the term $W(R_s, R_{s'})$ needs to be rewritten as a sum of products of "single-particle" functions depending on only one variable, R_s. To this aim, the LJ potential has been replaced by its decomposition as a sum of

n_G Gaussian functions, as proposed in [21]. Introducing such representation for both the *Ne-Ne* potential, $V(\mathbf{r})$, and the $V_s(R_s)$ interaction:

$$V_s(R_s) = \sum_{p=1}^{n_G} G_s(p)\, e^{-\Gamma_s(p)R_s^2} \quad , \tag{5.9}$$

$$V(\mathbf{r}) = \sum_{p=1}^{n_G} a_p\, e^{-\beta_p r^2} \quad , \tag{5.10}$$

the sum over all atoms is performed (see Appendix A.2), leading to the following expressions for the $W_\alpha^d(R_s)$ and $W(R_s, R_{s'})$ potential energies [11]:

$$W_\alpha^d(R_s) = n_s V_\alpha^d(R_s) + \sum_{p=1}^{n_G} G_s(p)\, e^{-\Gamma_s(p)R_s^2} \tag{5.11}$$

$$W(R_s, R_{s'}) = \sum_{p=1}^{n_G} \sum_{J,K=0}^{\infty} F_{s,s'}^{J,K}(p) U_J(R_s) U_K(R_{s'}) \quad . \tag{5.12}$$

where $U_J(R_s) = \left((R_s - R_s^0)^J\, e^{-\beta_p (R_s - R_s^0)^2}\right)$, and similarly for $U_K(R_{s'})$. The coefficients $G_s(p)$ and $F_{s,s'}^{J,K}(p)$ are given explicitly in Appendix A.2. The term $W(R_s, R_{s'})$ can be visualized as the expansion around some reference radii, R_s^0. In order to keep the number of terms that contribute to the sum in equation (5.12) small, one has to choose these values within the regions of the **R**-space where the dynamics takes place. In practice, the distances R_s^0 are chosen to be the equilibrium values of the classical radii corresponding to the excited state of the impurity. Then, the summation can be truncated at fairly low orders. In the results presented in this work, we kept all terms up to $J + K = 10$, this choice was found to yield converged results.

The Hamiltonian written in this form contains around 11400 terms corresponding to the 80-dimensional potential energy surface. It is important to remark, that both the number of terms in the Hamiltonian and the amount of degrees of freedom, makes the numerical solution of the time-dependent Schrödinger equation for this system,

to be at the edge of the current computational possibilities. This Hamiltonian is the starting point of the dynamical calculations presented in this work.

5.2 Quantum dynamics

The Hamiltonian in (5.3), written in terms of the multidimensional potential developed in equations (5.12), is used for the quantum treatment of the shell dynamics by solving the multidimensional time-dependent Schrödinger equation for the electronic ground ($\alpha = X$) and excited ($\alpha = A$) states. The multidimensional wave function is expressed by:

$$\Psi_\alpha(\mathbf{R}, t) \;=\; \prod_{s=1}^{N} \varphi_\alpha^{(s)}(R_s, t) \quad . \tag{5.13}$$

In the special parametrization of the high-dimensional potential energy surface describe above (equation (5.12)), the dependence with the dynamical variables inside each term of the sum is factorized. This feature allows to make use of the Heidelberg MCTDH (Multi-Configurational Time Dependent Hartree) package [16, 118] for the numerical propagation of the wave function using both real and imaginary times. Specifically, the ground state Hamiltonian ($\alpha = X$) is employed to find the initial state of the system using the relaxation method [119], while the excited state Hamiltonian is utilized to calculate the dynamical response of the matrix after the photoexcitation.

In this work, first, the time-dependent Hartree approximation has been used to solve the coupled Schrödinger equation for the X and A states, including explicitly the shape of the pump pulse. Such study enables the investigation the influence of the pulse duration on the system dynamics, specially on the shape of the transient

absorption spectra. As a second step, the consequences of employing the Hartree approximation as well as the importance of the dynamical correlations between the relevant degrees of freedom, are evaluated by comparing the results obtained using a multi-configurational wave function and a single Hartree product (within the impulsive approximation). The latter relies on the assumption, that the initial excitation pulse triggering the dynamics in the A-state is instantaneous, that is, at $t = 0$ the relaxed wave-function of the ground state is placed on the PES of the A-state [120, 121]. As a consequence, the Schrödinger equation is decoupled and it can be solved separately for A-state only. The inclusion of many configurations in the wave function representation increases the computational effort, associated to the solution of the multidimensional Schrödinger equation, so fast, that the cost of the simultaneous propagation of the quantum state on the two coupled surfaces quickly becomes prohibitive. Hence, the use of the impulsive limit is mandatory.

When the coupling between both electronic states is present, the Schrödinger equation to be solved is:

$$i\hbar\partial_t \begin{pmatrix} \Psi_X(\mathbf{R},t) \\ \Psi_A(\mathbf{R},t) \end{pmatrix} = \begin{pmatrix} H_X & -\mu E(t) \\ -\mu E(t) & H_A \end{pmatrix} \begin{pmatrix} \Psi_X(\mathbf{R},t) \\ \Psi_A(\mathbf{R},t) \end{pmatrix} \tag{5.14}$$

where the dipole moment function, μ, corresponding to the initial and final states transition is taken as a constant. $E(t)$ is the electromagnetic pulse amplitude that couples both states. This coupled multidimensional Schrödinger equation describe the rearrangement dynamics of the Ne matrix upon the photo-excitation of the NO.

Within the MCTDH method [16, 17, 76, 77] the multidimensional wave-function is

expressed through the expansion:

$$|\Psi(t)\rangle \quad = \quad \sum_{j_1=1}^{n_1} ... \sum_{j_f=1}^{n_f} A_{j_1,...,j_f}(t) \prod_{\kappa=1}^{f} |\varphi_{j_\kappa}^{(\kappa)}(t)\rangle \tag{5.15}$$

where $|\Psi(t)\rangle \equiv \Psi_\alpha(\mathbf{R},t)$, $|\varphi_{j_\kappa}^{(\kappa)}(t)\rangle \equiv \varphi_{j_\kappa}(R_\kappa,t)$ is the single-particle wave function corresponding to the degree of freedom κ. j_κ is the configuration index and f is the total amount of degrees of freedom of the system. $A_{j_1,...,j_f}(t)$ are the expansion coefficients. Each term in the sum (5.15) is a single Hartree product. The single-particle functions (SPF) $|\varphi_{j_\kappa}^{(\kappa)}(t)\rangle$ could depend on one or more degrees of freedom, in the latter case the corresponding variables are called combined modes. The factorization in (5.15) allows to avoid the exponential increasing of the computational cost required to integrate numerically the Schrödinger equation, with respect to the dimension of the Hilbert space in which the wave-function is defined [122]. The n_i $(i = 1, \dots f)$ are the number of SPF employed for each degree of freedom, κ. The equations of motion for the coefficients $A_{j_1,...,j_f}(t)$ and the functions $|\varphi_{j_\kappa}^{(\kappa)}(t)\rangle$ can be obtained by applying the Dirac-Frenkel variational principle [17].

The representation (5.15) of the many-body wave function is a generalization of the well known Time-Dependent Hartree approximation (TDH): when choosing all $n_i = 1$, the wave function reduces to a Hartree product.

On a single potential energy surface, the Schrödinger equation to solve is:

$$i\hbar\partial_t|\Psi(t)\rangle = H_\alpha|\Psi(t)\rangle \quad , \alpha = X, A \quad . \tag{5.16}$$

One of the interesting features of the MCTDH method, as implemented in the Heidelberg package, is the possibility to use different numbers of SPF, n_i, for each degree of freedom. Whenever exists highly correlated degrees of freedom it is even

more convenient to combine them in a single function that contains this subset of coordinates ("mode combination"). Both methods are employed in this work in order to evaluate the dynamical correlations.

On the other hand, for the numerical propagation, each of the time-dependent SPF is expanded in a complete basis set of time-independent functions (*primitive basis*). The primitive basis used in this thesis was the discrete variable representation of the harmonic oscillator [16]. The equations of motion for the single-particle wave-functions and the expansion coefficients of the MCTDH method, emerging from the Dirac-Frenkel variational principle, are solved employing the Variable Mean Field (VMF) integration scheme [16] with adjustable time step. The initial time step is chosen to be 10^{-7} fs.

5.2.1 The Multi-Configurational Time-Dependent Hartree method

In spite of the great development of modern computers, finding the solution of the time-dependent (or the time-independent) Schrödinger equation for more than 4 degrees of freedom is an extreme difficult task. Indeed, the number of basis functions needed to represent the wave-function and, thus, the numerical effort, increases exponentially with the number of degrees of freedom. In the field of quantum chemistry, there are several softwares devoted to solve the Schrödinger equation for systems with a large number of degrees of freedom. Nevertheless, they are devoted to investigate the electronic structure of the systems, therefore considering only one type of interaction: the Coulombic potential. On the other hand, the resolution of quantum dynamical problems in molecular physics poses greater challenges because, for example, there is not only one family of coordinates that properly describes all the problems in this

field. Besides, the operators can act over all the coordinates at the same time, while in quantum chemistry problems the Coulomb potential only acts over the electron coordinates. Another difficulty is, that even at low energies, the nuclear wave-function is characterized by relatively large quantum numbers and therefore by fast and pronounced spatial oscillations, very hard to describe numerically. These are the essential reasons why it is a complicated task to develop a general methodology to solve the nuclear Schrödinger equation, even for relatively few degrees of freedom.

In the time-dependent picture, further approximations have been developed which keep a fully quantum mechanical picture while removing the exponential scaling problem. These methods are exemplified by the TDH method (also known as time-dependent self-consistent field (TDSCF)). Here, the wavefunction is represented as a Hartree product of one-dimensional functions, resulting in a set of coupled one-dimensional equations of motion for the wave-packet. In the following, the MCTDH method will be described.

In order to gain in clarity, the method will be discussed first for only two dimensions and it will be generalized afterwards. In the two dimensional case, the wave-function is written as:

$$\Psi(x, y, t) = a(t)\varphi_1(x, t)\varphi_2(y, t) \quad , \tag{5.17}$$

where a is a complex number depending on time. φ_1 and φ_2 are the SPF or *orbitals* for each degree of freedom x and y, respectively. The product $\varphi_1\varphi_2$ is named a *Hartree product*. Equation (5.17) does not determine the single-particle functions uniquely, since phases and normalization factors may be shifted from φ_1 to φ_2 or even to a. The introduction of the redundant term $a(t)$ allows to freely choose the φ_1 and φ_2

phases. By imposing the following constrains:

$$\langle\varphi_1|\dot{\varphi}_1\rangle = \langle\varphi_2|\dot{\varphi}_2\rangle = 0 \quad , \tag{5.18}$$

one guarantees that the norms of both φ_1 and φ_2 do not change and the phases remain fixed. If norms are initially set to $\|\varphi_1\| = \|\varphi_2\| = 1$, the SPFs will remain normalized during the whole propagation. The equations of motion for $a(t)$, φ_1 and φ_2 are derived from the Dirac-Frenkel variational principle [123, 124]:

$$\langle\delta\Psi|H - i\hbar\partial_t|\Psi\rangle = 0 \quad . \tag{5.19}$$

Variation with respect to $a(t)$ leads to:

$$\langle\varphi_1\varphi_2|i\hbar\dot{a}\varphi_1\varphi_2 + i\hbar a\dot{\varphi}_1\varphi_2 + i\hbar a\varphi_1\dot{\varphi}_2 - Ha\varphi_1\varphi_2\rangle = 0 \quad , \tag{5.20}$$

or, using (5.18) and normalizing φ_1 and φ_2 initially to 1,

$$i\hbar\dot{a} = \langle H\rangle a \quad , \tag{5.21}$$

where $\langle H\rangle = \langle\varphi_1\varphi_2|H|\varphi_1\varphi_2\rangle$. Variations with respect to both φ_1 and φ_2 yield:

$$i\hbar\dot{\varphi}_1 = (H^{(1)} - \langle H\rangle)\varphi_1 \quad , \text{ and } \quad i\hbar\dot{\varphi}_2 = (H^{(2)} - \langle H\rangle)\varphi_2 \quad . \tag{5.22}$$

The *mean-field operators* are defined by

$$H^{(1)} = \langle\varphi_2|H|\varphi_2\rangle \quad , \text{ and } \quad H^{(2)} = \langle\varphi_1|H|\varphi_1\rangle \quad . \tag{5.23}$$

Equations (5.22) can be rewritten as:

$$i\hbar\dot{\varphi}_1 = (1 - |\varphi_1\rangle\langle\varphi_1|)H^{(1)}\varphi_1 \quad , \text{ and } \quad i\hbar\dot{\varphi}_2 = (1 - |\varphi_2\rangle\langle\varphi_2|)H^{(2)}\varphi_2 \quad , \tag{5.24}$$

where $|\varphi_1\rangle\langle\varphi_1|$ and $|\varphi_2\rangle\langle\varphi_2|$ are the projectors along the states φ_1 and φ_2 respectively.

The TDH wave-function can be considered as being propagated by an effective Hamiltonian H_{ef}:

$$i\hbar\dot{\Psi} = H_{\text{ef}}\Psi \quad , \text{ with } \quad H_{\text{ef}} = H^{(1)} + H^{(2)} - \langle H\rangle \tag{5.25}$$

To evaluate the error introduced by the TDH approximation, let us consider the following model Hamiltonian:

$$H = -\frac{\hbar^2}{2m_1}\frac{\partial^2}{\partial x^2} - \frac{\hbar^2}{2m_2}\frac{\partial^2}{\partial y^2} + V_1(x) + V_2(y) + W_1(x)W_2(y) \quad . \tag{5.26}$$

In this case,

$$H_{\text{ef}} = H - (W_1 - \langle W_1\rangle)(W_2 - \langle W_2\rangle) \quad , \tag{5.27}$$

that is,

$$i\hbar\dot{\Psi} - H\Psi = -(W_1 - \langle W_1\rangle)(W_2 - \langle W_2\rangle)\Psi \quad . \tag{5.28}$$

The right hand side of this equation describes the error introduced within the TDH approximation. This error disappear if the Hamiltonian is separable, and it becomes small if the functions W_1 and W_2 are almost constant along the width of the single-particle functions φ_1 and φ_2, respectively. This explains why the error introduced by the TDH approximation (equation (5.28)) is much smaller or vanishes compared

with the time-independent Hartree approximation: in general the time-dependent wave-packet is likely localized, while the eigenstates are usually very delocalised. The TDH approach has been widely used in the study of many dynamical processes in molecular physics [125–128].

Quantum systems are usually characterized by an important correlation between the different degrees of freedom. That is why a single Hartree product is not enough too describe its dynamical behaviour. The first multi-configurational time-dependent approach was introduced by Makri and Miller [129]. Afterwards, Kosloff *et al.* show that the reactive scattering of $H + H_2$ in two dimensions can not occur if a single Hartree product is used to represent the time-dependent wave-function describing the process [130]. Finally, Meyer, Manthe and Cederbaum present the general formulation of the MCTDH method. They show that the choice of the Hartree functions is not unique, and that the equations can be fairly simplified if the orthonormalization constraint is assumed to hold for all times. The professional package was developed by Hans-Dieter Meyer from Heidelberg (http://www.pci.uni-heidelberg.de/tc/usr/mctdh/) [16].

As mentioned above, the MCTDH wave-function is a generalization of the TDH one (equation 5.15). For the system under study, the total amount of degrees of freedom is $f = 80$. The coordinates $R_1, \ldots, R_f$ are, in this case, the shell radii. $A_{j_1 \ldots j_f}$ are the expansion coefficients in the basis set of the SPFs $\varphi_{j_\kappa}^{(\kappa)}$. Each of this functions is expanded in a time-independent *primitive basis* set:

$$\varphi_{j_\kappa}^{(\kappa)}(R_\kappa, t) = \sum_{i_\kappa}^{N_\kappa} G_{i_\kappa}^{j_\kappa}(t) \chi_{i_\kappa}^{(\kappa)}(R_\kappa) \quad . \tag{5.29}$$

where N_κ is the number of primitive basis used for the degree of freedom κ. Setting $n_1 = \ldots = n_f = 1$ one recovers the TDH wave function. The TDH approximation is

thus contained in MCTDH method as a limiting case. As the number of configurations n_κ is increased, the precision of the proposed representation of the wave packet gets larger and the MCTDH wave function converges to the exact one when n_κ tends to N_κ. However, the computational cost of the numerical propagation grows very fast as the number of configurations is enlarged, that is, with the increase of n_κ.

As in the TDH case, the MCTDH wave-function representation is not unique. Uniquely defined propagation is obtained by imposing the constraints to the SPFs:

$$\langle \varphi_j^{(\kappa)}(0)|\varphi_l^{(\kappa)}(0)\rangle = \delta_{jl} \quad , \text{ and } \quad \langle \varphi_j^{(\kappa)}(t)|\dot{\varphi}_l^{(\kappa)}(t)\rangle = -i\langle \varphi_j^{(\kappa)}(t)|g^{(\kappa)}|\varphi_l^{(\kappa)}(t)\rangle \quad . \tag{5.30}$$

Here the *constraint operators*, $g^{(\kappa)}$, acting exclusively on the κ degree of freedom, are arbitrary unless for the hermitian condition. From now on, it will be assumed that all $g^{(\kappa)} = 0$. This is in most cases the usual choice. With this choice, the constraints (5.30) guarantee the orthonormality of the SPFs during the whole propagation.

In order to introduce the MCTDH equations, the notation used will be simplified as:

$$A_J = A_{j_1 \ldots j_f} \quad , \text{ and } \quad \Phi_J = \prod_{\kappa=1}^{f} \varphi_{j_\kappa}^{(\kappa)} \quad , \tag{5.31}$$

where the multiple index J describe one configuration, i.e., one single Hartree product given by Φ_J. The introduction of the projector operator associated to the function space of the particle with index κ,

$$P^{(\kappa)} = \sum_{j=1}^{n_\kappa} |\varphi_j^{(\kappa)}\rangle\langle\varphi_j^{(\kappa)}| \quad , \tag{5.32}$$

allows to define the *single-hole functions* $\Psi_l^{(\kappa)}$ as the linear combination of Hartree products of the $(f-1)$ SPFs excluding the one corresponding to the degree of freedom

κ.

$$\begin{aligned}\Psi_l^{(\kappa)} &= \sum_{j_1}\cdots\sum_{j_{\kappa-1}}\sum_{j_{\kappa+1}}\cdots\sum_{j_f} A_{j_1\ldots j_{\kappa-1}lj_{\kappa+1}\ldots j_f}\varphi_{j_1}^{(1)}\cdots\varphi_{j_{\kappa-1}}^{(\kappa-1)}\varphi_{j_{\kappa+1}}^{(\kappa+1)}\cdots\varphi_{j_f}^{(f)} \\ &= \sum_{J}^{\kappa} A_{J_l^\kappa}\varphi_{j_1}^{(1)}\cdots\varphi_{j_{\kappa-1}}^{(\kappa-1)}\varphi_{j_{\kappa+1}}^{(\kappa+1)}\cdots\varphi_{j_f}^{(f)} \quad . \end{aligned} \tag{5.33}$$

The index J_l^κ of equation (5.33) corresponds to the multiple index J with the internal index $j_\kappa = l$ fixed (which corresponds to the SPF $\varphi_{j_\kappa=l}^{(\kappa)}$), and $\sum_J^\kappa$ is the sum over all indexes corresponding to all degrees of freedom excluding κ.

The single-hole functions allows to define the *mean-field operators*,

$$\langle H\rangle_{jl}^{(\kappa)} = \langle\Psi_j^{(\kappa)}|H|\Psi_l^{(\kappa)}\rangle \quad , \tag{5.34}$$

where, as in (5.23), the superscript (κ) indicates the integration over all degrees of freedom excluding κ. Using the single-hole functions one can define the *density matrices*

$$\begin{aligned}\rho_{jl}^{(\kappa)} &= \langle\Psi_j^{(\kappa)}|\Psi_l^{(\kappa)}\rangle \\ &= \sum_{j_1}\cdots\sum_{j_{\kappa-1}}\sum_{j_{\kappa+1}}\cdots\sum_{j_f} A^*_{j_1\ldots j_{\kappa-1}jj_{\kappa+1}\ldots j_f}A_{j_1\ldots j_{\kappa-1}lj_{\kappa+1}\ldots j_f} \\ &= \sum_{J}^{\kappa} A^*_{J_j^\kappa}A_{J_l^\kappa} \quad . \end{aligned} \tag{5.35}$$

Note that $\langle H\rangle_{jl}^{(\kappa)}$ is an operator acting exclusively on the degree of freedom κ, and the trace of $\rho_{jl}^{(\kappa)}$ is always equal to $\|\Psi\|^2$ due to the orthonormality of the SPFs.

Employing the notations introduced above, Ψ, $\dot{\Psi}$ and $\delta\Psi$ can be expressed as:

$$\begin{aligned} \Psi &= \sum_J A_J \Phi_J = \sum_{j=1}^{n_\kappa} \varphi_j^{(\kappa)} \Psi_j^{(\kappa)} \\ \dot{\Psi} &= \sum_{\kappa=1}^{f} \sum_{j=1}^{n_\kappa} \dot{\varphi}_j^{(\kappa)} \Psi_j^{(\kappa)} + \sum_J \dot{A}_J \Phi_J \quad , \\ \frac{\delta\Psi}{\delta A_J} &= \Phi_J \quad , \text{ and } \quad \frac{\delta\Psi}{\delta \varphi_j^{(\kappa)}} = \Psi_j^{(\kappa)} \quad . \end{aligned} \tag{5.36}$$

With the aid of the variational principle (5.19) and the constraints (5.30), the variation of the coefficients yields:

$$\langle \Phi_J | H | \Psi \rangle - i\hbar \langle \Phi_J | \dot{\Psi} \rangle = 0 \quad , \tag{5.37}$$

conducing to the respective coefficient equations:

$$i\hbar \dot{A}_J = \langle \Phi_J | H | \Psi \rangle \quad . \tag{5.38}$$

Now varying with respect to the SPFs:

$$\langle \Psi_j^{(\kappa)} | H | \Psi \rangle = i\hbar \langle \Psi_j^{(\kappa)} | \sum_{\kappa'=1}^{f} \sum_{l=1}^{n_{\kappa'}} \dot{\varphi}_l^{(\kappa')} \Psi_l^{(\kappa')} \rangle + i \sum_J \langle \Psi_j^{(\kappa)} | \Phi_J \rangle \dot{A}_J \quad , \tag{5.39}$$

one can obtain:

$$i\hbar \sum_{l=1}^{n_\kappa} \rho_{jl}^{(\kappa)} \dot{\varphi}_l^{(\kappa)} = \langle \Psi_j^{(\kappa)} | H | \Psi \rangle - \sum_J \langle \Psi_j^{(\kappa)} | \Phi_J \rangle \langle \Phi_J | H | \Psi \rangle \quad . \tag{5.40}$$

Note that

$$\sum_J \langle \Psi_j^{(\kappa)} | \Phi_J \rangle \langle \Phi_J | = P^{(\kappa)} \langle \Psi_j^{(\kappa)} | \quad , \text{ and } \quad \langle \Psi_j^{(\kappa)} | H | \Psi \rangle = \sum_{l=1}^{n_\kappa} \langle H \rangle_{jl}^{(\kappa)} \varphi_l^{(\kappa)} \quad . \tag{5.41}$$

After some algebraic manipulations one finally arrives to the MCTDH equations of motion:

$$i\hbar\dot{A}_J = \sum_L \langle\Phi_J|H|\Phi_L\rangle A_L \quad , \tag{5.42}$$

$$i\hbar\dot{\varphi}^{(\kappa)} = (\mathbf{1}_{n_\kappa} - P^{(\kappa)}) \left[(\rho^{(\kappa)})^{-1}\langle\mathbf{H}\rangle^{(\kappa)}\right] \varphi^{(\kappa)} \quad , \tag{5.43}$$

where a vectorial notation has been used for the SPF corresponding to the degree κ,

$$\varphi^{(\kappa)} = \left(\varphi_1^{(\kappa)}, \ldots, \varphi_{n_\kappa}^{(\kappa)}\right)^T \quad , \tag{5.44}$$

$\rho^{(\kappa)}$ is the density matrix corresponding also to the degree κ, $\langle\mathbf{H}\rangle^{(\kappa)}$ is the mean-field operators matrix, and $\mathbf{1}_{n_\kappa}$ is the unity matrix of dimension $n_\kappa \times n_\kappa$.

To conclude, it is important to remark that the MCTDH equations conserve the norm and, for time-independent Hamiltonians, also the energy. The time-dependence of the basis functions provides a great flexibility to the MCTDH method and the possibility to adapts itself to a wide variety of physical problems. It is necessary to emphasize that the PES has to be written as a superposition of separable terms, in order to achieve an efficient performance of the MCTDH algorithm. The method convergence will depend then on the number of configurations needed to describe the wave function of the system. This subject will be discussed afterwards in section 6.2.1.

5.2.2 Imaginary-time propagation of the wave-function: relaxation method

This method was first proposed by R. Kosloff [119] in 1986, to find the eigenvalues and eigenfunctions of the stationary Schrödinger equation on a grid. The method is

based on solving the Schrödinger equation for the imaginary time $\tau = it$:

$$\frac{\partial \Psi(\mathbf{R},\tau)}{\partial \tau} = \sum_j \frac{\hbar^2}{2m_j} \nabla_j^2 \Psi(\mathbf{R},\tau) - V(\mathbf{R})\ \Psi(\mathbf{R},\tau) \quad . \tag{5.45}$$

In the following, only time-independent Hamiltonians will be considered. The formal solution of the above equation, in the basis formed by the eigenfunctions $\varphi_n(\mathbf{R})$ of $\hat{H}$ operator, is:

$$\Psi(\mathbf{R},\tau) = \sum_n c_n \varphi_n(\vec{R}) e^{-E_n \tau/\hbar} \tag{5.46}$$

The contributions of the eigenstates with energy E_n to the total wave-function decay exponentially (the time τ used in the simulations is a real parameter). The term corresponding to the ground state presents the smaller decay rate, thus, when $\tau \to \infty$, the contributions of all the excited states can be neglected and the total wave function will consist, essentially, in the ground state eigenvector $\Psi_0(\mathbf{R})$. In this way, the ground state can be obtained from the asymptotic wave function $\Psi_0 \propto \Psi(\mathbf{R}, \tau \to \infty)$. The latter is found via the numerical propagation of the state $\Psi(\mathbf{R},\tau)$ as in equation (5.45), renormalizing the wave function after each time step.

This method will be used later, to generate the relaxed wave function of both the basic as well as the excited states for the specific problem addressed in this thesis. In the case in which the impulsive approximation is used, the relaxed ground state wave-function will be the used as the initial condition for the dynamical propagation in the excited state of interest.

5.3 Observables

5.3.1 Absorption and emission spectra

From the knowledge of the initial state $\Psi_X^{in}(\mathbf{R})$, it is possible to calculate the absorption and emission spectra, by propagating the former on the excited potential energy surfaces. Employing the Fourier transform of the autocorrelation function of $\Psi_X(\mathbf{R})$ it is possible to get the absorption spectra corresponding to the transition to the different excited states [120, 121].

Let $\zeta(\mathbf{R})$ be $\zeta(\mathbf{R}) = \mu_{fi}\Psi_X^{in}(\mathbf{R}, t = 0)$, where $\Psi_X^{in}(\mathbf{R}, t = 0)$ is the relaxed nuclear wave function corresponding to the initial electronic state, X, and μ_{fi} is the matrix element of the dipole moment operator calculated with the initial and final states. The absorption spectra can be calculated through the expression:

$$\sigma(\omega) \propto \int_{-\infty}^{+\infty} dt \langle \zeta(\mathbf{R}) | e^{-\frac{i}{\hbar}H_f t} \zeta(\mathbf{R}) \rangle e^{-\frac{i}{\hbar}(E_0+\hbar\omega)t} \quad , \tag{5.47}$$

where H_f is the final state Hamiltonian. In our case these will be the A, C, or D states. E_0 is the ground state energy, i.e., the corresponding eigenvalue of the wave function $\Psi_X^{in}(\mathbf{R}, t = 0)$. $\hbar\omega$ is the energy of the instantaneous laser pulse inducing the transition. To obtain the emission spectra it is necessary to find the relaxed wave functions of the excited states and, afterwards, to Fourier transform the autocorrelation function with the Hamiltonian of the ground state. In this work, the emission band from states A to X is evaluated.

By fitting $\sigma(\omega)$ to the experimental absorption and emission bands it is possible to compute the potential energy surface of one of the two states, if the other is previously known. In this thesis, the PES corresponding to the A, C and D states will be retrieved, employing this method and using the ground state PES as an input.

5.3.2 Reduced densities and other observables

In general, the expectation value of an observable O, is computed in the standard way using the time-dependent wave-function $|\Psi\rangle$:

$$\langle O\rangle = \langle\Psi|\hat{O}|\Psi\rangle \quad , \tag{5.48}$$

where $\hat{O}$ is the operator associated to the physical magnitude O.

In this work, observables such as the mean radius of each shell $\langle R_s\rangle$ with the impurity being in the states X and A, respectively, the variances of the reduced densities associated to each shell $\langle\Delta R_s\rangle$ and its corresponding kinetic energy, have been computed using equation (5.48). Another observable very useful to reveal the quantum effects of the system is the one-dimensional reduced density distribution defined by:

$$\rho_\alpha^{(s)}(R_s,t) \;=\; \int |\Psi_\alpha(\mathbf{R},t)|^2\, d^{N-1}R_s' \tag{5.49}$$

where $d^{N-1}R_s'$ denotes the integration over all degrees of freedom except R_s.

5.3.3 Chain energy

The Hamiltonian of the subspace S_p is defined as:

$$\hat{H}_{\rm C} \;=\; \sum_{s\in S_p}\left(T_s + W^d(R_s) + \frac{1}{2}\sum_{s'\in S_p} W(R_s,R_{s'})\right) \quad . \tag{5.50}$$

This Hamiltonian describes the dynamics along the crystallographic axis (110) defined by the impurity and the its first nearest neighbours (the atoms in the 1^{st} shell). Taking into account that the the potential between these shells (equation (5.12)) has a non

negligible value only for atoms in contiguous shells, this Hamiltonian can be visualized as the one corresponding to a chain of atoms. The energy associated to this chain can be computed by equation (5.48).

5.3.4 Pump-probe signals: transient absorption spectra

The dynamical process of interest occurs while the NO molecule is in its Rydberg A state. The probe laser pulse used in the spectroscopic experiments [5] induces transitions from this state to the C y D states of NO.

Up to first order of time-dependent perturbation theory, the nuclear wave-function corresponding to the final electronic state is given by the expression (see Apendix A.3 for further details):

$$\Psi_\alpha(\mathbf{R},t;T) \sim \mu_{\alpha A}\int_{-\infty}^{t} dt'\, e^{-\frac{i}{\hbar}H_\alpha(t-t')}\; f(t'-T)\, e^{-i\omega(t'-T)} e^{-\frac{i}{\hbar}H_A(t'-T)}\Psi_A(\mathbf{R},T) \quad , \tag{5.51}$$

with $\alpha = C, D$. Here, a constant dipole moment $\mu_{\alpha A}$ is assumed. T is the time delay between pump and probe pulses. In this expression, the term $f(t) = e^{-\left(\frac{t}{\tau}\right)^2}$ is the envelope function of the probe pulse, chosen to be of Gaussian form, with duration τ and central frequency ω.

Assuming the measured signal to be proportional to the population of the final excited state α, after the application of both the pump and the probe pulses, the following expression can be written:

$$P_\alpha(T) \;=\; \lim_{t\to\infty}\int d^N R_s \left|\Psi_\alpha(\mathbf{R},t;T)\right|^2 \quad . \tag{5.52}$$

If the duration of the probe pulse is very short compared with the characteristic scale of the dynamics response of the system, the previous expression can be simplified

to [131–133]:

$$P_\alpha(T) = \int_{-\infty}^{\infty} dt\, e^{-2\left(\frac{t}{\tau}\right)^2} \int dR_1\, e^{-\frac{\tau^2}{2\hbar^2}(D_\alpha(R_1)-\hbar\omega)^2} \rho_A^{(1)}(R_1, T+t) \tag{5.53}$$

$$\tag{5.54}$$

where $D_\alpha(R_1) = W_\alpha^d(R_1) - W_A^d(R_1)$ is the *potential difference* with the impurity in the $\alpha = C, D$ and A states. The NO-host matrix interaction is assumed to be restricted to the first shell of Ne atoms. The dependence on R_1 reproduce the phenomenology of the electronic bubble dynamics inferred from the experiments. In the impulsive limit, the nuclei remain fixed in their instantaneous positions while the transition of the NO to the excited state occurs, leading to the interpretation of D_α as the difference between the NO final and initial interaction potentials with the 1^{st} nearest neighbour shell being at the same position R_1 (taking into account that the interaction between the NO and the 2^{nd} shell is negligible).

Equation (5.53) reflects the fundamental feature of pump-probe spectroscopy: the wavepacket motion is detected through the filter function $e^{-\frac{\tau^2}{2\hbar^2}(D_\alpha(R_1)-\hbar\omega)^2}$ defining certain geometrical configurations R_1^* of the 1^{st} shell, for which the filter function is resonant with the central probe pulse frequency. These special configurations are called *transient Franck-Condon* points. When the wavepacket arrives to these points, transitions to higher excited states are favoured [132–138] and the signal measured, which is proportional to the population of those excited states, increases considerably. Due to the finite duration of the pulse, the signal is distributed along its temporal width. Thus, the potential difference plays the role of an intermediate function which maps the motion of the wavepacket associated to the 1^{st} shell into the pump-probe signal that can be measured in a spectroscopic experiment. The next chapter will be devoted to the discussion of the quantum dynamical response of solid Ne upon

photo-excitation of a *NO* impurity, using the methodology described in the current chapter.

Chapter 6

Results and discussion

In this chapter, the results obtained via the solution of the time-independent and time-dependent Schrödinger equations are presented. Using the multidimensional wave function, the structural properties of the system in the initial and the final electronic states, the absorption and emission bands, the transient absorption spectra, etc., are evaluated and compared to the results of pump-probe experiments carried out in neon matrices doped with NO. The theoretical results are discussed within the proposed model [11, 139].

6.1 Time-dependent Hartree approximation

6.1.1 Structural properties and steady state spectroscopy

In this section, the static properties computed through the simulation of the pure Ne neon solid and in presence of the NO impurity, within the Hartree approximation, are presented. In the calculation of these static properties and the stationary absorption and emission spectra, both the relaxation method and the self-correlation of the vibrational wave function, described in the previous chapter, are employed.

The knowledge of the initial state is one of the prerequisites to perform the simulation of the system dynamics after the photo-excitation by the laser pulse. This is achieved through the propagation of the state vector in imaginary time, using the Hamiltonian of the electronic ground state [119]. The propagation is made employing the MCTDH package of Heidelberg, with the potential energy surface generated according to equation (5.12), choosing $R_s^0 = R_s^e$, i.e, the reference radii are taken equal to the classical equilibrium radii of the *Ne* atoms in the matrix, while the impurity is in the A excited state.

After the propagation, the relaxed multidimensional wave function, $\Psi_X^{in}(\mathbf{R})$, describing the nuclear motion in the electronic ground state, is obtained. In order to asses the structural changes induced by the impurity, the expectation values $\langle R_s \rangle_X$, using this ground state wave function, are calculated and compared with the average radii of each shell in the pure f.c.c. matrix. The latter radii, denoted as $\langle R_s \rangle_p$, are also obtained from the solution of the stationary Schrödinger equation, but replacing V_α^d in equation (5.12) by V, that is, the *Ne*-*Ne* interaction. The computed values of $\langle R_s \rangle_p$ are summarized in Table 6.1.

As mentioned above, in the 9^{th} shell of the pure f.c.c. structure, there is a subset of 12 atoms lying along the main crystallographic axes defined by the impurity centre and the atoms of the 1^{st} shell. The particles in this subset, denoted as the $9b$ subshell, are located at nearest neighbours distance of the atoms of the 4^{th} shell. For an infinite and pure f.c.c. structure, the radii of the $9a$ and $9b$ shells coincide. The small differences observed in the calculated $\langle R_s \rangle_p$ values of these shells are due to the use of a finite number of terms in the potential energy expansion of equation (5.12).

To illustrate the static effects of electronically exciting the impurity, the relaxation procedure is repeated, with the impurity-rare gas potential corresponding to the Rydberg state, A. The average values of $\langle R_s \rangle_X$ and $\langle R_s \rangle_A$ of the first shells

($s \leq 10$), with the impurity in its ground electronic state, $NO(X)$, and in the excited state, $NO(A)$, and their shifts with respect to the pure neon solid, respectively, are presented in Table 6.1 and in Figure 6.1.

Table 6.1: Shell structure and main properties of the radial model. First column: shell number. Second column: number of atoms n_s in shell s. Third column: radii of shells, assuming a pure matrix. Fourth and five columns: radial expectation values of the relaxed matrix, with the impurity in the ground, *NO(X)*, and excited, *NO(A)*, electronic states, respectively. All distances are expressed in atomic units.

s	n_s	$\langle R_s \rangle_p$	$\langle R_s \rangle_X$	$\langle R_s \rangle_A$
1	12	5.83	6.16	7.21
2	6	8.15	8.10	8.30
3	24	10.02	10.11	10.47
4	12	11.59	11.72	12.38
5	24	12.91	12.92	13.03
6	8	14.17	14.21	14.39
7	48	15.30	15.34	15.56
8	6	16.35	16.37	16.46
9a	24	17.34	17.35	17.44
9b	12	17.36	17.42	17.76
10	24	18.28	18.29	18.38

The results shown in Figure 6.1 allow to quantify the effect of the presence of the impurity in the solid. It is observed, that the radial displacement of the *Ne* atoms that surround the impurity, due to the presence of the latter, is not a monotonic function of the distance to the origin. Instead, this magnitude presents peaks for some non-contiguous shells, i.e., the shells $s = 1, 4, 9b, \ldots$. The explanation is as follows: the 1^{st} shell shows the most important displacement, with respect to the pure matrix, of about 0.26 a.u. (4.5 % of its initial value), because the repulsive branch of the interaction potential *NO-Ne* is dominant at the distance at which this shell is placed in the pure neon solid. In the crystal, the second shell is located at a distance (approximately 8.13 a.u.) at which the *NO-Ne* potential is rather small, but attractive, which explains the weak contraction of this shell. For the third and all subsequent coordination shells, the *NO-Ne* interaction is negligible and the

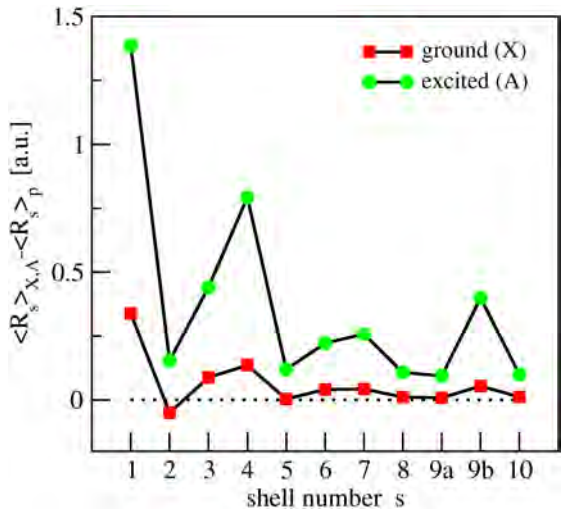

Figure 6.1: Expectation values of the shell displacements R_s (with respect to the pure crystal), caused by the presence of the *NO* impurity in a substitutional site in the matrix. Squares correspond to the impurity ground state and circles to its first Rydberg state.

displacement is due to the motion of the neighbouring *Ne* atoms. This becomes specially important for the fourth shell: the atoms in it are separated by the nearest neighbour distance (see Figure 5.2) from the atoms of the first shell. Therefore, the atoms in the fourth shell deviate from their initial positions (1.3%) as a consequence of the outwards shift of the atoms of the first shell. In this way, each of the particles in the first shell defines a geometric line, from the impurity, on which the *Ne* atoms are located at nearest neighbours distance. The major distortion is propagated along these directions.

As mentioned above, for those shells where only a subset of atoms lie on these privileged axes, the displacement of these atoms is treated independently from the subshell that is not connected to these axes. This allows to take into account the large differences in the radial collective displacements of these subsets, when the impurity is present. The importance of this structural effect is more clearly visualized in Figure 6.1, for the shells $s = 9a$ and $s = 9b$. Both have the same mean radial distance in the undoped matrix, whereas, in presence of the impurity, their relative

displacements are noticeable different. The atoms of the shell $9b$ are placed along the privileged axes and are displaced by 0.05 a.u. with respect to its position in the pure matrix, while those in the shell $9a$ are almost unaffected by the impurity. This effect has also been observed by previous molecular dynamics simulations [5].

Since the relaxation of the system back to the electronic ground state, X, after the excitation to the A state, is a rather slow process (the lifetime of the Rydberg state in the neon matrix is of about 200 ns [140, 141]) compared to the characteristic time scale of the structural dynamics (a few picoseconds), it is interesting to analyse the equilibrium positions of atomic nuclei on the new potential energy surface, corresponding to the NO in the A state, and to compare them with those of the pure crystal and of the doped matrix, with the NO in the ground electronic state. The radial displacements of the Ne atoms around the impurity, when the latter is in the excited state $NO(A)$, reported in Figure 6.1 and in Table 6.1, confirm that the main deformation occurs for the atoms that lie on the axes defined by the impurity centre and the atoms of the first shell. The marked amplitude of the deformation of the first shell owes to the characteristics of the Rydberg state *NO(A)* discussed above, specifically the relation between the spatial distribution of the orbital and the distance from the centre of mass of NO and the first nearest neighbours shell. As a result of the repulsive interaction between the electronic clouds, the atoms of this shell are displaced from their initial positions by around 1 a.u..

From these static results it can be concluded that the electronic bubble formation is not a one-dimensional motion of the first shell, but it is a collective motion that involves a large number of shells. The bubble dynamics and the ultrafast propagation of the perturbation in the solid, arise from the complex interaction among a considerable number of coupled degrees of freedom.

The stationary absorption spectra, calculated using equation (5.47), allows to fit

the parameters in the interaction potentials $V_\alpha(R_s) = A\,exp(-\beta(R_s - r_0))$ ($\alpha = A, C, D$), in order to reproduce, to the maximum extent possible, the experimental spectroscopic results (Table 5.1). The comparison between the calculated and experimental [8,9,93] lineshapes is shown in Figure 6.2.

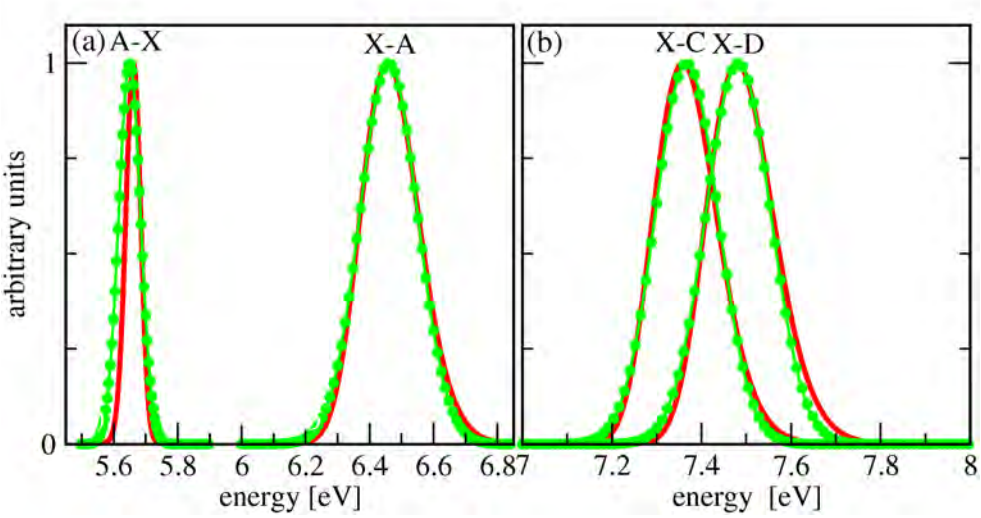

Figure 6.2: Simulated absorption and emission spectra of the doped solid. In the left panel (a), the transitions between the electronic ground state to the first Rydberg state of the impurity, A, are shown. In the right panel (b), the absorption from the ground state to the excited electronic states C y D of NO, are illustrated. The solid lines represent the computed spectra while the circles represent the experimental data points (Ref. [9]).

The optimization of these spectra lead to the values of the parameters reported in Table 5.1. It is found that the new *Ne-NO(A)* interaction is slightly more repulsive, compared to the potential energy surfaces generated from the fitting of the same experimental spectroscopic data to the results of classical MD simulations [4]. The interactions between each Ne atom and the NO impurity in the states C and D are required to model the full pump-probe signal, since in the experiment we want to compare with [9], the probe step is done by an ultrafast excited state absorption to those states. Each of these transitions occur at distinct stages of the process: the photo-absorption $NO(A \leftarrow X)$ marks the start of the geometrical rearrangement of

the *Ne* atoms that surround the impurity, while the photo-excitation from the A state of *NO* to the Rydberg states of higher energy, C and D, is used to monitor the system dynamics. Since the potential parameters reported in Table 5.1 reproduce the absorption and emission spectra between the electronic states involved in the excitation and detection processes, they are expected to provide, at least qualitatively, a correct description of the influence of the interaction between the molecule and the nearby media on the time evolution of the system.

6.1.2 Geometrical rearrangement and energy redistribution in the matrix

The excitation of the *Ne* matrix doped with *NO*, using a pump laser pulse characterized by a temporal width of 280 fs and a central wavelength $\lambda = 192$ nm, consists in the population of the first Rydberg state (A) of the *NO* molecule. The parameters of the laser pulses used in our simulations were those of the pump-probe experiments carried out in the group of Prof. M. Chergui [5]. To model this process, taking into account explicitly the parameters of the pump laser pulse employed in the experiments, the multidimensional Schrödinger equation (5.14), for the coupled X and A states of *NO*, is solved numerically. To this aim, the ground state wave function, obtained through the relaxation method detailed in section 5.2.2, is used as initial wave function. The propagation is performed using the Heidelberg MCTDH package [16]. The coupling with the external electromagnetic field leads to the creation of a non-stationary excited state nuclear wave packet $\Psi_A(\mathbf{R}, t)$.

To analyse the dynamics of this wave packet, the reduced one-dimensional densities for the 1^{st}, the 3^{rd} and the 4^{th} shells, are illustrated in Figure 6.3.

In the figure, the effect of the finite temporal width of the excitation pulse is clearly

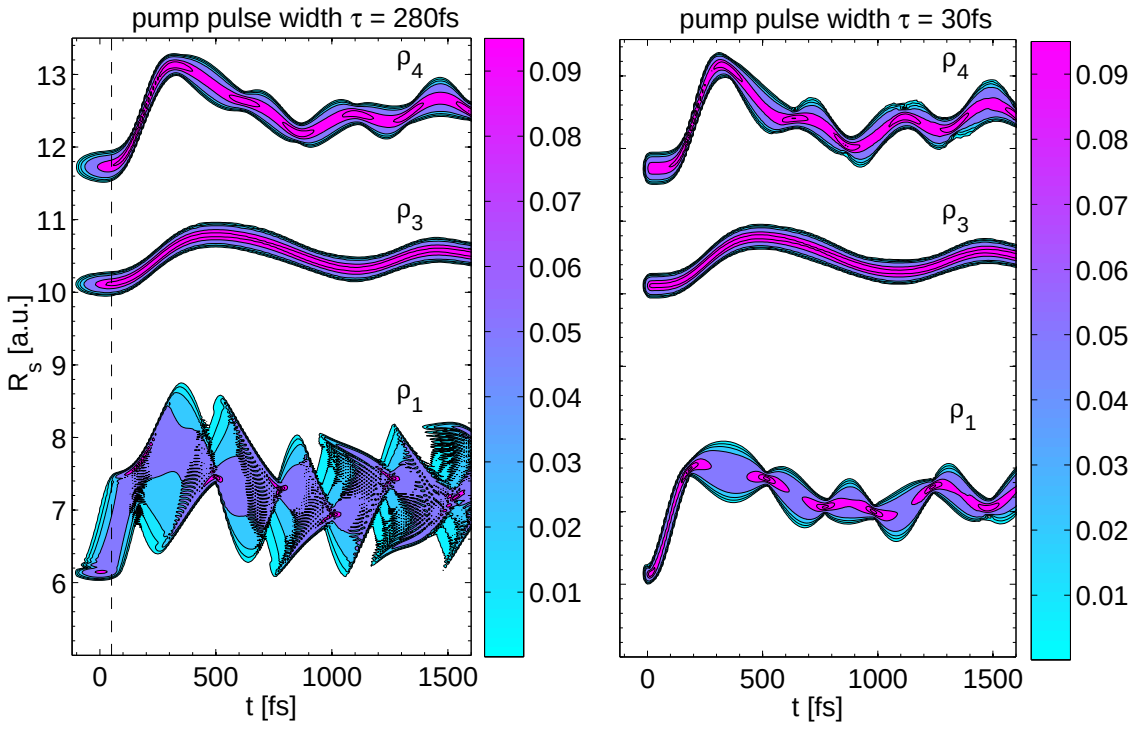

Figure 6.3: Reduced densities, for the first few shells, evaluated from the wave packet $\Psi_A(\mathbf{R}, t)$ formed as a consequence of the electronic excitation caused by a pulse of 280 fs (left panel) and 30 fs (right panel). Especially, the reduced density $\rho_A^{(1)}$ is strongly affected by the pulse shape effects. The vertical line indicates the departing time of the outward motion of the fourth shell.

shown. In the left panel, the densities of the shells mentioned above are illustrated for an excitation pulse width of 280 fs (Full Width at Half Maximum), and in the right panel, for a width of 30 fs.

In both cases, for the 1^{st} shell, the creation of the wave packet in the excited state by the laser pulse around $t = 0$, and its ulterior motion outwards during the first 200 fs are observed. This behaviour is consistent with the previously reported experimental results [4], reflecting the initial dynamics of bubble formation. Consistent with the findings above, for the mean radii in the state $NO(A)$ (see Figure 6.1), the second shell exhibits only a weak displacement. However, the comparison between $\rho_A^{(1)}(R_1, t)$, $\rho_A^{(3)}(R_3, t)$ and $\rho_A^{(4)}(R_4, t)$ demonstrates more clearly the propagation of the perturbation along the preferential axes described in the previous section. When a pump pulse of length equal to 280 fs is used, complicated structures are observed in the time evolution of the wave packet, i.e., it presents strong dispersion and contraction patterns. This is a purely quantum effect due to the temporal width of the pump pulse, which is comparable to the time scale of bubble expansion. The portion of the wave packet, promoted earliest to the state A, reach the fourth shell after approximately 50 fs, and pushes it outwards, while itself being reflected inwards (see the discontinuous line in Figure 6.3). However, in this instant, the excitation pulse is not over yet, and the parts of the wave packet promoted towards the end of the pulse can move freely to larger distances (since the 4^{th} shell has already departed), encountering, while it moves, the earlier returning parts. This cause the complex interference patterns and the profound breathing of the wave packet observed. The large dispersion of $\rho_A^{(1)}$ between 150 fs and 300 fs clearly shows the simultaneous motion in both directions. This scenario then repeats itself with a deformation of the wave packet due to effect of anharmonic contributions of the confinement potential, exerted on the 1^{st} shell by the rest of the matrix. In the case of a 30 fs pump pulse,

which is much shorter than the time scale of the bubble expansion, a more compact wave packet is obtained, without the pronounced interference patterns observed for the excitation pulse width of 280 fs.

Regardless the pulse length employed, with a time delay of 100 fs, the fourth shell, being coupled to the first one by nearest neighbours interactions, gets strongly pushed outwards due to the motion of the atoms of the first shell. For longer times, the coupled shell dynamics becomes more complex and it shows an interesting aspect: the response of the matrix is such that, around 1 ps after the photo-excitation, the fourth shell contracts down to approximately 12 a.u., forcing the distribution $\rho_A^{(1)}$ to move to smaller distances, as well. This bubble contraction time has been observed experimentally [3, 5], and the values inferred from these measurements are in good agreement with the simulations presented in this thesis.

To illustrate this point, in Figure 6.4, the mean values of the radial positions of the first shells, in the case of a 280 fs excitation pulse, are shown.

In the left panels are shown the shells which are connected along the crystallographic (110) axes, and in the right panel, those shells whose atoms do not lie along the (110) axes but are at nearest neighbours distance of the corresponding ones in the left panel. In this Figure, it can be seen that the propagation occurs mainly along the main axes, formed by the atoms of the shells $s = 1, 4, 9b, 15, 24b, 34b, \ldots$. The vertical lines in each diagram indicate the time instant at which the following shell of the axis is set in motion due to the collisions with the previous one, i.e., the time instant at which the collisions between the atoms lying on the principal axes take place. For example, the dotted lines in the first graph correspond to the time elapsed until the begin of the expansion of the fourth shell. It is interesting to notice, that though the energy propagation into the solid occurs mainly along the privileged axes, by mean of direct collisions of the atoms along them, there is an alternative mechanism of energy

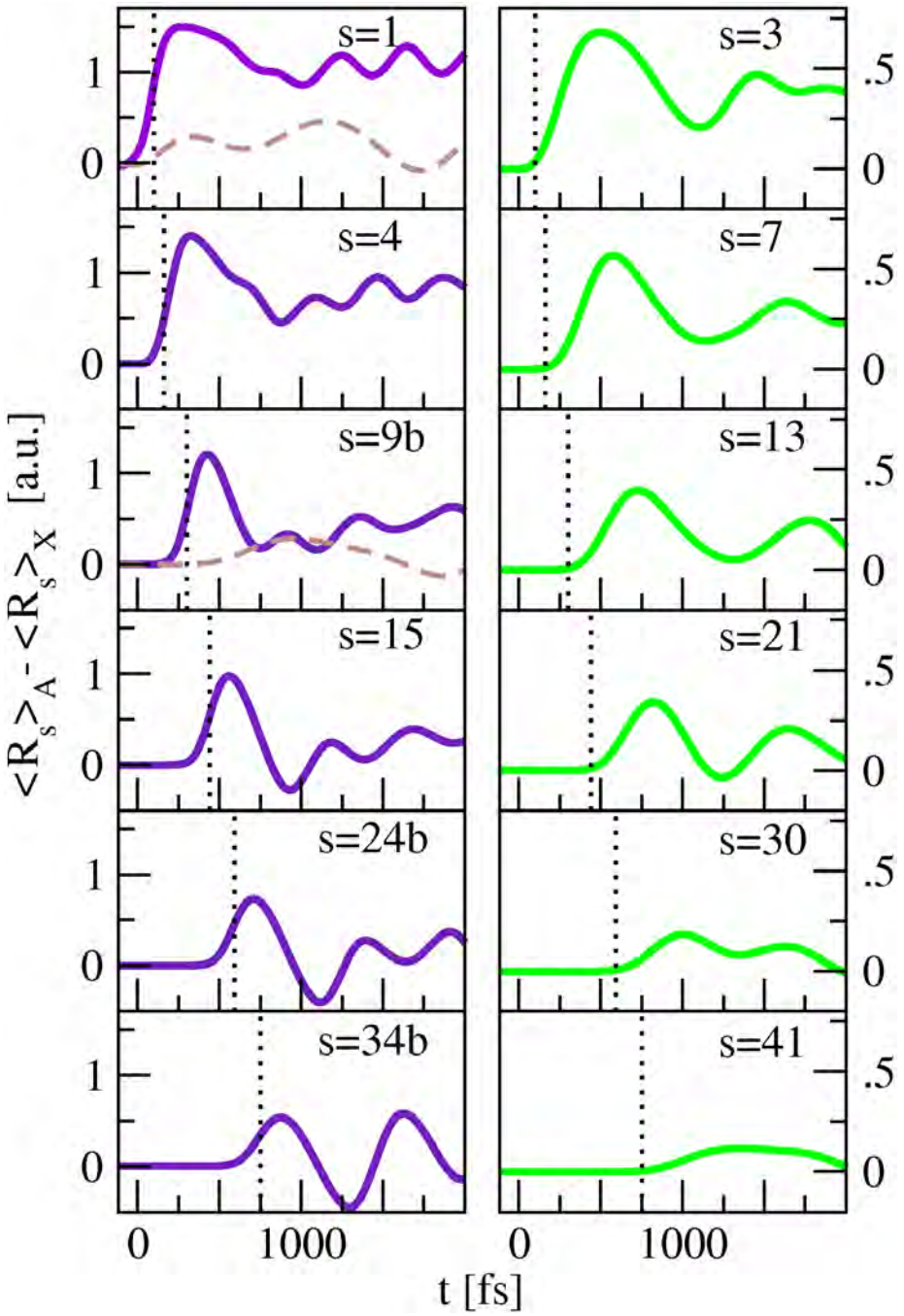

Figure 6.4: Time evolution of the average positions of different shells during the first 2 ps of the dynamics. In the left column, the shells whose atoms lie along the main crystallographic axis (110), are shown. For the sake of comparison, the "silent" shells $s = 2$ y $s = 9a$, have been included as discontinuous lines in the first and the third panels, respectively. The dotted vertical lines in each diagram indicate the time instant at which the following shell, along the principal axis, is set in motion. The right panels illustrate the expectation values of the radii of the shells that undergo side collisions with the corresponding ones to the left (note the differences in the scales).

redistribution through side collisions with atoms placed outside the main axes, but which are at nearest neighbours distance of the (110) lines (right panel). This fact can be appreciated in the figure: the 1^{st} shell, for example, collides at the same time (vertical line) with the 4^{th} and the 3^{rd} shells, though the latter collision is less intense.

These mechanisms of energy propagation into the rare gas matrix can be better visualized in Figure 6.5.

In this plots, the kinetic energies of different shells, as function of time, are shown. During the first 90 fs, the fast acceleration of the first shell, termed "bubble expansion" is shown. After regular time intervals, the shells directly connected to the first one ($s = 4, 9b, 15, 24b, 34b, \ldots$) start to get accelerated, thereby showing the ultrafast energy transfer in the solid. However, the energy is not only transported along these axes. Other shells are also set in motion, although with with less intensity (see right panels in Figure 6.5. Notice the differences in the scale). This is caused by the *Ne-Ne* interaction between the atoms located along the main crystallographic axes and the atoms separated from them by the nearest neighbour distance, but placed outside these axes. For example, the *Ne* atoms in the 3^{rd}, 7^{th} and 13^{th} shells are located, initially, at a distance of approximately 5.9 a.u. (the nearest neighbours separation in the lattice) of the shells 1^{st}, 4^{th} and $9b$, respectively, though they are not on the principal axes. The motion of these shells is activated indirectly through the large amplitude displacements of the 1^{st}, 4^{th} and $9b$ shells. These mechanisms, which are illustrated in the right panels of the figures 6.4 and 6.5, show the side collisions of the atoms of the main axes with these secondary shells as function of time. In the first graph, for example, the coincidence of the departure times of the shells 3^{rd} and 4^{th}, 7^{th} and $9b$, and so on, is observed. On the other hand, the second figure shows that, indeed, the kinetic energy of the atoms belonging to every main axis shell is distributed between both neighbouring shells. It suggests that the energy of the 1^{st}

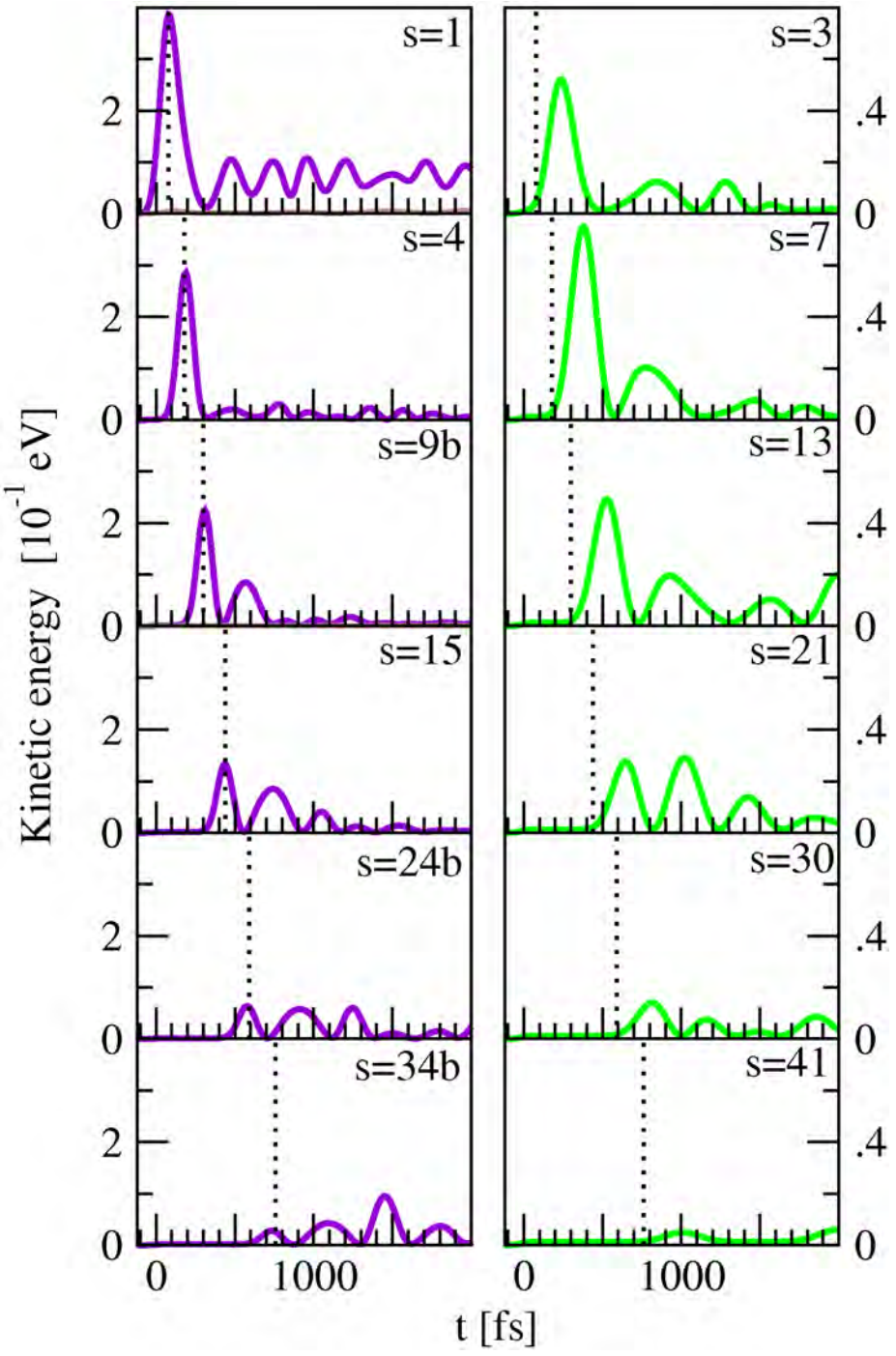

Figure 6.5: Time evolution of the kinetic energies of the shells whose atoms lie along the privileged axes (left panel) and their off-axis nearest neighbours (right panel). The vertical lines coincide with the times indicated in Figure 6.4.

shell initially distributes between the 3^{rd} and the 4^{th} shells, and the same happens with the 4^{th} shell, that delivers its energy mainly to the shells 7^{th} and $9b$.

In summary, the dynamics present two fundamental aspects: direct collisions take place, which cause the fast energy transfer between consecutive shells formed by atoms lying on the privileged axes, accompanied by a weaker excitation of the remaining shells, by lateral collisions. These latter shells form a dissipative "bath" affecting the primary dynamics. A remarkable feature is that the "bath modes" in this system are not formed by remote atoms, but for those which are placed at unfavourable positions in the rare gas matrix with respect to the impurity.

From the data in Figure 6.4, taking into account the time interval from the begin of each shell relative displacement and the instant at which they reach the respective maxima, and the magnitude of these maximal displacements, te propagation velocity of the initial perturbation can be estimated. This velocity is of approximately 3500 m/s (this is a supersonic speed in this medium). Such supersonic expansion has been also observed and described experimentally [4].

To which extent the complex time evolution of the system configuration and the energy transfers in the solid are reflected in pump-probe experiments, is addressed in the following section.

6.1.3 Transient absorption spectra

To the aim of monitoring, in a pump-probe experiment, the dynamics of *Ne* atoms in the doped matrix after photo-excitation of the impurity, the second laser pulse (*probe laser*), retarded in time with respect to the first one (*pump laser*), induce a transition to higher energy levels of the system. The choice of the final state is determined by the possibility to measure the transferred population. The probe pulse used in the experiment which we want to compare our results with [5], induce a transition to the

electronic states C and D of NO.

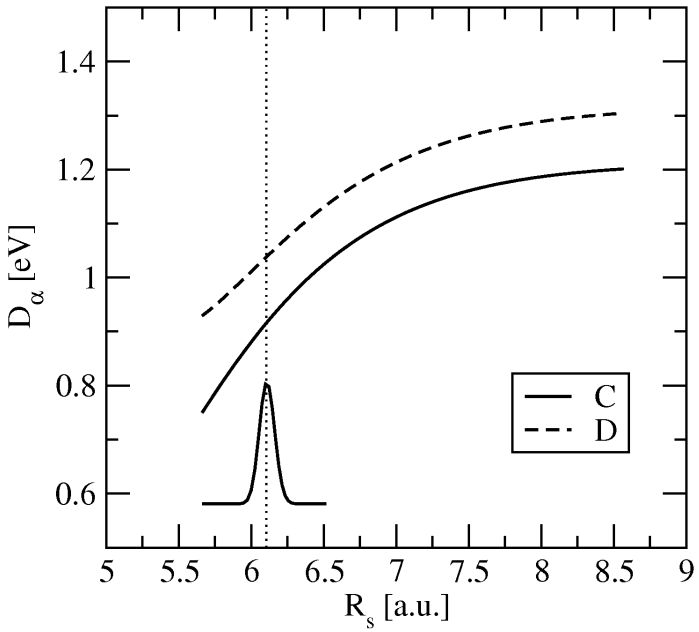

Figure 6.6: Potential energy differences $D_\alpha(R_1) = W^d_\alpha(R_1) - W^d_A(R_1)$, where $\alpha = C, D$. This difference enables to determine the dynamical Franck-Condon points, R^*_1, for the central frequencies of the probe pulse. The vertical lines indicate the location of the centre of the wave packet corresponding to the first shell at the begin of the dynamics.

The expression (5.53) illustrates how the filter function maps the motion of the wave packet associated to the first shell into a measurable pump-probe signal. In Figure 6.6 the differences of the potentials corresponding to the states C and D, with respect to the ground state X, are shown. These differences enable a clear analysis of the pump-probe signals to be expected: for a given central frequency of the laser, the dynamical Franck-Condon points are defined by the relations $D_C(R_1) = \hbar\omega$ and $D_D(R_1) = \hbar\omega$. The fact that both $D_C(R_1)$ and $D_D(R_1)$ are monotonous functions of R_1 (these curves are practically parallel), implies that one can establish a simple connection between the time evolution of the radial density $\rho^{(1)}_A(R_1, T)$ and the pump-probe signal, for a given frequency of the probe laser. In this way, if one scans smoothly the wave length of the probe laser pulse over a wide range, in principle, it

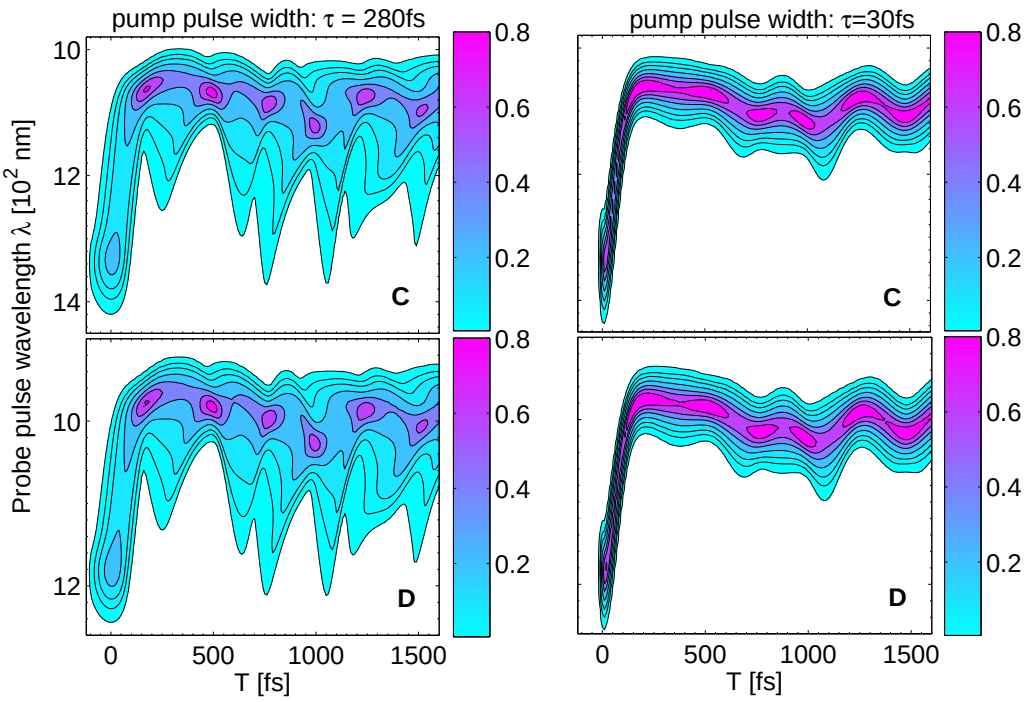

Figure 6.7: Pump-probe signals as function of the probe laser wavelength and of the time delay between the pulses. The left and right panels correspond, respectively, to excitation (pump) laser pulses of 280 fs and 30 fs. The simulated signals correspond to the transitions from the first Rydberg state to the C (upper panels) and D (lower panels) states.

is possible to make a "photograph" of the moving wave packet that represents the 1^{st} shell, making eventually fine quantum properties of the matter wave visible [135,142].

In Figure 6.7 are shown the calculated pump-probe signals, corresponding to the excitation of the states C and D, as functions of the probe laser wavelengths, for pump pulses of lengths 280 fs (left panels) and 30 fs (right panels), respectively. The overall structure for excitation to the C and D states is comparable, and shows the same main features: at the initial time, when the radius of the first shell is around 6 a.u., the resonance condition holds for the two states C and D, for wavelengths of 1300 and 1200 nm, respectively. The rapid expansion of the first shell upon excitation by the laser pulse leads to a drastic shift of the resonance point to wavelengths at

around 1100 nm and 1000 nm for the states C and D, respectively. Then, for times longer than 200 fs, the signal shows fairly regular oscillations around 1100 nm for the excitation to the C state and around 1000 nm, for the excitation to the D state.

As has been detailed above, and it is evidenced by equation (5.53), this behaviour reflects the dynamics of the first shell, since the signal is a smeared out image of the time evolution of $\rho_A^{(1)}(R_1)$. The periodic dispersion and refocusing represented in Figure 6.3 are also present in this signal. It can be also noticed, that for the time at which the first bubble contraction takes place ($\approx$ 1 ps), the signal can be detected at fairly large wavelengths, close to the characteristic values of the initial resonance points. For specific wavelengths, this relationship becomes more striking. In the case of the excitation with a short length laser pulse, the less pronounced structures of the radial densities depicted in Figure 6.3 are also reflected in the spectra. In this case, the initial wave packet is more compact both spatially and temporarily, in such a way that the front and the later parts of the wave packet are very close to each other and they practically do not self-interfere. As a consequence, the wave function is less structured and it remains more localized around the average radii.

To compare with the experimental transient spectra, the contributions $P_C(T)$ and $P_D(T)$ (indicating the transition probability to the states C and D, respectively) have to be added, since the measured signal, i.e., the depletion of the A state population, is proportional to the transient absorption probability and it is not possible to discriminate which portion of the population goes to the state C or D. The results plotted in Figure 6.8 are precisely the sum $P(T) = P_C(T) + P_D(T)$ for different probe pulse wavelengths, using the same (arbitrary) value for the transition dipole moments, μ_{CA} and μ_{DA}, which are unknown. In this case, the temporal width of the pump pulse is set equal to 280 fs, in agreement with the laser pulse employed in the experiment. In this figure, the total computed absorption probability is compared to the experimen-

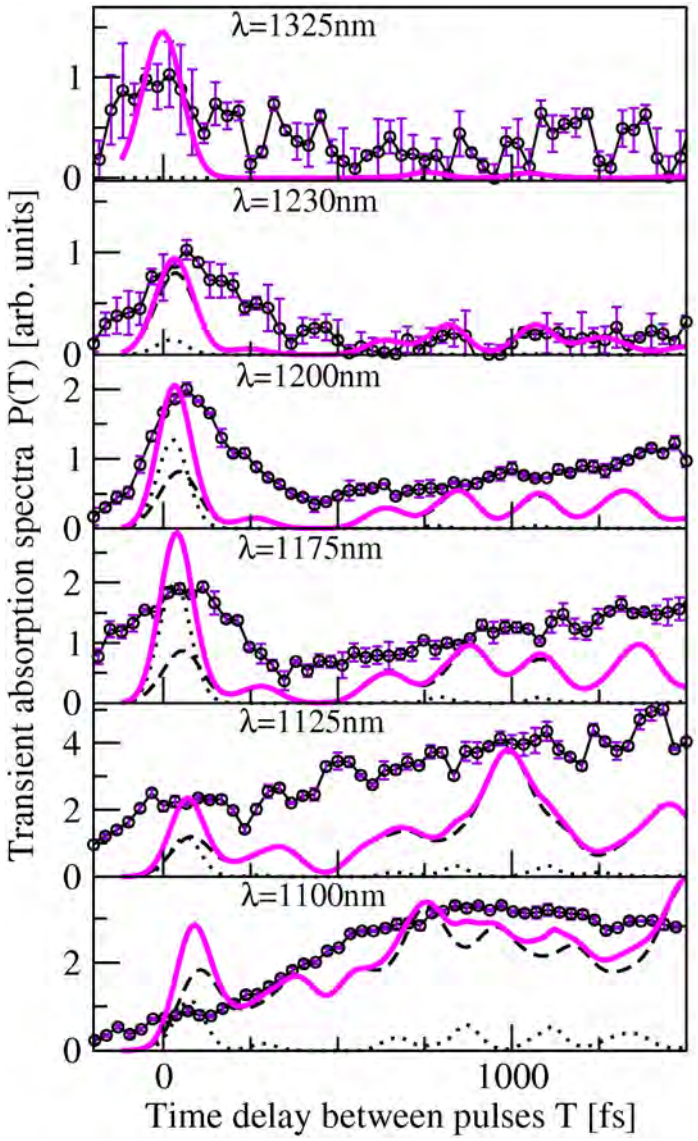

Figure 6.8: Transient absorption probability $P(T)$ (continuous lines), as function of the delay time T between the pump and probe pulses, and the contributions $P_C(T)$ (dashed lines) and $P_D(T)$ (dotted lines) due to transitions to specific states. The circles and error bars represent the experimental data of Ref. [4].

tal transient signals reported in [3, 5], represented by circles, using a common scaling factor for all the wavelengths considered.

The detected signal, for high wavelengths, captures the initial expansion of the bubble. It presents an initial peak, followed by a slow later increase of the signal, which reflects the bubble retraction at around 1 ps, to finally settle around the new equilibrium value. For the low wavelength detection, the initial peak is less pronounced, which reflects that during the primary bubble expansion large cavity radii are reached, while the structures that appear at longer times, indicate the oscillations of the electronic bubble at these times. For these wavelengths, the dynamical Franck-Condon point, coincides with the value of R_1 (approximately 8.5 a.u.) around which the first shell establishes itself for long times. Dashed and dotted lines indicate the contributions of the states C and D, respectively, to these spectra. It is important to highlight that for wavelengths shorter than $\lambda = 1200$ nm, both states contribute. In fact, the intensity of the detected signal doubles for this specific wavelength, since each state contributes in a similar proportion. The latter prediction has been corroborated by experimental observations [3, 5] and can be appreciated in Figure 4.6.

It can be seen, that the theoretically calculated signals qualitatively reproduce the experimental results, although the results of the simulations present much more pronounced structures. These deviations can be explained as a result of three main causes: first, the radial shell model developed in this work neglects the effects of the anisotropy of *NO-Ne* interaction, which would break the spherical symmetry; second, the impulsive approximation introduced to account for the probe step in the calculation of the pump-probe signals, is based on the assumption that this pulse acts during a time interval much shorter than the characteristic time scale of the system dynamics; and third, the dynamics itself is treated within the time dependent Hartree approximation. It is expected that a correlated, multi-configurational

dynamics, would lead to a stronger dispersion of the radial densities and, therefore, also of the simulated signals.

Summing up, as a result of the study of the dynamics of this molecular system, it is found to be characterized by a complex, high-dimensional quantum dynamical behaviour of the atoms of the matrix. The dynamical process consists in a shock-wave-like propagation of the initial matrix perturbation along the crystallographic axes defined by the nearest neighbours of the impurity. Other atoms, even closeby, can be fairly unaffected, and form a sort of "bath" to which the energy flowing along the (110) axes is dissipated. The calculated observables qualitatively agree with the experimental results, pointing at the feasibility of the proposed model to account for the essential features of this phenomenon: the ultrafast initial formation of the bubble, its contraction at around de 1 ps and the subsequent relaxation dynamics, owing to the coupling with other shells. However, the bubble contraction is not simply a direct rebouncing of the first shell, but a collective response of the matrix, which involves a large number of surrounding atoms forming other shells. The main difference between the simulations presented above, with respect to the experimental measured signal, is that the theoretical results exhibit a much more structured behaviour. As detailed above, this behaviour can be associated to the radial approximation of the interaction inherent to our model, and also due to the fact that the dynamics has been investigated using the time dependent Hartree approximation.

6.2 Role of dynamical correlations

To asses the quality of the Hartree approximation for the investigation of the structural relaxation of NO doped neon matrices, an additional study has been carried out, based on the inclusion of several configurations within an MCTDH approach. In

this case, the increment of the number of configurations, at least for those shells which are strongly coupled, allows to evaluate the degree of correlation and, therefore, the validity of the Hartree approximation presented in the previous section.

6.2.1 Analysis of the populations of natural orbitals

To evaluate the magnitude of correlations among the shells which play a major role in the relaxation dynamics of the system, the eigenvalues of the single-particle density matrix operator associated to each degree of freedom κ, have being calculated as function of time, as defined in (5.35).

These eigenvalues, $C_{j_\kappa}^{(\kappa)}$, known as "natural populations", give a measure of the degree of correlation: they describe the weight of the natural orbitals, thus indicating how many SPFs, or configurations, are needed for each degree of freedom to guarantee the convergence of the results. For instance, in the case that the time evolution of the multidimensional wave function is well described within the Hartree approximation, the natural orbital will coincide with the Hartree product and the natural population corresponding to this orbital will be 1.

Figure 6.9 shows the time evolution of the populations of natural orbitals, $C_{j_\kappa}^{(\kappa)}$, for the chain modes, S_p, together with the corresponding expectation values for the different shells. Four configurations were used to represent the wave packets associated to the 1^{st} and the 4^{th} shells and three configurations for the remaining modes in the subspace S_p.

As first result, we find that the high-dimensional ground state is extremely well described by a factorized Hartree wave function. At $t = 0$, it can be noticed that only one coefficient per mode suffices to fully describe the vibrational ground state, and the population of natural orbitals takes its largest possible value, that is, it is equal to one. The femtosecond excitation to the A state of NO is treated within the impulsive

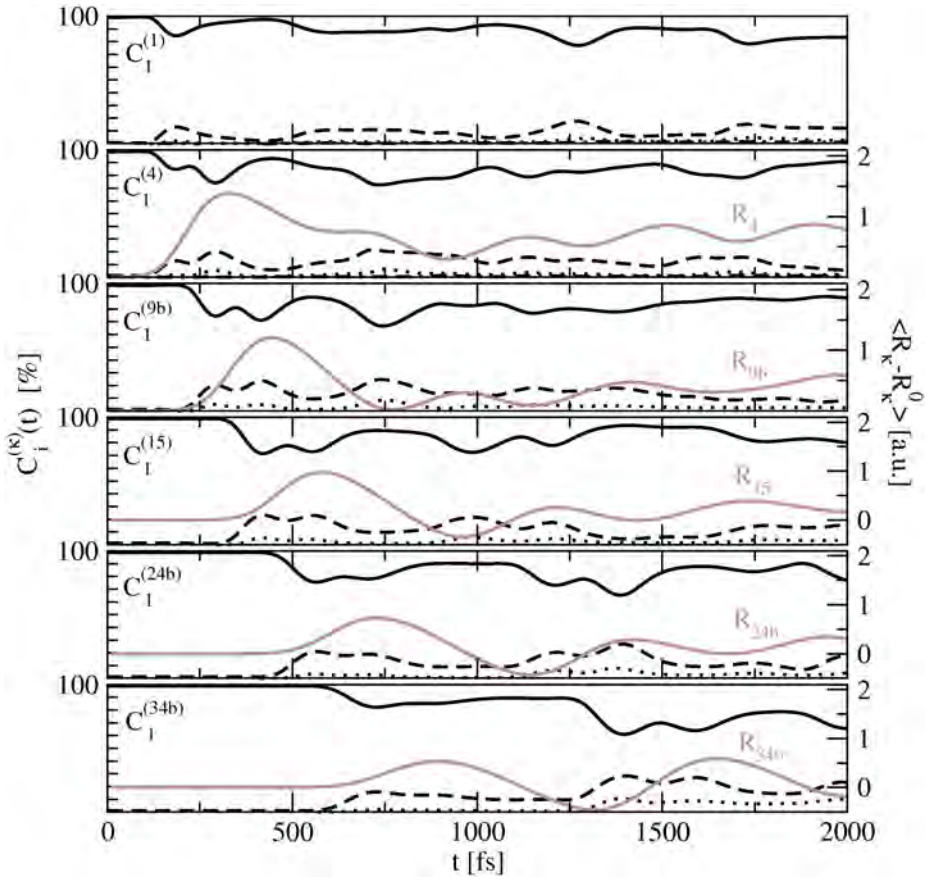

Figure 6.9: Time evolution of the natural populations. The results are shown for the modes of the main crystallographic axes (α = 1, 4, 9b, 15, ...), as indicated inside the figures. The populations $C_1^{(\alpha)}$, $C_2^{(\alpha)}$, $C_3^{(\alpha)}$ and $C_4^{(\alpha)}$ of the different configurations are represented by the solid black, dashed, dotted and dark grey lines, respectively.

limit approximation [135], which results in promoting the ground state wave function onto the electronically excited state. Upon photo-excitation, the 1^{st} shell expands freely until it collides, at around 200 fs, with the atoms of the 4^{th} shell. This initial motion, up to 200 fs, is still well represented by a wave function which consists in a single Hartree product. However, as soon as the collisions takes place, the motion of the 1^{st} and the 4^{th} shells becomes entangled, and the natural populations of each of these shells show that 2 coefficients are necessary to describe their dynamics. This dynamic correlation is induced by the collision, as can be seen from the expectation value $< R_4 >$, which starts to deviate from its initial value at exactly this time.

This scenario repeats itself, while the shock-wave like perturbation propagates along the principal axis and subsequently activates the remaining chain modes. This situation is clearly visible when comparing the deviation of the $C_1^{(i)}$ (solid lines) from its initial value $C_1^{(i)}(t = 0) = 1$, below one with the expectation values of the radii of these modes. Another dynamical structure, underlying the shock-wave like propagation of the dynamical correlations, can be seen when comparing the natural populations $C_2^{(i)}$ (dashed lines): the second natural orbitals, all starting from zero until the perturbation reaches the corresponding shell, always show a pronounced initial double peak structure. The first of these maxima in one shell corresponds to the second maximum in the previous one. Hence, it is the motion of the preceding shell that creates dynamical correlations, which subsequently are passed on to the following shells. To describe the dynamics at later times, 3 coefficients are required for each of the chain modes, which transport the major part of the energy released into the material.

In what follows, the effects of these dynamical correlations onto the energy redistribution, the calculated radial distributions and the experimentally measurable pump-probe signals, are shown.

6.2.2 Energy transfer into the solid

As stated above, the photo-excitation of the *NO* molecule to its excited electronic *A* state, leads to a strong repulsive *NO-Ne* interaction, which pushes the closeby *Ne* atoms outwards. In this way, the energy needed for the electronic transition to occur, deposited by the laser, is transformed into kinetic energy of the nuclear motion. This triggers a shock-wave like perturbation of the atoms in the matrix, which mainly propagates along the privileged axes formed by the shells $s \in S_p$ and the energy dissipation into a "bath", formed by other atoms located outside these axes, which are also set in motion. To visualize this energy redistribution process, the energy of the chain modes as a function of time, for different number of shells included, is evaluated. These quantities have been calculated both for the Hartree wave function and for the correlated one.

In Figure 6.10, the expectation values of the chain Hamiltonian, H_c, both for the correlated (full line) and Hartree wave functions (dashed line), are plotted. All energies in this graph are measured with respect to the energy origin of the excited *A* state of *NO*. The Hamiltonian H_c contains the contributions of the 8 shells that lie on the principal axes. To make the analysis simpler, the initial energy has been shifted by $(n-1)$ times the interaction energy between two neighbouring shells along the principal axes, evaluated for the equilibrium positions of the ground electronic state (for example, $(n-1) \cdot W(R_1, R_4)$). The same energy shift can be applied in all cases, since these interaction energies are very similar for any 2 neighbouring shells in S_p. The index n identifies the shells order along the (110) axis.

First, it can be noticed that the chain energy calculated within the Hartree approximation slightly overestimates the one calculated within the MCTDH approach. The second finding with respect to the mean value of H_c is that there is energy dissipation at two time scales: a rapid initial decrease within the first 500 fs, followed

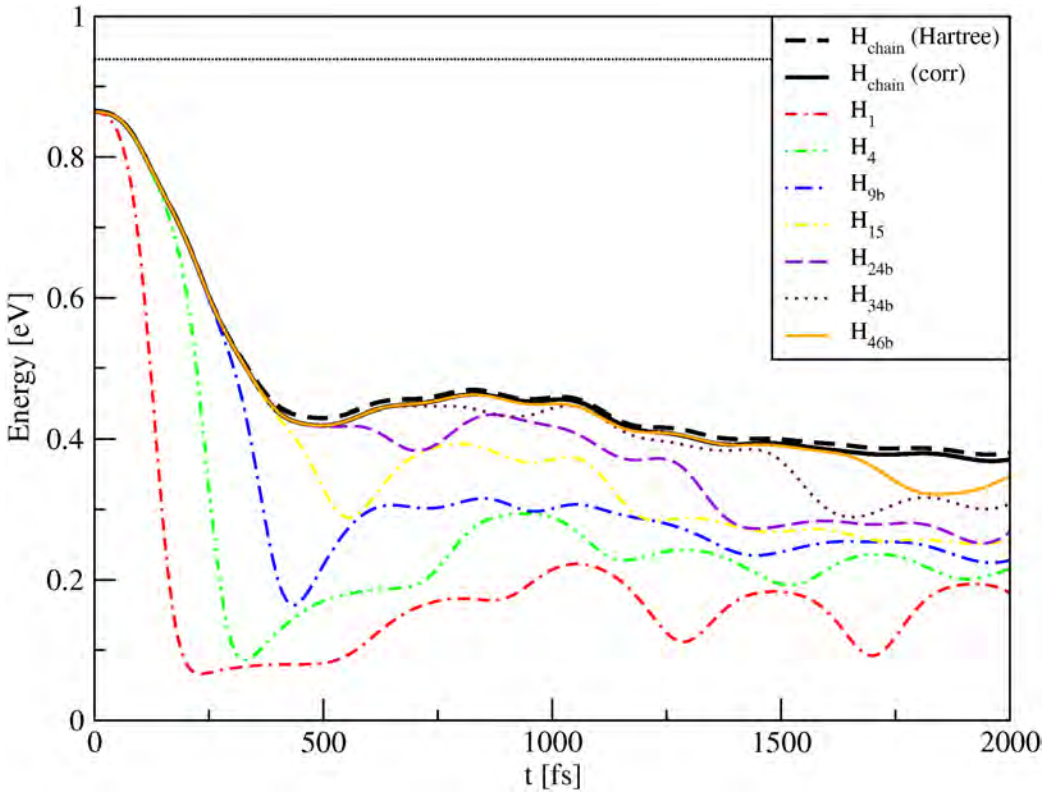

Figure 6.10: Expectation values of the chain Hamiltonian (eq.(5.50)) for different number of shells included in the chain (see text). The thick solid line represents the result of MCTDH calculations for the complete chain. The thick dashed line shows the result for the same magnitude, but within the TDH approximation. In the plot, the rest of the curves correspond to the MCTDH results for the truncated chain, as indicated in the text.

by a slow one for larger times. The initial decrease indicates that about 45% of the total available energy is dissipated into the "bath" modes within the first 500 fs. The cause of this phenomenon is that the atoms of the first shell, which exhibit the most drastic displacement, are strongly coupled not only to the 4^{th} shell (the following atoms in the main axis), but also to the atoms of the 3^{rd} shell. The atoms of the 3^{rd} shell are also at nearest neighbour distances from atoms of the 1^{st} shell, but they do not lie along the privileged axis. This scenario repeats itself for each one of the chain modes (shells $s \in S_p$) lying in the privileged axis. Hence, the atoms of the 3rd shell are also set in motion, leading to a rapid initial dissipation out of the chain modes. The atoms of the other, more remote shells, show a much weaker excitation of the remaining bath modes.

The shock-wave like behaviour of the energy dissipation along the axis can also be visualized when calculating the expectation value of the chain Hamiltonian for an increasing number of shells $s \in S_p$ included. For instance, H_1 denotes the outcome of calculations considering only the 1^{st} shell; $H_{(1,4)}$ is the energy corresponding to the 1^{st} and the 4^{th} shells; H_{9b}, accounts for the sum of the contributions of the 1^{st}, the 4^{th} and the $9b$ shells, and so on. For example, $H_{(1,4)} = T_1 + V_1 + T_4 + V_4 + V_{1-4}$; the Hamiltonian $H_{9b} = T_1 + V_1 + T_4 + V_4 + T_{9b} + V_{9b} + V_{1-4} + V_{4-9b} + V_{1-9b}$ and so on. In the latter example, the contribution V_{1-9b} can be neglected because the interaction between Ne atoms practically vanish for the typical separations between the shells 1^{st} and $9b$. Hence, the Hamiltonian $H_s, s \in S_p$, is the sum of the contributions due to the individual Hamiltonians of the shells identified by indexes not exceeding $s, s \in S_p$, and the interactions between contiguous shells along the main axis. At $t = 0$, the interactions V_{1-4} and V_{4-9b} between these contiguous shells are approximately the same, since, when the impulsive excitation occurs, they are located at their equilibrium configurations in the ground state. In Figure 6.10, the chain energies H_s have

being displaced by the number of terms of the latter type, i.e., the interaction between neighbouring shells, in these Hamiltonians in such a way that their initial values coincide with that of H_1. This makes the information in Figure 6.10, concerning the energy transfer into the lattice, to become more striking.

Considering only H_1, i.e., the energy corresponding to the 1^{st} shell, it can be seen that this energy decreases rapidly within about 200 fs. Such drastic drop indicates the transfer to other modes. When calculating $H_{(1,4)}$ one sees that the drop now occurs within a time interval of 300 fs; and so on. The drop of the chain energy clearly shows the energy transfer along the privileged axis. This energy transfer along the axis persists up to the shell $34b$, which corresponds to a radius of about 35 a.u..

Another important finding concerns the total amount of energy released into the matrix. The upper dotted line indicates the excess energy accumulated in the matrix at $t = 0$, as a consequence of the instantaneous excitation of the A state, measured with respect to the energy origin of this excited state. At the final stage of the dynamics, the chain modes keep 41% of the initial energy. The rest of the energy has been released into the matrix, as a result of side collisions between the chain modes and the "bath" modes. The total amount of energy dissipated into the matrix can be estimated to be 0.0205 a.u. or 0.55 eV , which is in very good agreement with the experimental result of 0.54 eV reported in Ref. [3].

For this study using a different number of chain atoms, we have only shown, for the sake of clarity, the MCTDH results, since the values of the corresponding magnitudes, evaluated within the TDH scheme, are almost identical.

Hence, the overall picture is that a shock-wave like energy transfer occurs, which propagates from the first shell towards the more external coordination shells in the solid. The perturbation is mainly propagated along the (110) crystallographic axis, for about 35 a.u., before its energy is completely dissipated into the remaining sur-

rounding atoms.

6.2.3 Radial densities

In Figure 6.11, the radial densities of the 1^{st} and 4^{th} shells are shown and compared, both for a Hartree wave function and a correlated one. In both graphs one can clearly see the main dynamical features: the initial extension of the 1^{st} shell, colliding at around 200 fs with the 4^{th} shell, thus initiating the energy disposal into the matrix. The magnitudes represented in this graph, as well as in all subsequent calculations,

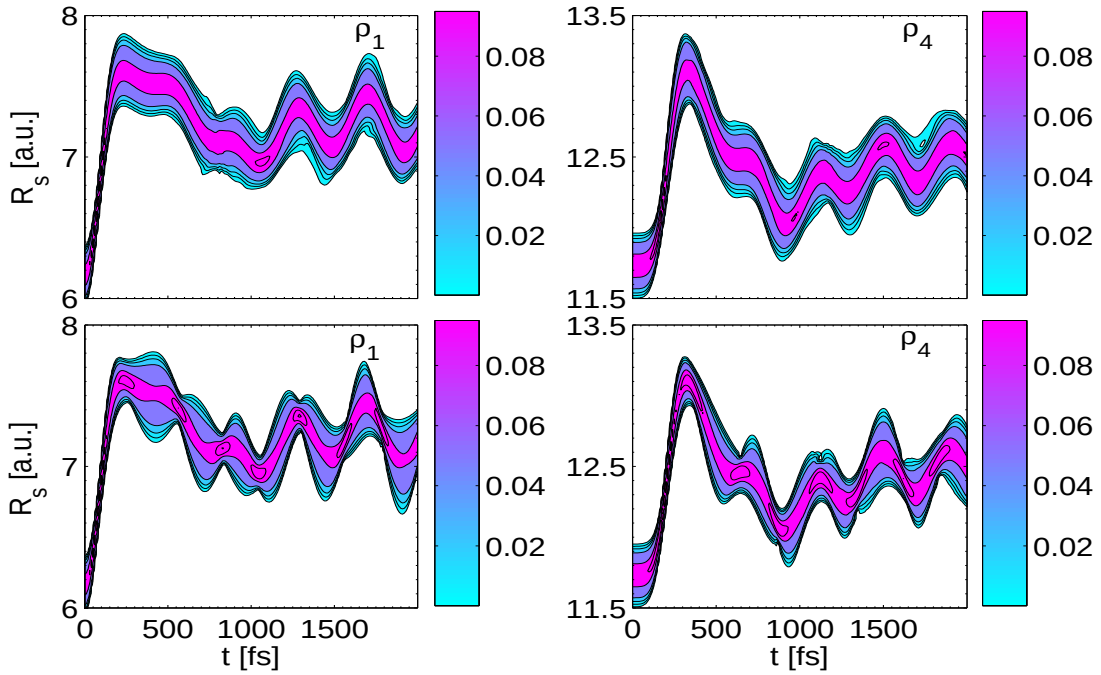

Figure 6.11: Contour plots of probability densities corresponding to the first and the fourth shells. The lower panels correspond to calculations carried out within the Hartree approximation. The upper panels were generated using the correlated wave function.

the correlated wave function was obtained by employing the mode combination of (R_1, R_4). For all the chain modes $R_s, s \in S_p$, included the previous combined mode, 3 configurations have been included in the wave function representation. For the

remaining modes, only one configuration has been considered. These number of configurations per mode is enough to achieve convergence of the numerical integration scheme. In this sense, it is important to remark that if one additional configuration is included for each mode, the weight of the natural orbital associated to this new configuration never exceeds 0.01% of the total. In our case of an 80-dimensional Hamiltonian, the above choice amounts to a total of 2187 configurations (see Table 6.2).

Table 6.2: Number of configurations corresponding to each mode, number of primitive basis functions corresponding to each SPF and the number of atoms in every shell.

Coordinates (R_s)	Number of single-particle wave functions (n_i)	Number of primitive basis functions	Number of atoms in each shell (n_s)
(R_1, R_4)	3	129	(12,12)
R_{9b}	3	127	12
R_{15}	3	101	12
R_{24b}	3	69	12
R_{34b}	3	69	12
R_{46b}	2	61	12
R_{58}	1	51	12
$R_i, i \leq 80$	1	$25 \cdots 55$	$8 \cdots 120$

As could be expected from Figure 6.11, the initial extension of $\rho_A^{(1)}(R_1)$, until 200 fs, is the same in both cases, since before the first collision a Hartree product is enough to describe the wave function. However, after the collision, the dynamical correlations of the wave function are clearly reflected in the reduced densities, which differ appreciably. Specifically, at around 400 fs, the Hartree wave function produce a reduced density $\rho_A^{(1)}$, centred around ΔR =1.3 a.u., whose width is 1.4 times larger than the corresponding spread of the density obtained from the correlated wavefunction.

This behaviour is a variant of the well-known dominating channel problem, inherent to the time dependent Hartree approximation. Since the interaction of one mode with the rest is given by the mean field exerted by the latter on the first, it is

dominated by the main part of the wave packet. In our context this means that the centre of the wave packet describing the motion of the 1^{st} shell pushes the 4^{th} shell outwards. This motion, in turn, has the characteristic that late parts of the wave packet corresponding to the 1^{st} shell can now move freely to larger distances, while the early part already bounces back to shorter radii [11].

In the subsequent dynamics, after the first 200 fs, the reduced densities obtained for the 1^{st} and the 4^{th} shells, using a correlated wave function, are much smoother than those based on a Hartree product. Generally speaking, the correlations lead to less pronounced vibrational coherences. Furthermore, the reduced densities based on the Hartree wave function show pronounced variations in the width, that is, a strong breathing of the density. This behaviour becomes apparent in Figure 6.12, where the expectation values of the first and second moments of the radial distributions are calculated, both for the correlated and the Hartree wave functions.

As first result, one sees that the radial expectation values are extremely well described by a Hartree wave function, which means that the overall dynamics is adequately described by the TDH method. However, the finer details, like the width of the densities are significantly different. Specially, the pronounced breathing of the density calculated within the Hartree scheme, discussed earlier, is clearly seen in the right panels of Figure 6.12. This result confirms the overall conclusion that the dynamical correlations suppress vibrational coherences in the wave function.

To which extent these correlations lead to measurable changes of the transient spectra in pump-probe experiments, is discussed in the next section.

6.2.4 Pump-Probe Spectra

For the sake of simplicity, attention will be focused on the probe excitation to the C-state only, even though it is known that contributions from the D-state are present

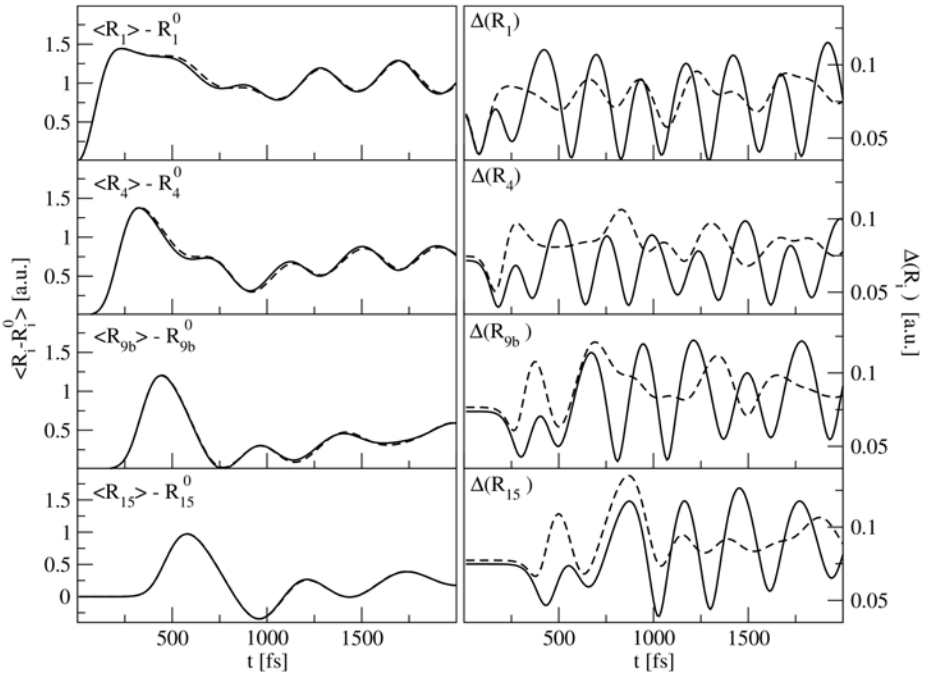

Figure 6.12: Expectation values of the first (left panel) and second (right panel) moments of the radial distribution function, calculated within the Hartree approximation (continuous lines) and using the correlated wave function (dashed lines). The average values of the radii, computed using both methods, are very similar while the variances are significantly different. The pronounced breathing of the Hartree density is clearly seen.

in the measured signal.

Figure 6.13 shows the pump-probe signal as a function of delay time between both pulses, T, and probe wavelength, λ.

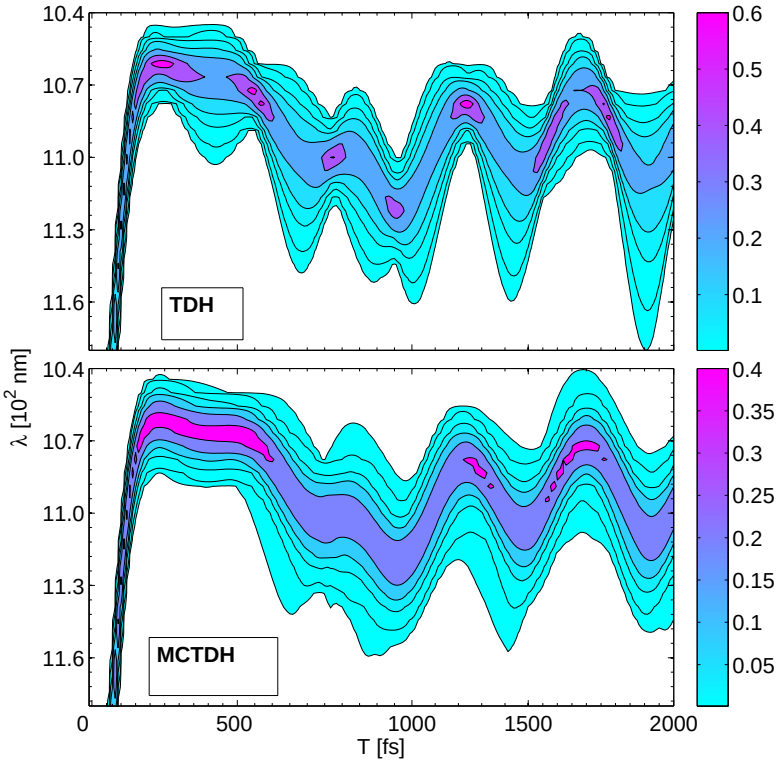

Figure 6.13: Pump-probe signals as a function of delay time T between the laser pulses. Upper panel: TDH approximation results, lower panel: correlated MCTDH results. The same structures observed in the redial densities of the first shell, in both methods of calculation, are present here: the pronounced breathing in the case of the TDH approximation and the smoothing of vibrational coherence in the MCTDH case.

Comparing with Figure 6.11, it can be noticed how the density $\rho_A^{(1)}(R_1, t)$ is mapped into the measurable spectra. Comparing the results of the TDH calculations with the correlated ones, it can be seen that the main features are extremely well described by the TDH result: At early times, we find a rapid shift of the transient-signal to large wavelengths, corresponding to the ultrafast initial cage expansion. At later times, the collisions with the other shells leads to the complicated structures

in the signal, reflecting the damped oscillatory motion of the atoms of the 1^{st} shell. However, one can also see that the differences in the radial density $\rho_A^{(1)}$ described earlier, are mapped into the pump-probe signal. Specifically, the more pronounced variations of the width in ρ_1, within the TDH approach, can also be seen in the pump-probe spectra: the focussing at around 510 fs lead to a more peaked spectrum at these times. Furthermore, the more coherent vibrational dynamics observed in the TDH results lead to more structures in the pump-probe signal.

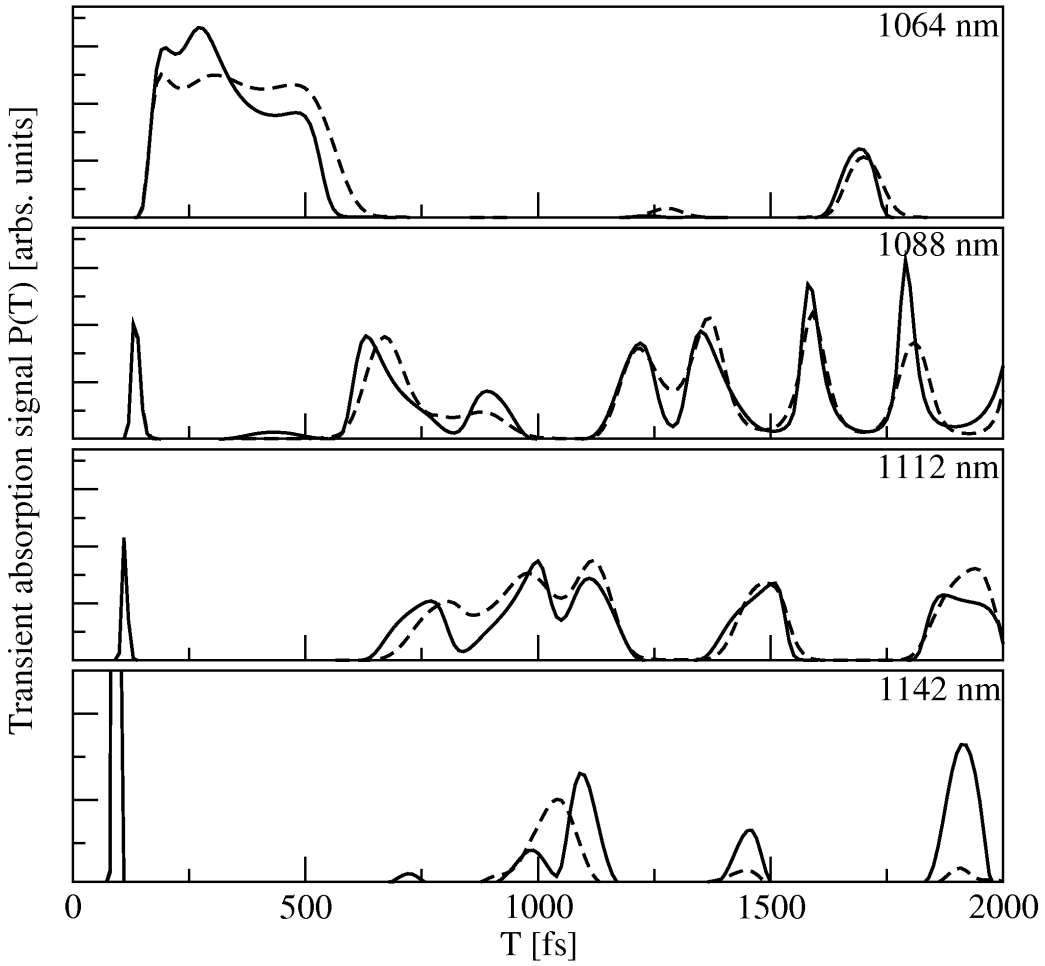

Figure 6.14: Pump-probe signals for selected probe laser wavelengths, as a function of delay time, T. It can be observed, that the inclusion of the dynamical correlations provokes the smoothing of the structures present in the TDH spectra.

To show this behaviour in more detail, the pump-probe signals for four selected

probe pulse wavelengths are plotted in 6.14. These transient spectra are nothing else but cuts through the 3-dimensional plots shown in Figure 6.13 at the specified wavelengths. At $\lambda = 1064$ nm, the transient Franck-Condon point is located at around R_1^*=7.6 a.u.. This point is close to the outer turning point of the motion of the 1^{st} shell. Hence the signal starts at zero, but quickly shows a sharp rise around 150 fs, indicating the initial expansion of the 1^{st} shell. During a time lapse of about 400 fs, the density $\rho_A^{(1)}(R_1)$ stays at large distances, before the first retraction occurs, leading to a vanishing of the signal around 550 fs.

Comparing the results obtained employing the TDH and the MCTDH integration schemes, one sees significant differences, even though the qualitative picture is comparable. For the other wavelengths, one can see that the overall structures are well described by the TDH approach, although the inclusion of dynamical correlations in the theoretical description leads to a smearing out of the signal.

The enhanced vibrational coherences observed in the TDH approach is specially visible in the case of $\lambda = 1142$ nm. At this wavelength, the transient Franck-Condon point is located around R_1^*=6.9 a.u.. Hence, the signal detects the wave packet at smaller radii than in the case of the other wavelengths. The fact that the signal is more enhanced in the calculations performed using the TDH approximation, reflects that the 1^{st} shell experiences a more elastic rebouncing. Specifically, a strong peak is found at 1900 fs, while in the correlated case this maximum is almost entirely absent.

To summarize, the main effect of explicitly accounting for the dynamical correlations is a more damped oscillatory motion of the different shells, which leads to measurable effects in the pump-probe spectra. However, the main features of the dynamics of geometrical rearrangement of the matrix are well described in the mean field approximation. This result suggest that a single Hartree product will be the most suitable choice to represent the many-body wave function, in future investiga-

tions on structural relaxation processes in quantum solids, such as $p-H_2$. The TDH approximation is adequate to analyse qualitatively, and to some extent also quantitatively, the dynamical response of these systems, while it has the advantage of being numerically much more efficient.

Chapter 7

Concluding remarks and perspectives

7.1 Conclusions

In this work, a radial shell model has been developed to attain a purely quantum mechanical description of the dynamical response of a *Ne* matrix, doped with a *NO* molecule, upon photo-excitation of the impurity. To achieve this, two methodologies have been used: the Time Dependent Hartree approximation and the Multiconfigurational Time Dependent Hartree approach. The first one is employed to simulate the rearrangement process in the solid, simultaneously propagating the wave function of the system in both the ground and the excited states, taking into account explicitly the shape of the pump pulse that couples these electronic states. The second approach, much more computational expensive, is used to evaluate the role of the dynamical correlations between the different degrees of freedom. In the present study, the multidimensional time-dependent Schrödinger equation is solved for a system with a large number of degrees of freedom (80 modes are considered,

corresponding to 4192 atoms which are restricted to move radially), while keeping a realistic description of intermolecular interactions. To our knowledge, only a few studies have been reported in the literature, about the quantum dynamics of molecular systems with tens of degrees of freedom. Typically, in this investigations, the quantum treatment was carried out at the expense of a significant simplification of the interaction potentials. The main conclusions of the work presented in this thesis are the following:

1. The structural rearrangement of the matrix is a multidimensional process, characterized by an initial expansion of the first shell of nearest neighbours of the impurity (the phenomenon known as electronic bubble formation) and the large coupling between the different degrees of freedom of the solid. As a consequence, the configurational modifications of the system are not a monotonic function of the shell radii. Instead, they clearly show the propagation of the perturbation along the preferential axis (110), defined by the diatomic molecule and its first nearest neighbours shell. An estimate of the velocity of propagation of the perturbation indicates that this process has a shock-wave like character.

2. There are two essential mechanisms of energy dissipation into the matrix: the direct collisions between the atoms lying along the main crystallographic axis and the side collisions between the atoms of each of these shells and its nearest neighbour atoms, pertaining to shells lying outside the preferential axis. These latter shells form a "bath" towards which the energy flowing through the main axis is dissipated. It is important to remark that this bath is not formed by remote atoms, but for atoms located in unfavourable positions with respect to the impurity. It has been found that 0.55 eV of the excess energy, initially deposited into the matrix by the pump pulse, are released into the "bath" *via*

the second mechanism mentioned above. The agreement between the dissipated energy, calculated in our simulations, with the experimental value (0.54 eV), reported in [3], is quite satisfactory.

3. It has been found that the width of the pump pulse has a significantly influence on the time-evolution of the wave packet formed during the excitation process. Using the real parameters of the pump-probe experiments on the relaxation dynamics of neon matrices doped with NO [3–5, 15], it has been found that the finite width of the excitation pulse (280 fs) causes the arising of a complex auto-interference pattern in the reduced density of the first shell. This is a purely quantum mechanical effect, originated by the fact that the time scale of the bubble formation and the duration of the excitation pulse are of the same order.

4. The results obtained for the transient absorption spectra within the TDH approximation reproduce qualitatively the experimental signals, showing clearly the general features of the restructuring process: the ultrafast bubble formation and its subsequent contraction around 1 ps, and the ulterior relaxation dynamics due to the couplings with other modes. Nevertheless, the contraction of the bubble is not a simple rebouncing of the first shell, but a collective response involving a great number of surrounding atoms forming the rest of the shells.

5. The influence of the dynamical correlations between the relevant degrees of freedom has been evaluated through the comparison between the results obtained by the numerical propagation of the initial wave packet, both in the TDH and in the MCTDH approaches. The overall finding is that the mean field approximation provides a correct description of the time evolution of most of observables. The energy transfer into the solid as well as the shell displacements are well de-

scribed within the TDH approximation. However, some quantities that contain finest information of the particle distributions in configuration space, i.e. the radial distribution functions, show a clear influence of the correlations.

6. It has been found that the vibrational coherence of the multi-configurational wave packet is much smaller than within the Hartree approximation. Specifically, the mean field approximation leads to pronounced breathings of the radial distribution functions, whereas they are practically absent in the results using the correlated wave function.

7. The latter characteristic can also be visualized in quantities like the pump-probe signals. In general, the explicit inclusion of correlations in the theoretical treatment leads to a smearing out of the spectra, conducing to least structured profiles. This means that the dynamical correlations tend to suppress the vibrational coherences appeared within the TDH approximation.

7.2 Perspectives

There are different possible directions to pursuing this job further:

1. *The explicit inclusion of the anisotropy of the impurity-rare gas potential.*
   The electronic densities determining the interactions $NO(X,A)$-Ne are slightly anisotropic [18, 22]. This effect can be accounted for by dividing the most affected shells into two or more subshells, treating each one as dynamically independent degrees of freedom. This approach will allow to extend the model beyond the pure radial approximation, though its applicability is limited to the amount of possible subdivisions, because of the increasing number of variables that should be incorporated explicitly in the theoretical treatment.

2. *The use of alternative (approximate) approaches.*

   To go beyond the radial approximation, in some cases, it may be convenient to make use of approximate methods, such as the Zero Point Averaged Dynamics (ZPAD) approach [25], which allows a separated description of each atom. In spite of its approximate character, it remains to be seen if the number of degrees of freedom of this particular system can be treated by this or similar approaches. Work along this line is currently in progress. In particular, the performance of single-particle Gaussian wave packets to model the structural response of the NO doped neon matrices is being explored.

On the other hand, the radial model developed in this thesis can be directly applied to the study of other solids with pronounced quantum behaviour like the para-hydrogen matrices, in which time resolved spectroscopy experiments of the matrix relaxation have been recently performed. [3–5, 15]. Due to the inapplicability of classical MD simulations to model the geometrical reorganization process in this system, the application of a methodology allowing a purely quantum treatment of the many-body system will help considerably to the interpretation of experimental signals in terms of the dynamics at the atomic level. The main difference between the pump-probe signals simulated in this work (within the TDH approximation) and the direct spectroscopic measurements is the more structured profile that characterizes the formers. These deviations tend to decrease as the number of configurations used to represent the many-body wave-function increases. Nevertheless, the computational cost associated to the increase of the correlation level beyond the one explored in this thesis results prohibitive. The results of the present investigation suggest that the mean field approximation is able to reproduce qualitatively the fundamental aspects of the dynamics in quantum solids, indicating that it is a reasonable choice to carry out quantum molecular dynamics simulations in similar solids like $p - H_2$.

Appendix A

Appendices

A.1 Intrashell interaction potential

The intrashell interaction contains the contributions from the *Ne* atoms within the same shell. Summing over all pairs of atoms of the same shell s, taking into account that these pair interactions are of the Lennard-Jones (LJ) type, an effective LJ interaction is obtained for $V_s(R_s)$, with scaled parameters ϵ_s and σ_s:

$$\begin{aligned} V_s(R_s) &= \sum_{i_s=1}^{n_s} \sum_{j_s=1}^{i_s-1} V(|\mathbf{r}_{i_s} - \mathbf{r}_{j_s}|) \\ &= \sum_{i_s=1}^{n_s} \sum_{j_s=1}^{i_s-1} 4\epsilon \left[\left(\frac{\sigma}{|\mathbf{r}_{i_s} - \mathbf{r}_{j_s}|} \right)^{12} - \left(\frac{\sigma}{|\mathbf{r}_{i_s} - \mathbf{r}_{j_s}|} \right)^{6} \right] \\ &= 4\epsilon_s \left[\left(\frac{\sigma_s}{R_s} \right)^{12} - \left(\frac{\sigma_s}{R_s} \right)^{6} \right] \quad . \end{aligned} \tag{A.1}$$

In this expression, $\epsilon_s = \epsilon(\lambda_6)^2/\lambda_{12}$ and $\sigma_s = \sigma R_s(\lambda_{12}/\lambda_6)^{1/6}$.

The coefficients λ_6 and λ_{12} are given by:

$$\lambda_6 = \sum_{i_s}^{n_s} \sum_{j_s=1}^{i_s-1} |\mathbf{r}_{i_s} - \mathbf{r}_{j_s}|^{-6}, \ \lambda_{12} = \sum_{i_s}^{n_s} \sum_{j_s=1}^{i_s-1} |\mathbf{r}_{i_s} - \mathbf{r}_{j_s}|^{-12} \quad .$$

Applying the decomposition of a LJ potential into a sum of Gaussian functions [21], it can be finally obtained:

$$V_s(R_s) \;=\; \sum_{p=1}^{n_G} G_s(p)\; e^{-\Gamma_s(p) R_s^2}$$

where, $G_s(p) = a_p\,(\epsilon_s/\epsilon)$ and $\Gamma_s(p) = \beta_p\,(\sigma/\sigma_s)^2$.

Throughout this work we consider a_p and β_p to be the parameters given in Ref. [21] corresponding to *Ne-Ne* LJ interaction potential.

A.2 Intershell interaction potential

The intershell interaction contains the contributions from the *Ne* atoms within different shells. Summing the pairs of interacting atoms corresponding to two different shells s and s', it is obtained:

$$\begin{aligned} W(R_s, R_{s'}) \;&=\; \sum_{i_s=1}^{n_s}\sum_{j_{s'}=1}^{n_{s'}} V(|\mathbf{r}_{i_s} - \mathbf{r}_{j_{s'}}|) \\ &=\; \sum_{i_s=1}^{n_s}\sum_{j_{s'}=1}^{n_{s'}} 4\epsilon \left[\left(\frac{\sigma}{|\mathbf{r}_{i_s} - \mathbf{r}_{j_{s'}}|} \right)^{12} - \left(\frac{\sigma}{|\mathbf{r}_{i_s} - \mathbf{r}_{j_{s'}}|} \right)^{6} \right] \end{aligned} \tag{A.2}$$

Expressing the LJ potential by its decomposition into a sum of Gaussian functions [21], $W(R_s, R_{s'})$ can be written as:

$$W(R_s, R_{s'}) \;=\; \sum_{i_s=1}^{n_s}\sum_{j_{s'}=1}^{n_{s'}}\sum_{p=1}^{n_G} a_p\; e^{-\beta_p(\mathbf{r}_{i_s} - \mathbf{r}_{j_{s'}})^2} \quad .$$

Expanding the exponential functions around the reference radii R_s^0 leads to:

$$W(R_s, R_{s'}) \;=\; \sum_{p=1}^{n_G}\sum_{J,K=0}^{\infty} F_{s,s'}^{J,K}(p) U_J(R_s) U_K(R_{s'}) \tag{A.3}$$

where $U_J(R_s) = (R_s - R_s^0)^J \; e^{-\beta_p (R_s - R_s^0)^2}$ y $U_K(R_{s'}) = (R_{s'} - R_{s'}^0)^K \; e^{-\beta_p (R_{s'} - R_{s'}^0)^2}$. The coefficients $F_{s,s'}^{J,K}(p)$ can be expressed by:

$$\begin{aligned} F_{s,s'}^{J,K}(p) \;\; = \;\; & \sum_{i_s}^{n_s} \sum_{j_{s'}}^{n_{s'}} \sum_{\left\{ \begin{smallmatrix} k,l,m \\ l+m=J \\ l+k=K \end{smallmatrix} \right\}} \frac{a_p (2\beta_p)^{k+l+m}}{k!l!m!} \frac{e^{-\beta_p |\mathbf{r}_{i_s}^0 - \mathbf{r}_{j_{s'}}^0|^2}}{(R_s^0)^J (R_{s'}^0)^K} \times \\ & \times [(\mathbf{r}_{j_{s'}}^0 - \mathbf{r}_{i_s}^0) \cdot \mathbf{r}_{i_s}^0]^m [(\mathbf{r}_{i_s}^0 - \mathbf{r}_{j_{s'}}^0) \cdot \mathbf{r}_{j_{s'}}^0]^k [\mathbf{r}_{i_s}^0 \cdot \mathbf{r}_{j_{s'}}^0]^l \quad . \end{aligned} \tag{A.4}$$

In this way, the multi-dimensional potential energy surface of equation (A.3) is written as a sum of factorized terms, i.e., of products of functions of only one coordinate, R_s. This form is compatible with the Heidelberg MCTDH program suite, optimizing the numerical integration of the time dependent Schrödinger equation.

A.3 Pump-probe spectra

For a Hamiltonian of the type,

$$\hat{H} = \hat{H}_0 + \hat{W} \quad , \tag{A.5}$$

where $\hat{H}_0$ is the non-perturbed Hamiltonian of the system and $\hat{W}$ is a perturbation which, in general, depends on time. The Schrödinger equation for this Hamiltonian reads

$$i\hbar \partial_t |\Psi\rangle = \hat{H} |\Psi\rangle \quad . \tag{A.6}$$

In the interaction picture, the wave function is defined as:

$$|\Psi\rangle = e^{-\frac{i}{\hbar} \hat{H}_0 t} |\tilde{\Psi}\rangle \quad . \tag{A.7}$$

In this way,

$$\partial_t|\Psi\rangle = -\frac{i}{\hbar}\left(e^{\frac{i}{\hbar}\hat{H}_0 t}\hat{W}e^{-\frac{i}{\hbar}\hat{H}_0 t}\right)|\tilde{\Psi}\rangle = -\frac{i}{\hbar}\tilde{W}|\tilde{\Psi}\rangle \quad . \tag{A.8}$$

Hence, the formal solution of the Schrödinger equation in this representation is:

$$|\tilde{\Psi}(t)\rangle = |\tilde{\Psi}(t_i)\rangle - \frac{i}{\hbar}\int_{t_i}^{t}\tilde{W}(t')|\tilde{\Psi}(t')\rangle dt' \quad . \tag{A.9}$$

Transforming to Schrödinger's picture, the equation (A.9) will take the form:

$$|\Psi(t)\rangle = e^{-\frac{i}{\hbar}\hat{H}_0(t-t_i)}|\Psi(t_i)\rangle - \frac{i}{\hbar}\int_{t_i}^{t}e^{-\frac{i}{\hbar}\hat{H}_0(t-t')}\hat{W}(t')|\Psi(t')\rangle dt' \quad . \tag{A.10}$$

The solution of equation (A.10), within first order perturbation theory, is obtained by replacing $|\Psi(t)\rangle = e^{-\frac{i}{\hbar}\hat{H}_0(t-t_i)}|\Psi(t_i)\rangle$ (the zero order solution) in the right hand side of the equation:

$$|\Psi(t)\rangle = e^{-\frac{i}{\hbar}\hat{H}_0(t-t_i)}|\Psi(t_i)\rangle - \frac{i}{\hbar}\int_{t_i}^{t}e^{-\frac{i}{\hbar}\hat{H}_0(t-t')}\hat{W}(t')e^{-\frac{i}{\hbar}\hat{H}_0(t'-t_i)}|\Psi(t_i)\rangle dt' \quad . \tag{A.11}$$

This solution will be applied to the case in which the perturbation is a laser pulse that couples two states. In our case, these will be the electronic states A and $\beta = C$ o D. For the sake of simplicity, we will consider the transitions to only one of them, for example, the C state. Then, the wave function of the system will be a linear combination the wave function in each of these states:

$$|\Psi(t)\rangle = |\Psi_A(\mathbf{R},t)\rangle|\Phi_A(\mathbf{r},t)\rangle + |\Psi_C(\mathbf{R},t)\rangle|\Phi_C(\mathbf{r},t)\rangle \quad , \tag{A.12}$$

where $|\Psi_A(\mathbf{R},t)\rangle$ represents the nuclear wave function of the A state, which depends on the positions of all the nuclei, $\mathbf{R}$, and $|\Phi_A(\mathbf{r},t)\rangle$ is the electronic wave function

of the A state, which depends on the electronic configuration denoted by $\mathbf{r}$, which contains the position vectors of all the electrons of the system. The same notation is used for the nuclear and electronic wave functions of the C state.

The non-perturbed Hamiltonian will be given by the matrix:

$$\hat{H}_0 = |\Phi_A\rangle\hat{H}_A\langle\Phi_A| + |\Phi_C\rangle\hat{H}_C\langle\Phi_C| \quad , \tag{A.13}$$

and the perturbation will be the probe laser pulse that couples both states,

$$\hat{W}(t) = E_0 f(t-T)e^{-i\omega(t-T)}|\Phi_C\rangle\mu_{CA}\langle\Phi_A| \quad , \tag{A.14}$$

where E_0 is the amplitude of the electromagnetic field, $f(t-T)$ is the envelope function describing the pulse shape, ω is the central pulse frequency and μ_{CA} is the dipole moment matrix element, calculated with the initial and final electronic wave functions.

Taking into account that the initial wave function of our problem is $|\Psi(t_i)\rangle = |\Psi_A\rangle|\Phi_A\rangle$, the solution of the Schrödinger equation, within first order perturbation theory (A.11), will be:

$$\begin{aligned} |\Psi(t)\rangle &= |\Phi_A\rangle e^{-\frac{i}{\hbar}\hat{H}_A(t-t_i)}|\Psi_A(t_i)\rangle - \\ &\quad -\frac{i}{\hbar}|\Phi_C\rangle\int_{t_i}^{t} e^{-\frac{i}{\hbar}\hat{H}_C(t-t')}\Big(E_0\mu_{CA}f(t'-T)e^{-i\omega(t'-T)}\Big)e^{-\frac{i}{\hbar}\hat{H}_A(t'-t_i)}|\Psi_A(t_i)\rangle dt' \end{aligned} \tag{A.15}$$

Multiplying (A.15) by $\langle\Phi_C|$,

$$\Psi_C(t) = \langle\Phi_C|\Psi(t)\rangle \tag{A.16}$$

$$= -\frac{i}{\hbar}\int_{-\infty}^{t} e^{-\frac{i}{\hbar}\hat{H}_C(t-t')}\left(E_0\mu_{CA}f(t'-T)e^{-i\omega(t'-T)}\right)e^{-\frac{i}{\hbar}\hat{H}_A(t'-T)}|\Psi_A(T)\rangle dt' \tag{A.17}$$

introducing the change of variables $t'' = t' - T$, it is obtained:

$$\Psi_C(t) = -\frac{i}{\hbar}E_0\mu e^{-\frac{i}{\hbar}\hat{H}_C(t-T)}\int_{-\infty}^{t-T} e^{\frac{i}{\hbar}\hat{H}_C(t'')}f(t'')e^{-i\omega t''}e^{-\frac{i}{\hbar}\hat{H}_A t''}|\Psi_A(T)\rangle dt'' \quad , \quad \text{(A.18)}$$

where the dipole moment $\mu_{CA} \equiv \mu$ is assumed to be constant.

The transient absorption signal measured in pump-probe experiments, is proportional to the final population of the C state, that is,

$$P_C(T) = \lim_{t\to\infty}\langle\Psi_C(t;T)|\Psi_C(t;T)\rangle \quad . \quad \text{(A.19)}$$

where T is the time delay between both pulses. Taking into account (A.18),

$$\begin{aligned} P_C(T) \quad \propto \quad & \int_{-\infty}^{+\infty} dt' \int_{-\infty}^{+\infty} dt'' \left[e^{-i\omega(t''-t')}f(t'')f(t')\right] \times \\ & \times\langle\Psi_A(T)|e^{\frac{i}{\hbar}\hat{H}_A t'}e^{-\frac{i}{\hbar}\hat{H}_C(t'-t'')}e^{-\frac{i}{\hbar}\hat{H}_A t''}|\Psi_A(T)\rangle \quad . \end{aligned} \quad \text{(A.20)}$$

Changing variables

$$t'' = t'_a + t_a/2 \;\text{ y }\; t' = t'_a - t_a/2 \quad , \quad \text{(A.21)}$$

and assuming a Gaussian shape of the probe pulse, $f(t) = e^{-(t/\tau)^2}$, (A.20) yields:

$$\begin{aligned} P_C(T) \quad \propto \quad & \int dt_a \int dt'_a \langle e^{-\frac{i}{\hbar}\hat{H}_A t'_a}\Psi_A(T)|e^{-\frac{i}{\hbar}\hat{H}_A\frac{t_a}{2}}e^{\frac{i}{\hbar}\hat{H}_C\frac{t_a}{2}}e^{-i\omega\frac{t_a}{2}}\times \quad , \\ & \times\left[e^{-2\left(\frac{t'_a}{\tau}\right)^2}e^{-\frac{1}{2}\left(\frac{t_a}{\tau}\right)^2}\right]e^{-i\omega\frac{t_a}{2}}e^{\frac{i}{\hbar}\hat{H}_C\frac{t_a}{2}}e^{-\frac{i}{\hbar}\hat{H}_A\frac{t_a}{2}}|e^{-\frac{i}{\hbar}\hat{H}_A t'_a}\Psi_A(T)\rangle \\ \propto \quad & \int dt_a \int dt'_a \langle e^{-\frac{i}{\hbar}\hat{H}_A t'_a}\Psi_A(T)|e^{\frac{i}{\hbar}(V_C - V_A - \hbar\omega)\frac{t_a}{2}}\times \\ & \times\left[e^{-2\left(\frac{t'_a}{\tau}\right)^2}e^{-\frac{1}{2}\left(\frac{t_a}{\tau}\right)^2}\right]e^{\frac{i}{\hbar}(V_C - V_A - \hbar\omega)\frac{t_a}{2}}|e^{-\frac{i}{\hbar}\hat{H}_A t'_a}\Psi_A(T)\rangle \quad , \end{aligned} \quad \text{(A.22)}$$

where it has been assumed that the impulsive limit holds, it means, that the variations of the kinetic energies, during the time during which the probe pulse is on, can be neglected. After some algebraic manipulations and integrating by t_a, the final equation for the C state population is obtained,

$$P_C(T) \propto \int_{-\infty}^{+\infty} dt'_a \; e^{-2\left(\frac{t'_a}{\tau}\right)^2} \langle \Psi_A(T+t'_a)| e^{-\left(\frac{\tau}{\hbar}\right)^2 (V_C - V_A - \hbar\omega)^2} |\Psi_A(T+t'_a)\rangle \quad \text{(A.23)}$$

where V_A y V_C are the potentials experienced, at each configuration, by the atomic nuclei in the A and C states, respectively.

Finally, in the case of our particular system, if the wave function Ψ_A is written as a Hartree product, and assuming that $V_C - V_A$ depends only on the radius of the first shell, R_1, the equation (A.23) can be rewritten as:

$$P_C(T) \propto \int_{-\infty}^{+\infty} dt'_a \; e^{-2\left(\frac{t'_a}{\tau}\right)^2} \int dR_1 \; e^{-\left(\frac{\tau}{\hbar}\right)^2 (V_C(R_1) - V_A(R_1) - \hbar\omega)^2} |\varphi_A^{(1)}(R_1, T+t'_a)|^2 \quad \text{(A.24)}$$

Bibliography

[1] V. A. Apkarian and N. Schwentner. *Chem. Rev.*, 99:1481, 1999.

[2] P. Jungwirth and B. Gerber. *Chem. Rev.*, 99:15831606, 1999.

[3] F. Vigliotti, L. Bonacina, and M. Chergui. *Phys. Rev. B*, 67:115118, 2003.

[4] G. Rojas-Lorenzo, J. Rubayo-Soneira, F. Vigliotti, and M. Chergui. *Phys. Rev. B*, 67:115119, 2003.

[5] F. Vigliotti, L. Bonacina, M. Chergui, G. Rojas-Lorenzo, and J. Rubayo-Soneira. *Chem. Phys. Lett.*, 362:31, 2002.

[6] S. A. Egorov and P. Larrégaray. *J. Chem. Phys.*, 128:244502, 2008.

[7] Ll. Uranga-Piña, A. Martínez-Mesa, L. García-Reyes, and J. Rubayo-Soneira. *Phys. Chem. Chem. Phys.*, 11:5358–5368, 2009.

[8] F. Vigliotti and M. Chergui. *Chem. Phys. Lett.*, 305:187, 1999.

[9] F. Vigliotti and M. Chergui. *Chem. Phys. Lett.*, 296:316, 1998.

[10] F. Marinetti, Ll. Uranga-Piña, E. Coccia, D. Lopez-Duran, E. Bodo, and F. A. Gianturco. *J. Phys. Chem. A*, 111:12289, 2007.

[11] Ll. Uranga-Piña, C. Meier, and J. Rubayo-Soneira. *J. Chem. Phys.*, 135:164504, 2011.

[12] A. Martínez-Mesa, Ll. Uranga-Piña, G. Rojas-Lorenzo, and J. Rubayo-Soneira. *Chem. Phys. Lett.*, 426:318, 2006.

[13] R. B. Gerber, M. V. Korolkov, J. Manz, M. Y. Niv, and B. Schmidt. *Chem. Phys. Lett.*, 327:76, 2000.

[14] M. Bargheer, M. Y. Niv, R. B. Gerber, and N. Schwentner. *Phys. Rev. Lett.*, 89:108301, 2002.

[15] F. Vigliotti, L. Bonacina, and M. Chergui. *J. Chem. Phys.*, 116:4553, 2002.

[16] H.-D. Meyer, U. Manthe, and L. S. Cederbaum. *Chem. Phys. Lett.*, 165:73–78, 1990.

[17] H.-D. Meyer, F. Gatti, and G. A. Worth, editors. *Multidimensional Quantum Dynamics: MCTDH Theory and Applications*. Wiley-VCH, Weinheim, 2009.

[18] P. Pajón-Suárez, G. Rojas-Lorenzo, J. Rubayo-Soneira, and R. Hernández-Lamoneda. *Chem. Phys. Lett.*, 421:389, 2006.

[19] J.P. Bergsma, P.H. Berens, K.R. Wilson, D.R. Fredkin, E.J. Heller, et al. *J. Chem. Phys.*, 88:612, 1984.

[20] Ll. Uranga-Piña, A. Martínez-Mesa, J. Rubayo-Soneira, and G. Rojas-Lorenzo. *Chem. Phys. Lett.*, 429:450, 2006.

[21] P.A. Frantsuzov and V.A. Mandelshtam. *J. Chem. Phys.*, 121:9247, 2004.

[22] P. Pajón-Suárez, G. Rojas-Lorenzo, J. Rubayo-Soneira, R. Hernández-Lamoneda, and P. Larrégaray. *J. Phys. Chem. A*, 113:14399, 2009.

[23] M. Sterling, Z. Li, and V. A. Apkarian. *J. Chem. Phys.*, 103:5679, 1995.

[24] P. Slavcek, P. Jungwirth, M. Lewerenz, N. H. Nahler, M. Farnk, and U. Buck. *J. Phys. Chem. A*, 107:7743, 2003.

[25] D. Bonhommeau, M. Lewerenz, and N. Halberstadt. *J. Chem. Phys.*, 128:054302, 2008.

[26] M.M. Martin and J.T. Hynes. *Femtochemistry and Femtobiology VI*. Elsevier, Amsterdam, The Netherlands, 2004.

[27] X. Chen and V.S. Batista. *J. Photochem. Photobiol. A*, 190:274, 2007.

[28] A. Douhal and J. Santamaria. *Femtochemistry and Femtobiology V*. World Scientific, Singapore, 2001.

[29] S. Mukamel. *Principles of Nonlinear Optical Spectroscopy*. Oxford University Press, 1995.

[30] M. T. Hochstrasser and R. M. Zanni. *Current Opinion in Structural Biology*, 11:516–522, 2001.

[31] Y. S. Kim and R. M. Hochstrasser. *J. Phys. Chem. A*, 113:8231–8251, 2009.

[32] S. Tam, M. Macler, M. E. DeRose, and M. E. Fajardo. *J. Chem. Phys.*, 113:9067, 2000.

[33] R. Zadoyan, J. Almy, and V. A. Apkarian. *Faraday Discussions*, 108:255, 1997.

[34] M. Bargheer, A. Borowski, T. Kiljunen, M. V. Korolkov, O. Kühn, J. Manz, B. Schmidt, M. Schröder, and N. Schwentner. *Coherence and Control of Molecular Dynamics in Rare Gas Matrices*, volume 87 of *Analysis and Control of Ultrafast Photoinduced Reactions*. Springer Verlag, Heidelberg, Germany, 2007.

[35] J. C. Owrutsky, D. Raftery, and R. M. Hochstrasser and. *Annu. Rev. Phys. Chem.*, 45:519, 1994.

[36] D. W. Miller and S. A. Adelman. *Int. Rev. Phys. Chem.*, 13:359, 1994.

[37] M. Gühr, M. Bargheer, M. Fushitani, T. Kiljunen, and N. Schwentner. *Phys. Chem. Chem. Phys.*, 9:779, 2007.

[38] M. D. Morse. *Chem. Rev.*, 86:1049, 1986.

[39] M.L. Klein and J.A. Venables. *Rare gas solids*. Academic Press, London, 1977.

[40] I. F. Silvera. *Rev. Mod. Phys.*, 52:393, 1980.

[41] J. van Kranendonk. *Solid Hydrogen*. Plenum Press, New York, 1983.

[42] B.I. Verkin. *Handbook of properties of condensed phases of hydrogen and oxygen*. Hemisphere Publishing, New York, 1991.

[43] A. Accardi, A. Borowski, and O. Kühn. *J. Phys. Chem. A*, 113:7491–7498, 2009.

[44] M. Bargheer, A. Cohen, R. B. Gerber, M. Gühr, M. V. Korolkov, J. Manz, M. Y. Niv, M. Schröder, and N. Schwentner. *J. Phys. Chem. A*, 111:9573–9585, 2007.

[45] H. Eshet, M.A. Ratner, and R.B. Gerber. *Chem. Phys. Lett.*, 431:199–203, 2006.

[46] M. Y. Niv, M. Bargheer, and R. B. Gerber. *J. Chem. Phys.*, 113:6660, 2000.

[47] M. Fushitani, M. Bargheer, M. Gühr, H. Ibrahim, and N. Schwentner. *J. Phys. B*, 41:074013, 2008.

[48] M. Gühr, H. Ibrahim, and N. Schwentner. *Phys. Chem. Chem. Phys.*, 6:5353, 2004.

[49] M. Gühr, M. Bargheer, and N. Schwentner. *Phys. Rev. Lett.*, 91:085504, 2003.

[50] M. Fushitani, N. Schwentner, M. Schröder, and O. Kühn. *J. Chem. Phys.*, 124:024505, 2006.

[51] M. Bargheer, R. B. Gerber, M. V. Korolkov, O. Kühn, J. Manz, M. Schröder, and N. Schwentner. *Phys. Chem. Chem. Phys.*, 4:5554, 2002.

[52] M. Chergui and N. Schwentner. *J. Chem. Phys.*, 89:1277, 1988.

[53] C. Jeannin, M.T. Portella-Oberli, S. Jimenez, F. Vigliotti, B. Lang, and M. Chergui. *Chem. Phys. Lett.*, 316:51, 2000.

[54] S. Jimenez, A. Pasquarello, R. Car, and M. Chergui. *Chem. Phys.*, 233:343, 1998.

[55] S. Jimenez, M. Chergui, G. Rojas-Lorenzo, and J. Rubayo-Soneira. *J. Chem. Phys.*, 114:5264, 2001.

[56] C. Jeannin, M.T. Portella-Oberli, F. Vigliotti, and M. Chergui. *Chem. Phys. Lett.*, 279:65, 1997.

[57] F. Vigliotti, A. Cavina, Ch. Bressler, B. Lang, and M. Chergui. *J. Chem. Phys.*, 116:4542, 2002.

[58] L. Bonacina, P. Larregaray, F. van Mourik, and M. Chergui. *J. Chem. Phys.*, 125:054507, 2006.

[59] F. Vigliotti, E. Sarraf, M. Chergui, and R. Scholz. *Phys. Rev. Lett.*, 83:2355, 1999.

[60] D.A. Micha and I. Burghardt, editors. *Quantum Dynamics of Complex Molecular Systems*. Springer, 2007.

[61] F. Stienkemeier, F. Meier, A. Hagele, H. O. Lutz, E. Schreiber, C. P. Schulz, and I. V. Hertel. *Phys. Rev. Lett.*, 83:2320, 1999.

[62] A. V. Benderskii, J. Eloranta, R. Zadoyan, and V. A. Apkarian. *J. Chem. Phys.*, 117:1201, 2002.

[63] C. Callegari, J. Higgins, F. Stienkemeier, and G. Scoles. *J. Phys. Chem. A*, 102:95, 1998.

[64] T. Momose, H. Hoshina, N. Sogoshi, H. Katsuki, T. Wakabayashi, and T. Shida. *J. Chem. Phys.*, 108:7334, 1998.

[65] T. Momose, M. Miki, T. Wakabayashi, T. Shida, M. C. Chan, S.S. Lee, and T. Oka. *J. Chem. Phys.*, 107:7707, 1997.

[66] M. E. Fajardo. *J. Chem. Phys.*, 98:110, 1993.

[67] A. V. Danilychev, V. E. Bondybey, V. A. Apkarian, S. Tanaka, H. Kajihara, and S. Koda. *J. Chem. Phys.*, 103:4292, 1995.

[68] Y. M. Ma, T. Cui, and G. T. Zou. *J. Chem. Phys.*, 114:3092, 2001.

[69] J. R. Krumrine, S. M. Jang, M. H. Alexander, and G. A. Voth. *J. Chem. Phys.*, 113:9079, 2000.

[70] Z. Li and V. A. Apkarian. *J. Chem. Phys.*, 107:1544, 1997.

[71] E. Cheng and K. B. Whaley. *J. Chem. Phys.*, 104:3155, 1996.

[72] D. Scharf, G. J. Martyna, D. H. Li, G. A. Voth, and M. L. Klein. *J. Chem. Phys.*, 99:9013, 1993.

[73] D. M. Ceperley. *Rev. Mod. Phys.*, 67:279, 1995.

[74] Y. Elran and P. Brumer. *J. Chem. Phys.*, 121:2673, 2004.

[75] T.D. Hone, S. Izvekov, and G.A. Voth. *J. Chem. Phys.*, 122:054105, 2005.

[76] U. Manthe, H.-D. Meyer, and L. S. Cederbaum. *J. Chem. Phys.*, 97:3199–3213, 1992.

[77] M. H. Beck, A. Jäckle, G. A. Worth, and H.-D. Meyer. *Phys. Rep.*, 324:1–105, 2000.

[78] D. Bonhommeau, Jr. P. T. Lake, C. Le Quiniou, M. Lewerenz, and N. Halberstadt. *J. Chem. Phys.*, 126:051104, 2007.

[79] R. Ramírez and C. P. Herrero. *Phys. Rev. B*, 72:024303, 2005.

[80] G.E. Moyano, P. Schwerdtfeger, and K. Rosciszewski. *Phys. Rev. B*, 75:024101, 2007.

[81] C. Cazorla and J. Boronat. *Phys. Rev. B*, 77:024310, 2008.

[82] N. Schwentner, E. E. Koch, and J. Jortner. *Electronic Excitations in Condensed Rare Gases*. Springer, Berlin, 1985.

[83] E. Boursey, M.-C. Castex, and V. Chandrasekharan. *Phys. Rev. B*, 16:2858, 1977.

[84] I. Ya Fugol. *Adv. Phys.*, 27:1, 1978.

[85] G. Zimmerer. *Excited-state spectroscopy in solids*. Soc. Italiana di Fisica, Bologna, Italy, 1987.

[86] I. Ya. Fugol and. *Adv. Phys.*, 37:1, 1988.

[87] T. Suemoto and H. Kanzaki. *J. Phys. Soc. Jpn.*, 49:1039, 1980.

[88] T. Suemoto and H. Kanzaki. *J. Phys. Soc. Jpn.*, 50:3664, 1981.

[89] C. H. Leung, L. Emery, and K. S. Song. *Phys. Rev. B*, 28:3474, 1983.

[90] K. Inoue, H. Sakamoto, and H. Kanzaki. *J. Phys. Soc. Jpn.*, 53:819, 1984.

[91] F. Coletti, J. M. Debever, and G. Zimmerer. *J. Chem. Phys.*, 83:49, 1985.

[92] T. Kloiber, W. Laasch, G. Zimmerer, F. Coletti, and J. M. Debever. *Europhys. Lett.*, 7:77, 1988.

[93] M. Chergui, N. Schwentner, and W. Bömer. *J. Chem. Phys.*, 85:2472–2482, 1986.

[94] S. Ossicini. *J. Phys. Chem. Solids*, 46:123, 1985.

[95] P. L. Kunsch and F. Coletti. *J. Chem. Phys.*, 70:726, 1978.

[96] M. Derbyshire and R. D. Etters. *J. Chem. Phys.*, 79:831, 1983.

[97] S. Cui, R. E. Johnson, and P. T. Cummings. *Phys. Rev. B*, 39:9580, 1989.

[98] F. G. Amar and B. J. Berne. *J. Phys. Chem.*, 88:6720, 1984.

[99] E. D. Potter, Q. Liu, and A. H. Zewail. *Chem. Phys. Lett.*, 200:605, 1992.

[100] M. Rosenblit and J. Jortner. *J. Phys. Chem. A*, 101:751, 1997.

[101] L.C. Ferreira and A.C. Cataneo. *Sci. Agric. (Piracicaba, Braz.)*, 67:236, 2010.

[102] D. E. Spence, P. N. Kean, and W. Sibbett. *Opt. Lett.*, 16:42, 1991.

[103] M. Groß and F. Spiegelmann. *Eur. Phys. J. D*, 4:219, 1998.

[104] W. S. Dennis, E. Durbin, Fitzsimm.Wa, O. Heybey, and G. K. Walters. *Phys. Rev. Lett.*, 23:1083, 1969.

[105] A. Fujisaki, K. Sano, T. Kinoshita, Y. Takahashi, and T. Yabuzaki. *Phys. Rev. Lett.*, 71:1039, 1993.

[106] Y. Takahashi, K. Sano, T. Kinoshita, and T. Yabuzaki. *Phys. Rev. Lett.*, 71:1035, 1993.

[107] T. Kinoshita, K. Fukuda, and T. Yabuzaki. *Phys. Rev. B*, 54:6600, 1996.

[108] T. Kinoshita, K. Fukuda, Y. Takahashi, and T. Yabuzaki. *Zeitschrift Fur Physik B-Condensed Matter*, 98:387, 1995.

[109] T. Kinoshita, K. Fukuda, Y. Takahashi, and T. Yabuzaki. *Phys. Rev. A*, 52:2707, 1995.

[110] R. G. W. Norrish and G. Porter. *Nature*, 164:658, 1949.

[111] M. Eigen. *Discuss. Faraday Soc.*, 17:194, 1954.

[112] F. J. McClung and R. W. Hellwarth. *J. Appl. Phys.*, 33:828, 1962.

[113] A. J. De Maria, D. A. Stetser, and H. Heynau. *Appl. Phys. Lett.*, 8:174, 1966.

[114] R. L. Fork, C. H. Brito Cruz, P. C. Becker, and C. V. Shank. *Opt. Lett.*, 12:483, 1987.

[115] A.H. Zewail. *J. Phys. Chem. A*, 104:5660, 2000.

[116] L. Bonacina. PhD thesis, École Polythécnique Fédéral de Laussane, 2004.

[117] H. Thuis, S. Stolte, and J. Reuss. *Chem. Phys.*, 43:351, 1979.

[118] G. A. Worth, M. H. Beck, A. Jäckle, and H.-D. Meyer. The mctdh package, version 8.2, (2000), university of heidelberg, heidelberg, germany. h.-d. meyer, version 8.3 (2002), version 8.4 (2007).

[119] R. Kosloff and H. Tal-Ezer. *Chem. Phys. Lett.*, 127:223, 1986.

[120] R. Schinke. *Photodissociation Dynamics.* Cambridge University Press, 1993.

[121] D. Tannor. *Quantum mechanics: a time dependent perspective.* University Science Book, Sausalito, California, 2007.

[122] M. L. Brewer, J. S. Hulme, and D. E. Manolopoulos. *J. Chem. Phys.*, 106:4832, 1997.

[123] P. A. M. Dirac. *Proc. Cambridge Philos. Soc.*, 26:376, 1930.

[124] J. Frenkel. *Wave Mechanics.* Clarendon Press, Oxford, 1934.

[125] P. Jungwirth and R. B. Gerber. *J. Chem. Phys.*, 102:6046, 1995.

[126] P. Jungwirth and R. B. Gerber. *J. Chem. Phys.*, 102:8855, 1995.

[127] P. Jungwirth, E. Fredj, and R. B. Gerber. *J. Chem. Phys.*, 104:9332, 1996.

[128] R. B. Gerber, P. Jungwirth, E. Fredj, A. Rom, and D. L. Thompson, editors. *Modern Methods for Multidimensional Dynamics Computations in Chemistry.* World Scientific, Singapore, 1998.

[129] N. Makri and W. H. Miller. *J. Chem. Phys.*, 87:5781, 1987.

[130] J. Jortner and B. Pullman, editors. *Large finite systems: Proceedings of the twenti- eth Jerusalem Symposium of Quantum Chemistry and Biochemistry.* Dordrecht, Reidel, 1987.

[131] C. Meier and V. Engel. *Phys. Chem. Chem. Phys.*, 4:5014, 2002.

[132] M. Braun, C. Meier, and V. Engel. *J. Chem. Phys.*, 103:7907, 1995.

[133] M. Braun, C. Meier, and V. Engel. *J. Chem. Phys.*, 105:530, 1996.

[134] L. W. Ungar and J. A. Cina. *Advances in Chemical Physics*, volume 100. John Wiley & Sons, 1997.

[135] U. Banin, A. Bartana, S. Ruhman, and R. Kosloff. *J. Chem. Phys.*, 101:8461, 1994.

[136] A. Bartana, U. Banin, S. Ruhman, and R. Kosloff. *Chem. Phys. Lett.*, 229:211, 1994.

[137] M. Hartmann, J. Pittner, V. Bonacic-Koutecky, A. Heidenreich, and J. Jortner. *J. Chem. Phys.*, 108:3096, 1998.

[138] M.-C. Heitz, G. Durand, F. Spiegelman, C. Meier, R. Mitric, and V. Bonacic-Koutecky. *J. Chem. Phys.*, 121:9906, 2004.

[139] Ll. Uranga-Piña, C. Meier, and J. Rubayo-Soneira. *accepted for publication in Chem. Phys. Lett.*, 2011.

[140] F. Vigliotti, G. Zerza, M. Chergui, and J. Rubayo-Soneira. *J. Chem. Phys.*, 109:3508, 1998.

[141] H. Zacharias, J.B. Halpern, and K.H. Welge. *Chem. Phys. Lett.*, 43:41, 1976.

[142] H. Katsuki, H. Chiba, B. Girard, C. Meier, and K. Ohmori. *Science*, 311:1589, 2006.

AUTHOR: Llinersy Uranga-Piña

TITLE: Ultrafast geometrical rearrangement of solid neon upon photoexcitation of a NO impurity: a quantum dynamics study

THESIS DIRECTOR: Christoph Meier

CO-DIRECTOR: Jesús Rubayo Soneira

SUMMARY:

This thesis reports on results of quantum molecular dynamics simulations of photo-induced structural dynamics in nitric oxide (NO) doped solid neon (Ne). The local perturbation, caused by the optical excitation of the dopant molecule, propagates radially from the NO to the lattice atoms, in a shock-wave-like fashion. The ultrafast relaxation dynamics is studied using a purely quantum mechanical approach, based on a multidimensional shell model, with the shell radii being the dynamical variables. As a consequence of the weak anisotropy of the NO-Ne interaction, the model accounts for the main dynamical features of the rare gas solid while it implies a significant dimensionality reduction with respect to the real condensed phase system. The numerical propagation of the multidimensional wave packet allows the analysis of both the static deformation of the solid due to the impurity and the dynamical response after femtosecond excitation. The photo-induced dynamics of solvent atoms around the impurity centre is found to be a complex collective process, which involves many degrees of freedom. The proposed theoretical methodology allows to consider realistic time-dependent femtosecond pulses and the effect of the pulse duration on the geometrical rearrangement dynamics is clearly shown. The time-resolved absorption spectra were simulated, using the pulse parameters of previous pump-probe spectroscopic experiments, carried out with with femtosecond time-resolution. The computed transient signals qualitatively reproduce the experimental results, thereby enabling a clear analysis of the ultrafast mechanism of the energy transfer into the solid. The influence of explicitly including dynamical correlations in the theoretical treatment of the relaxation dynamics, within the Multi-Configurational Time-Dependent Hartree (MCTDH) scheme, was addressed. This aspect is found to be important only for certain degrees of freedom. The consideration of multi-configurational wave functions does not appreciably modify the values of observables such as the average shell radii, with respect to those obtained employing the time-dependent Hartree ansatz. However, the inclusion of correlations reduces the degree of structuring of the calculated pump-probe signals and improve the agreement with experimental results.

KEYWORDS: quantum dynamics, ultrafast spectroscopy, condensed phase, optical excitation, molecules, correlations, MCTDH

AUTEUR: Llinersy Uranga-Piña

TITRE: Ultrafast geometrical rearrangement of solid neon upon photoexcitation of a NO impurity: a quantum dynamics study

DIRECTEUR DE THÈSE: Christoph Meier

CO-DIRECTEUR DE THÈSE: Jesús Rubayo Soneira

LIEU ET DATE DE SOUTENANCE: Université de La Havane, le 9 juillet 2012

RESUMÉ:

Cette thèse présente des modélisations quantiques de la dynamique photoinduite de la molécule NO en matrice de néon. La perturbation locale, créée par l'excitation optique de NO, se propage d'une façon radiale, comme une onde de choc. La dynamique ultrarapide de relaxation est étudiée à l'aide d'un modèle de couches successives autour de la molécule NO. Grâce à la faible anisotropie de l'interaction NO-Ne, le modèle est capable de décrire les mouvements principaux des atomes voisins du solide, tout en réduisant la dimensionnalité. La propagation numérique du paquet d'ondes multidimensionnel permet d'analyser des déformations statiques ainsi que la réponse dynamique après excitation femtoseconde. La méthodologie présentée permet en plus de considérer des paramètres réalistes de l'impulsion laser excitatrice, et les effets de leur durée est clairement mise en évidence. Des calculs de spectres d'absorption résolus en temps donnent un bon accord avec des mesures expérimentales, et permettent ainsi une analyse détaillée des mécanismes de transfert d'énergie vers le solide. Dans ce contexte, l'influence des corrélations quantiques a été étudiée, en utilisant la méthode MCTDH (multi configuration time dependent Hartree). Entre certains degrés de liberté, elles jouent un rôle important, mais pour des observables comme l'énergie transférée ou les positions moyennes des atomes du solide, une approche de champ moyen dépendant du temps donne déjà des résultats précis. Par contre, les effets des corrélations sont bien visibles dans des observables mesurées, car ils mènent à des spectres d'absorption plus lisses, en meilleur accord avec les expériences.

MOTS-CLÉS: dynamique quantique, spectroscopie ultrarapide, phase condensée, excitation optique, molécules, corrélation, MCTDH

SPECIALITÉ: Physique de la matière

UNITÉ DE RECHERCHE:
Laboratoire Collisions, Agrégats, Réactivité (UMR 5589)
IRSAMC – Université Paul Sabatier – Bât. 3R1b4
118 rte de Narbonne
31062 TOULOUSE CEDEX 09, FRANCE